

All-sky Survey of Short X-ray Transients by MAXI GSC

Takahiro TOIZUMI

Department of Physics, Graduate School of Science,
Tokyo Institute of Technology, Tokyo, Japan

February 2012

Contents

1	Introduction	2
2	All-sky Transient Surveys with Soft X-ray Band	4
2.1	HEAO-1	4
2.2	Ariel V	5
2.3	Einstein (HEAO-2)	6
2.4	Granat/WATCH	6
2.5	ROSAT	7
2.6	BeppoSAX	7
2.7	HETE-2	8
2.8	Summary	9
3	Short X-ray Transients	13
3.1	Gamma-ray Bursts	13
3.1.1	Prompt Emission	14
3.1.2	Statistical Properties of GRB	15
3.1.3	X-ray Flash	19
3.1.4	GRB Afterglows	19
3.1.5	Off-axis Model	20
3.1.6	Orphan Afterglows	21
3.2	Other X-ray Transients	23
3.2.1	Jet from BL Lac	23
3.2.2	Active Star Flare	24
3.2.3	Tidal Disruption of a Star by the Supermassive Black Hole	26
3.2.4	Super Nova Shock Breakout	28
4	Monitor of All-sky X-ray Image	30
4.1	Gas Slit Camera (GSC)	31

4.1.1	Overview of GSCs	31
4.1.2	Field of View	31
4.1.3	Principle of the position determination	32
4.1.4	Xe Proportional Counter	35
4.1.5	In-Orbit Performance	37
4.2	Solid-State Camera	38
4.3	Radiation Belt Monitor	40
5	Analysis & Results	42
5.1	Short X-ray Transients Search in All-sky	42
5.1.1	Data Selection for GSCs	42
5.1.2	Data Reduction	43
5.1.3	Effective Area for Sources	46
5.1.4	Effective Area for Background Counts	47
5.1.5	Extraction of Candidates for Transients	49
5.1.6	GSC Exposure Map	51
5.1.7	Transient Frequency Map	51
5.2	Local Analysis for Candidates of Transient	52
5.2.1	Data Reduction	53
5.2.2	Localization of the detected X-ray source	53
5.2.3	Flux Calculation	54
5.2.4	Exclusion of False Events	55
5.2.5	Calculation of False Detection Probability	58
5.2.6	List of Detected Transients	58
5.2.7	Spatial Distribution of Detected Transients	61
5.2.8	Identification of Transients	61
6	Discussion	65
6.1	Statistic Estimation for Transients	65
6.1.1	Dipole Moment	65
6.1.2	V/V_{max} Test	66
6.1.3	Log N -Log S distribution	66
6.1.4	Comparison of the Rate of XRF with GRB	69
6.1.5	Transients in the Index $-3/2$ Region	69
6.2	Future Work	70
7	Conclusion	71

A	Comparsion with past MAXI data	73
A.1	Comparsion with MAXI GRB	73
A.2	Comparsion with MAXI Flare Star	73
B	Figures	76

List of Figures

2.1	The Log N -Log S distribution of HEAO-1 transients	5
2.2	The XRF samples of BeppoSAX	8
2.3	The spectral distribution of HETE transients	9
2.4	Summary of the FXT search	11
3.1	Distribution of GRB duration	15
3.2	Angular distribution of GRB	16
3.3	Log N –Log S distribution of GRBs detected by BATSE.	18
3.4	Image of the first observed afterglow	20
3.5	The typical light curve of X-ray afterglows	21
3.6	The schematic view of the off-axis model	22
3.7	Light curve of Markarian 421	23
3.8	Log N -Log S plot for AGNs detected by MAXI/GSC	24
3.9	Light curve of the flare stars	25
3.10	Light curve of the candidates of tidal disruptions I	26
3.11	Light curve of the candidates of tidal disruptions II	27
3.12	Light curve of the candidates of the super nova shock breakout	28
4.1	Picture of MAXI on ISS	30
4.2	Picture of GSC and SSC	31
4.3	Field of View of MAXI GSC	33
4.4	Principle of position determination	34
4.5	Construction of GSC unit (anode direction)	36
4.6	All-sky image observed by MAXI GSC	40
4.7	Particle map observed by MAXI/RBM	41
5.1	False detection of transients around Sco X-1	45
5.2	Example of effective area	47
5.3	Integrated background plot on the BEX coordinate	49

5.4	Time variability of NXB	50
5.5	Exposure map observed by MAXI/GSC	52
5.6	Candidates frequency map observed by MAXI/GSC	53
5.7	Examples for PSF images	54
5.8	The θ distribution of the leak events.	56
5.9	Transient distribution observed by MAXI GSC	61
5.10	Prompt emission of GRB100707A detected by Suzaku WAM	62
6.1	LogN-LogS distribution of X-ray transients	67
B.1	Light curves of transients	77
B.2	Light curves of transients	78
B.3	Light curves of transients	79
B.4	Light curves of transients	80

List of Tables

2.1	Comparison of the each satellite	12
4.1	Summary of GSCs	32
4.2	Summary of the HV operation of GSC counter	39
5.1	Excluded sources for transient search	43
5.2	Transients table detected with probability of 10^{-8}	59
5.3	Transients table detected by multiple cameras with 9σ significance	60
6.1	Conversion values of Swift BAT and MAXI GSC	68
A.1	Comparison for this work with past detected GRB by MAXI.	74
A.2	Comparison for this work with past detected flare from active star by MAXI	75

Abstract

We searched for short X-ray transients in the 15 months data obtained by Monitor of All-sky X-ray Image (MAXI)/ Gas Slit Camera (GSC).

Studies of short X-ray transients had been conducted by several all-sky survey missions. In the X-ray band, the candidates of the transients probably includes various classes of events such as Gamma-ray bursts (GRBs), X-ray flashes (XRFs), flares stars, and active galactic nuclei (AGNs). In addition, the very rare events will be possibly detected in X-ray band such as tidal disruption events and nova/supernova shock breakouts. However, the systematic survey of short X-ray transients has not been conducted yet because of the low frequency of the transients, small field of view, and small frequency of the monitoring.

Monitor of All-sky X-ray Image (MAXI) is an all-sky X-ray monitor mounted on the International Space Station (ISS). The Gas Slit Camera (GSC) scans 85 % of the entire sky every 92 minutes (i.e. orbital period of ISS). The transit time of the GSC over a source is about 40 seconds on the orbital plane, and longer towards the orbital poles.

We searched for short X-ray transients in the all-sky survey data obtained with MAXI/GSC in the 4.0-10.0 keV energy band using the data obtained between October 1, 2009 and December 31, 2010. In this study, we searched for transient sources that are detected in single scans of MAXI/GSC, therefore the durations of the emission should be shorter than 92 minutes. The typical detection limit is about 50 mCrab (5σ).

As a result of the transient survey, we found 29 transients with the fluctuation probability of less than 10^{-8} . Eight of them are identified as prompt emission of GRBs reported to the Gamma-Ray Burst Coordinate Network (GCN), one as a GRB afterglow. Three transients are positionally coincident with flare stars, and other two with known X-ray sources. The other 15 transients remained unidentified.

We investigated origin of the detected 29 transients with fluctuation probability of less than 10^{-8} based on angular distribution, V/V_{max} test, and the LogN-LogS distribution. We obtained the value of these parameters as angular moment of $\langle \cos\theta \rangle = 0.02 \pm 0.17$, and $\langle V/V_{max} \rangle = 0.517 \pm 0.054$. The value of angular distribution $\langle \cos\theta \rangle$ is consistent with being isotropic. Thus majority of these sources are either located in the Galactic Disk, like nearby flare stars, or extragalactic like GRB, XRFs, AGNs, or supernova. The value of $\langle V/V_{max} \rangle$ is consistent with the spatial distribution which are uniformly in the Euclidean space. The cumulative flux distribution LogN-LogS obtained by MAXI/GSC transients suggests that there are two components; one is composed primarily of GRBs and the other with various faint events. The GRB components are well fitted by the

Swift GRB curve, and other components are parallel with index $-3/2$ on the $\text{Log}N\text{-Log}S$ distribution plot.

These two components suggest the X-ray emission from the transient clearly other than GRBs. and rapid multiwavelength followup observations should be useful for identifying these faint class transients.

Chapter 1

Introduction

Studies of short X-ray transients with time scales of few seconds to one day have been conducted using several all-sky survey missions, HEAO-I (Ambruster et al. 1986[1] and Connors et al. 1986[2]), Ariel V (Grindlay et al. 1999[3]), Einstein (Gotthelf et al. 1996[4]), Granat (Castro et al. 1999[5]), ROSAT (Greiner et al. 2000[6]), BeppoSAX (Heise et al. 2001[7]), and HETE-2 (Sakamoto et al. 2005[8]).

In the soft X-ray band, there are various classes of transients. On the galactic plane, many X-ray transients were found and observed by several X-ray satellites. For example, X-ray burster near the galactic center are neutron stars in close binary systems on which thermonuclear explosion occurs with various frequencies. These transients are originated in the galactic sources and distributed around the galactic center or in the arms. Numerous isotropically distributed transients are also found and observed. These transients should be distributed either in the solar system neighborhood or in the extragalactic space. The candidates of such transients are Gamma-ray bursts (GRBs), afterglows of GRBs, X-ray flashes, flares from active stars, and flares from active galactic nuclei. One of the most interesting motivation of the transient search is the detection of the theoretically predicted X-ray sources such as a tidal disruption (Burrows et al. 2011[9]) and a super nova shock breakout (Soderberg et al. 2008[10]) which have been detected only on few occasions.

Currently, the major constituents of fast X-ray transients are considered to be Gamma-ray bursts (GRBs) and active stars, which isotropically distributed. The $\text{Log}N\text{-Log}S$ distribution of fast X-ray transients are thought to be consistent with the sum of these transient classes (Arefiev et al. 2003[11]). However, these studies are based on small samples of X-ray transients, and merged the data are inhomogeneous taken with different energy bands. Thus, a high statistical and systematic result has been awaited. If we are able to obtain a sample of transients with as large statistics as the BATSE (Briggs et al. 1993[12]; hundreds or thousands of transients), we can investigate the composition of these

X-ray transients more reliably. For this study, we need a detector system with (1) 'large field of view' in order to survey the whole sky uniformly, (2) 'high sensitivity' in order to detect faint transients. (3) 'high scan frequency' in order to detect the X-ray transients with various timescales systematically. In addition, various biases introduced by merging data from different systems can be eliminated by using a single detector system.

MAXI is an all-sky X-ray monitor mounted on the International Space Station. The Gas Slit Camera (GSC) on board the MAXI scans 85 % of the entire sky every 92 minutes (i.e. orbital period of ISS). The transit time of the GSC over a source is about 40 seconds if the source is on the orbital plane, and longer towards the orbital poles. GSC has sensitivity in the X-ray energy band (2.0–30.0 keV), a large effective area of 5320 cm², a long and thin field of view of 160° × 3° and a lower threshold for single scan of about 50 mCrab ($\sim 5 \times 10^{-10}$ erg s⁻¹ cm⁻² for 4.0–10.0 keV). MAXI/GSC can observe transients more systematically using its large field of view and scan frequency than the past all-sky survey missions.

We searched for short X-ray transients in the all-sky survey data obtained by the MAXI/GSC in the 4.0–10.0 keV energy band between October 1, 2009 and December 31, 2010 (15 month). We used the cleaned GSC data that do not suffer from contamination of bright galactic sources, high particle fluxes, solar flares, and other artifacts that mimic transient sources.

In this thesis, we first review the past transients searches conducted by several all-sky survey satellites, and compare the results from these missions (Chapter 2). Next, we review the current understanding of the candidates for X-ray transients: Gamma-ray bursts, X-ray Flashes, AGN, active stars, and other extragalactic transients (Chapter 3). Thirdly, we introduce our mission of MAXI/GSC (Chapter 4), then, we describe the analysis method for searching transient events in the MAXI/GSC data (Chapter 5). Fifthly, we discuss the obtained statistics of short transient events in the 4–10 keV X-ray band, and compare it with the GRBs detected by Swift BAT (Chapter 6). And finally we describe the conclusion of our transient search (Chapter 7).

Chapter 2

All-sky Transient Surveys with Soft X-ray Band

In this chapter, we review the past all-sky survey missions and their results on all-sky transient surveys in the soft X-ray band.

2.1 HEAO-1

The first systematic all-sky survey of soft X-ray transients was performed using High Energy Astronomy Observatory 1 (HEAO-1). HEAO-1 was launched on August 12, 1977 and scanned the entire sky three times from August 1977 to January 1979 (Ambruster et al. 1986[1]; Connors et al. 1986[2]). The spin axis of the satellite was pointed toward the Sun at all times during the scanning operations, and it was incremented every 12 hours by 0.5° . The spin period of the satellite is about 35 minutes, during which each detectors completed one scan (360°) of the sky with the Sun angle of 90° . The source was seen for only about 10 second in a single scan. The whole sky was scanned every 6 month with this scanning pattern.

HEAO-1 had seven large-area thin-window proportional counters of various effective areas and fields of view. The energy range of these detectors was 0.5–20.0 keV. The primary survey modules (modules 1–4) had an effective area of 1650 cm^2 with $1 \times 4^\circ$ fields of view. Module 5 had a smaller field of view ($1 \times 0.5^\circ$) and it was primarily used to determine the source positions.

HEAO-1 found ten short X-ray transients in the A-1 survey (6 month, Ambruster et al. 1986[1]) in the 0.5–20 keV energy band, and eight transients in the A-2 survey (over 1.5 year, Connors et al. 1986[2]) in the 2–20 keV energy band. The scan time of the sources were 10 s for the A-1 survey and 60 s for the A-2 survey respectively. In the A-1

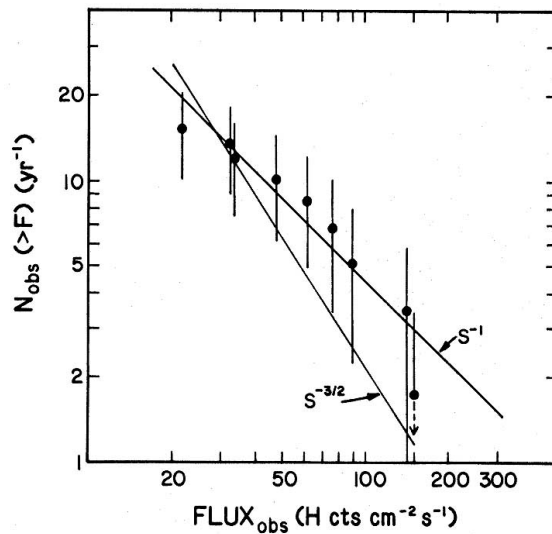


Figure 2.1: The first $\text{Log}N\text{-Log}S$ distribution for X-ray transients detected by HEAO-1[1]. Number of sample is nine sources detected in about 1.5 year operation (A-1).

survey, eight of these transients were identified to flare stars, but remaining 2 sources were not identified. The A-2 survey found three transients that were directly attributable to stellar flaring sources, but other five transients were not identified. Figure 2.1 shows the $\text{Log}N\text{-Log}S$ distribution of HEAO-1 A1 transients.

2.2 Ariel V

The X-ray transients in the Ariel V data were searched for by Grindlay et al. 1999[3].

Ariel V was an X-ray astronomy satellite developed by UK and USA, and launched on 1974 October 15 from the San Marco platform in India. The Sky Survey Instrument (SSI) on board Ariel V had an angular resolution of $0.75 \times 10^\circ$, with an effective area of 290 cm^2 , and an energy range of 2.0–20.0 keV. The detection principle of SSI was similar to that of the HEAO-1. The spin period of the satellite was approximately 6 s and the detector scanned great circles on the sky.

SSI found 27 transient sources (Pye et al. 1983[13]) with significances above 5.5σ , or a threshold flux of $8 \text{ counts s}^{-1} \text{ cm}^{-2}$ ($\sim 20 \text{ mCrab}$) in its 5.5-year operation (October 1974–March 1980). The detected transients (including one source that was probably detected twice) are distributed approximately isotropically on the sky. They made the $\text{Log}N\text{-Log}S$ distribution of these sources with fluxes above 20 mCrab, and fitted the distribution to a formula $N = N_0(S/S_0)^\alpha$ with $\alpha = 0.8 \pm 0.8$ and $N_0 = 65 \pm 30$.

Fourteen of the 27 transients detected by Ariel V were identified to known X-ray sources: Be X-ray binaries, RS CVn stars, BL Lac objects, and low-mass X-ray binaries. Remaining 13 transient sources were classified as GRB candidates.

As the result, the rate of X-ray transients without counterpart (the rate of GRB candidates) are consistent with the BATSE GRB $\log N$ - $\log S$ distribution. It meant that the rate of GRB afterglows were equal to that of prompt emission. Grindlay et al. 1999[3] concluded that the difference of beaming between prompt and afterglow emission were not required.

2.3 Einstein (HEAO-2)

The Einstein Observatory (*i.e.* HEAO-2 which was renamed after launch) carried a high-resolution X-ray telescope with a 3.4 m focal length and a 1.0 degree^2 field of view. The Imaging Proportional Counter (IPC), which covers the full focal plane of the telescope, had an energy range of 0.2–3.5 keV, and an effective area of about 100 cm^2 .

Short-duration X-ray transients serendipitously observed by the IPC were reported by Gotthelf et al. 1996[4]. The IPC was operated for 3 years (November 1978–April 1981), and surveyed X-ray transients with a total exposure time of $1.5 \times 10^7 \text{ s}$, with a limiting sensitivity of $10^{-11} \text{ erg s}^{-1} \text{ cm}^{-2}$. IPC detected 42 X-ray flash candidates, and 18 of these transients had spectra consistent with extragalactic origins and light curves similar to X-ray counterparts of GRB. The duration of transients are $\sim 10 \text{ s}$, and these events did not have identified counterparts in its spatial error circle. The rate of transients detected by the IPC was $2 \times 10^6 \text{ yr}^{-1}$. This is far more numerous than known GRBs.

2.4 Granat/WATCH

The international Astrophysical Observatory “GRANAT” was a Soviet space observatory developed in collaboration with France, Denmark and Bulgaria. It was launched on 1989 December 1. The X-ray instrument ‘WATCH’ was designed to monitor the sky continuously and alerted a discovery of new X-ray transients to the other on-board instruments. The detector design is based on the rotation modulation collimator principles. The fields of view covered approximately 75% of the sky. WATCH had two energy ranges of approximately 8–15 keV and 15–100 keV. It accumulated the data for 4, 8, or 16 s, depending on memory filling. During a burst or a transient event, count rates were accumulated with a time resolution of 1 second into 36 energy channels (NASA homepage about GRANAT[14]).

WATCH discovered six X-ray transients (Castro-Tirado et al. 1999[5]). Three of these transients were bright and fast in X-ray band, and were located at high latitudes in the galactic coordinates. Two of these transients had counterparts of the flare star in their error boxes. No counterparts were found for the other short transient.

The other three events were observed for long durations (for ~ 1 day). They were located near the galactic plane, and Castro-Tirado et al. 1999[5] suggested that these transients were produced by compact binaries.

2.5 ROSAT

ROSAT (ROentgen SATellite) was developed by Germany, the USA, and the UK. It was launched on June 1, 1990. ROSAT conducted its mission in two phases. The first mission was the all-sky survey using the Position Sensitive Proportional Counter (PSPC) to scan the sky continuously. It was performed during the period from August 1, 1990 to January 25, 1999. After the first six months, ROSAT performed second mission that was the individual pointing observations of selected astrophysical sources. The PSPC had an energy range of 0.1–2.5 keV, a field of view of 2° diameter, and an effective area of 240 cm^2 .

Greiner et al. 2000[6] searched for X-ray afterglow candidates of GRBs in the ROSAT all-sky survey data. They found 27 X-ray transients, but most of them were identified to flare stars. Using the BATSE data, they calculated the rate of afterglows detected by ROSAT, and they obtained 3.7 GRB afterglows during the ROSAT operation period. This value was consistent with detected candidate rate. Greiner et al. 2000[6] concluded that beam opening angles of GRBs are comparable in the X-ray and gamma-ray domains.

2.6 BeppoSAX

BeppoSAX was launched on April 30, 1996, and observed numerous X-ray transients until the end of its operation (April 30, 2002). While the most important work of BeppoSAX is discovery of afterglows of GRBs, we describe the fast X-ray transients (FXTs) detected by BeppoSAX in this section.

Wide Field Camera (WFC) on board BeppoSAX is a two-dimensional position sensitive detector (multi-wire proportional counter) with a coded mask. WFC had an energy range of 2–28 keV, a field of view of 20×20 degree², the sensitivity of ~ 1 mCrab for a 100 ks integration, and an effective area of 250 cm^2 including the transmission efficiency of the the coded mask. Gamma-ray burst monitor (GRBM), another detector system on

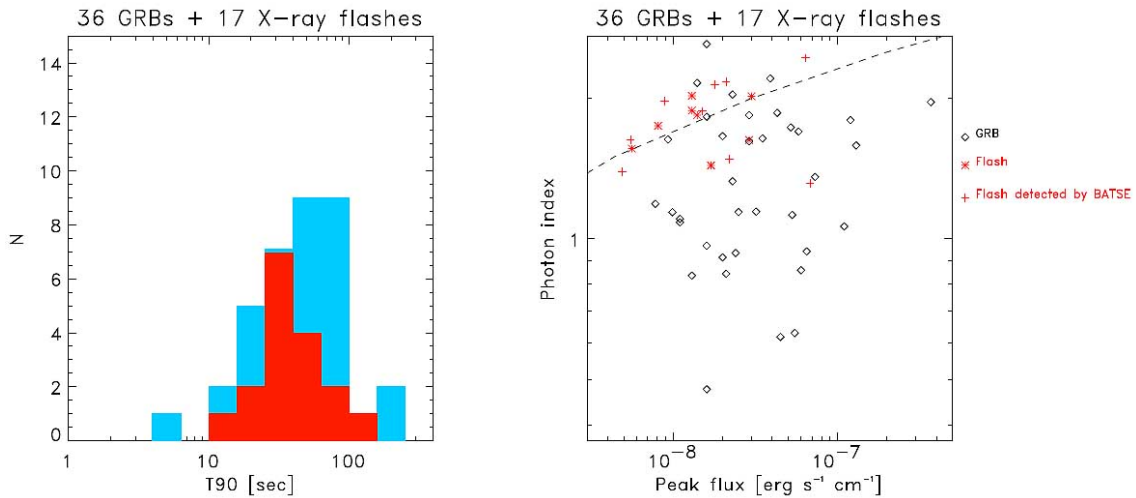


Figure 2.2: The left panel shows the histogram of T_{90} for hard GRBs (blue) and XRFs (red). The right panel shows distribution of the peak flux in 2–25 keV band and the photon index of the power-law spectra.

board BeppoSAX, monitored GRB in the energy range of 40–700 keV from the entire sky. While GRBM had no information on the incident direction, 10 % of GRBs detected by the GRBM were found in the field of view of the WFC. Heise et al. 2001[7] found fast X-ray transient sources that were detected only by the WFC, and not by the GRBM in the γ -ray band (40–700 keV). They called these events 'X-ray flash (XRF)'. Some of these X-ray flashes were also detected by BATSE, and these properties were similar to long GRBs (Kippen et al. 2001[15]).

Heise et al. 2001[7] investigated the statistical properties of the 17 X-ray flashes (XRFs) observed by WFC. Figure 2.2 shows the duration distribution of detected XRFs and the distribution of spectral photon index vs. peak flux. These distribution shows that the properties of XRFs and GRBs are distributed continuously with no clear separation. They concluded that the XRFs displayed properties that are in all aspects a natural extension of those of GRBs.

2.7 HETE-2

The High Energy Transient Explorer 2 (HETE-2) was a first astronomical satellite dedicated to observe GRBs. HETE-2 was launched on October 9, 2000 by a Pegasus rocket. This satellite had three types of GRB detectors. The french gamma telescope (FRE-GATE) for spectroscopy and triggering of GRBs in the gamma-ray band, the Wide-Field

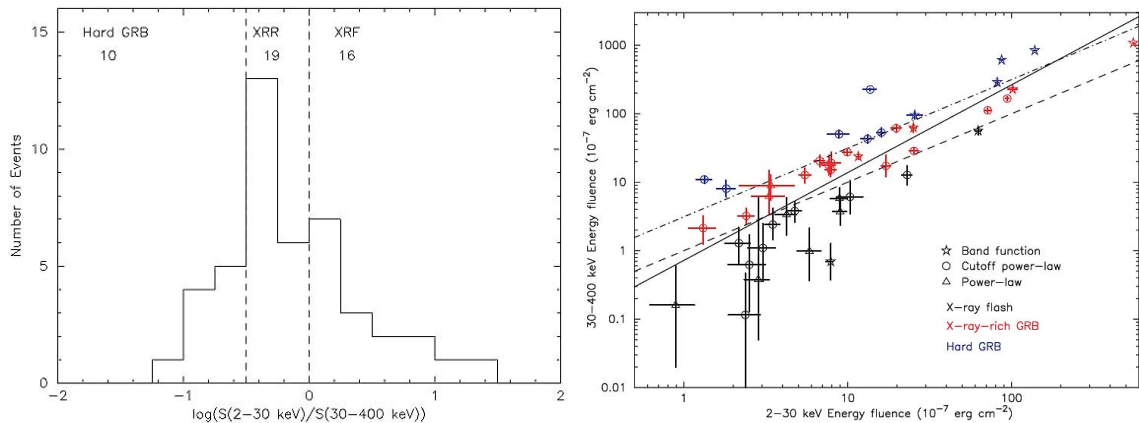


Figure 2.3: Left panel shows the distribution of the fluence ratio of HETE transients. Sakamoto et al. 2005[8] classified these events by this definition. Right panel shows the distribution of these bursts on the high and low fluence.

X-ray monitor (WXM) for spectroscopy, timing, and localization in the X-ray band, and the Soft X-ray Camera (SXC) for fine localization. FREGATE had a wide range of field of view (70 degree^2) and its effective area of 160 cm^2 with the energy range of $6\text{--}400 \text{ keV}$. WXM consisted of two sets of one-dimensional position sensitive proportional counters and the coded mask aperture. The two sets were placed orthogonal to each other to determine two-dimensional direction. WXM was sensitive in the energy range of $2\text{--}25 \text{ keV}$, had an effective area of about 80 cm^2 in each counter, and GRB localization accuracy of about 10 arcminutes.

Sakamoto et al. 2005[8] investigated the properties of XRFs in the HETE data. They analyzed 45 GRBs obtained by its 3 years operation, and they characterize these GRBs by its fluence ratio $S_x(2\text{--}30 \text{ keV}) / S_\gamma(30\text{--}400 \text{ keV})$. GRBs, XRRs (X-ray rich GRBs), and XRFs were classified as the left panel of figure 2.3. The right panel of figure 2.3 shows the fluence distribution of these bursts. They investigated several properties of these bursts. As the result of these comparisons, they concluded that the properties of GRB, XRR and XRF formed continuum, and there was no clear intrinsic distinction among them.

2.8 Summary

We summarize the past studies of short X-ray transients in table 2.1. Arefiev et al. 2003[11] assembled archival data from Ariel V, HEAO I, WATCH, ROSAT, and Einstein. They fitted assembled $\text{Log}N\text{-Log}S$ plot, and obtained a power-law index of -1.0 . They

concluded that the measured index results from mixture of multiple classes of sources, with the major contribution from GRBs and stellar flares. The interpreted the flat distribution mainly as due to the GRBs (figure 2.4 as was the case of the BATSE result (pendleton et al. 1996[16])). However, some fraction of FXTs was attributed to non-GRB sources, such as magnetic stars.

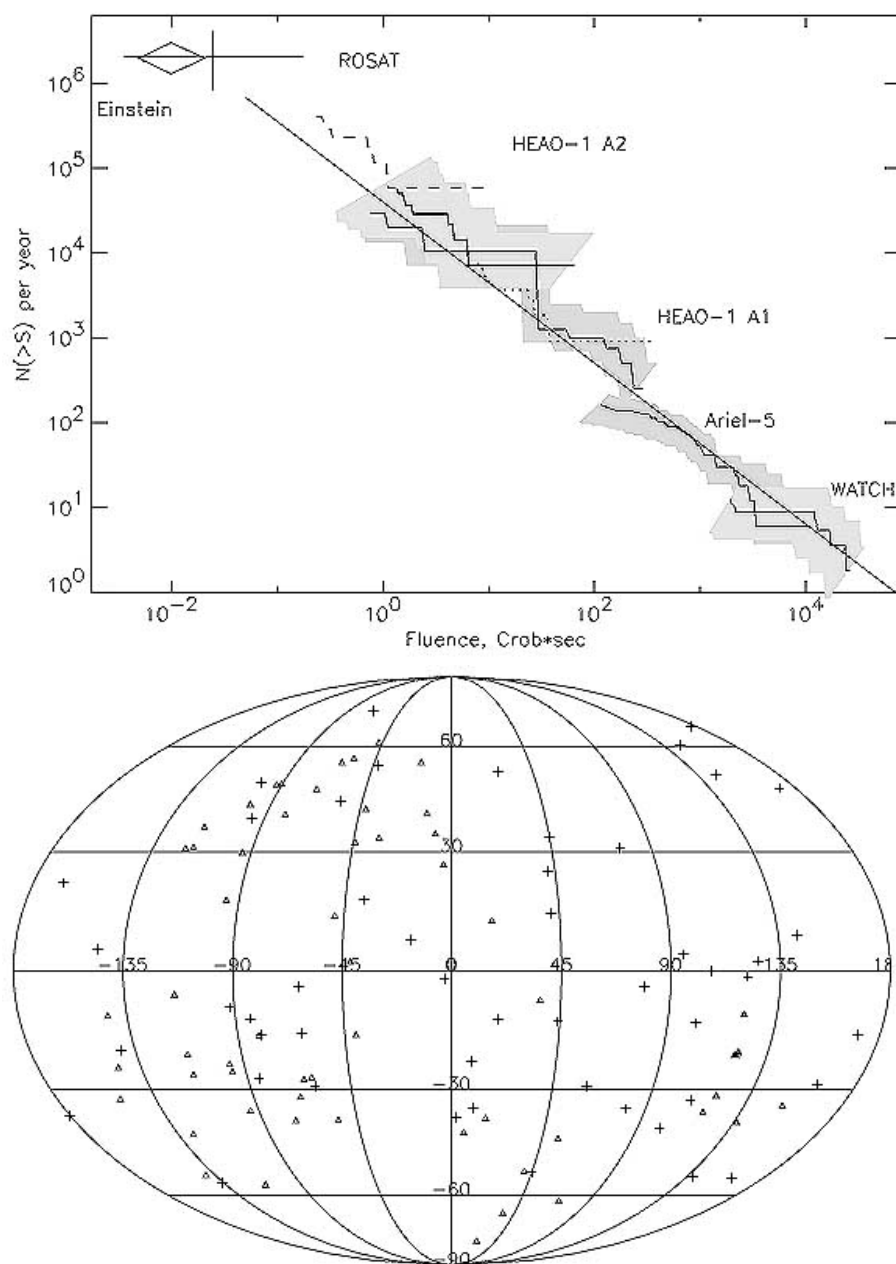


Figure 2.4: Arefiev et al. 2003[11] summarized fast X-ray transient search. The top panel shows the $\text{Log}N\text{-Log}S$ distribution with merged each satellite. This distribution fitted by the power-law function with index of -1.0. The bottom panel shows the spatial distribution for each satellite. Fast X-ray transients are uniformly distributed on the whole sky.

Table 2.1: Comparison of the performance and results for each satellite.

Satellite	FoV ^a	F_{lim} ^b	Energy range	Sample/year
HEAO-I	0.0097 %	4.0 mCrab	0.5–20 keV	18 FXT ^c s/1.5 yr
Ariel V (SSI)	0.0181 %	20 mCrab	2.0–20 keV	27 FXTs/5.5 yr
Einstein (IPC)	0.0076 %	0.04 mCrab	0.4–4.0 keV	42 FXTs/2.5 yr
Glanat (WATCH)	75 %	900 mCrab	8.0–15 keV	6 FXTs/9 yr
ROSAT (PSPC)	0.0076 %	0.04 mCrab	0.1–2.5 keV	23 FXTs/8.5 yr
BeppoSAX (WFC)	0.097 %	400 mCrab	2.0–28 keV	17 XRFs/6 yr
HETE-2 (WXM)	12.73 %	90 mCrab	2.0–25 keV	45 GRBs/3 yr
MAXI (GSC)	2.33 %	50 mCrab	4.0–10.0 keV	29 FXTs/1.25 yr

^a A ratio between the field of view and whole sky.

^b Limited sensitivity of each detectors.

^c FXT is an acronym for first X-ray transient.

Chapter 3

Short X-ray Transients

In this chapter, we describe the short transient isotropically distributed in the sky. Since our main target is the sources of unknown origin, we do not deal with the classes of transients that occur in the galactic plane.

3.1 Gamma-ray Bursts

Gamma-ray bursts (GRBs) are the brightest transient in the universe. Its total emission energy is about 10^{52} erg. The first detection of GRB is observed by the U.S. satellite Vela (Klebesadel et al. 1973[17]). Vela was the military satellite monitoring nuclear experiments in the space around the Earth. Vela detected a few unknown Gamma-ray events from the direction not in the neighborhood of the Earth. More likely, they had origins in the Universe.

A significant advance in the studies of GRB was achieved by Burst and Transient Source Experiment (BATSE) on-board the Compton Gamma Ray Observatory (CGRO) launched in 1991. BATSE confirmed the GRB properties of angular distribution, duration time distribution, spectral properties, and occurrence frequency. The distance of GRBs is confirmed by the discovery of afterglow by BeppoSAX. The spectral properties at low energy range was investigated by HETE-II satellite, leading to the conclusion that the origins of X-ray flashes and GRBs are common. Currently, a fleet of spacecrafts, Swift, Suzaku, Kounus-Wind, and Fermi, are operated for detection of GRBs. Although a large amount of data of GRB has been obtained, the central engine of GRBs has not been understood yet.

The duration of prompt emission of GRBs are a few to a few 1000's seconds in the observed frame, and their light curves show a large variety. Occurrence frequency of GRB is about one event in a day with the sensitivity of BATSE. Most of GRB have the same

spectral shape and the spectra are well fitted by the BAND function[18]. 90 % of GRBs has afterglow emission, after the prompt burst in the broad energy band (X-ray to radio band). According to the spectra obtained by optical telescope, most of GRBs occur at cosmological distances ($z > 1.0$). Thus, the distribution of GRBs is uniform in whole sky. The highest spectroscopically confirmed redshift of GRBs is $z = 8.2$ for GRB090423[19]. GRB090429 were also detected at even higher redshift of $z = 9.4$ [20], though its redshift value is estimated based on multicolor photometry.

GRBs properties are summarized as following.

1. Short duration time (10 ms \sim 1000 s).
2. Broad energy ranges (few keV \sim few MeV).
3. The spectra well fitted by Band function (Band et al. 1993[18]).
4. Uniform distribution in whole sky.
5. Spatial distribution in cosmological distance.
6. Afterglow emission with broad energy band.

3.1.1 Prompt Emission

Duration Time

The duration time of GRBs are defined based on the integrated number of photons of in the prompt emission of bursts. T_{50} is defined at the time of obtaining the middle 50 % (from 25% to 75% in the integrated photon light curve) of the total photons, and T_{90} is the time for obtaining the middle 90 % of the total photons.

Figure 3.1 shows the distribution of GRB duration time T_{90} obtained by BATSE during the nine year mission (BATSE web[21]). Two broad peak distributions can be seen clearly. These peak times are 0.3 s and 40 s respectively, and minimum point between two peaks is placed on 2 s. GRBs are characterized as two types of origin by these duration times. The “Short GRBs” with duration time less than 2 s are considered that it is generated due to the merger of neutron stars.

Spectral Properties

The spectral properties of the prompt GRBs were studied in detail BATSE on the CGRO satellite.

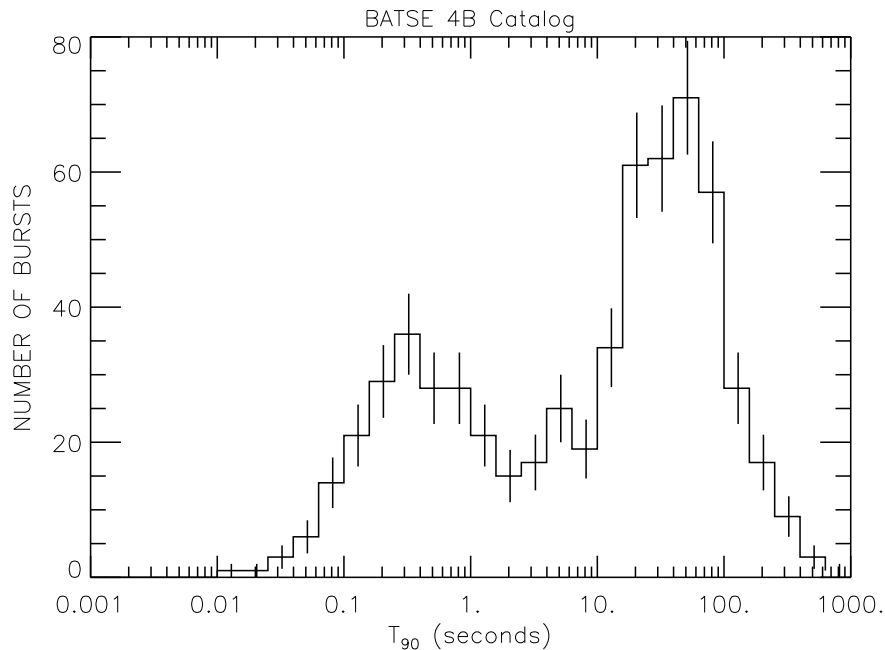


Figure 3.1: Distribution of GRB duration obtained by BATSE during the nine year mission (BATSE web[21]). A clear two broad peak distribution can be seen. These peaks appear centered around 0.3 s and 40 s with the minimum about 2 s.

Although light curve of GRBs have various shape, the most of GRB spectra are well fitted by the Band function[18]. The Band function is described as following equation.

3.1

$$\begin{aligned}
 N(E) &= A \left(\frac{E}{E_0} \right)^\alpha \exp \left(\frac{-E}{E_{peak}} \right) && [(\alpha - \beta)E_{peak} > E] \\
 N(E) &= A \left(\frac{(\alpha - \beta)E_{peak}}{E_0} \right)^{\alpha - \beta} \exp(\beta - \alpha) \left(\frac{E}{E_0} \right)^\beta && [(\alpha - \beta)E_{peak} \leq E] \quad (3.1)
 \end{aligned}$$

Where, A is a constant value, E_{peak} is the peak energy at the spectral energy distribution, α is the spectral index at the low energy band, and β is the index at high energy band. E_{peak} is tightly concentrated around 250 keV, and α and β are clustered around -1 and -2.5 respectively.

3.1.2 Statistical Properties of GRB

Angular Distribution

GRBs are distributed isotropically in whole sky because it occurs at the cosmological distance. This information was also obtained by BATSE.

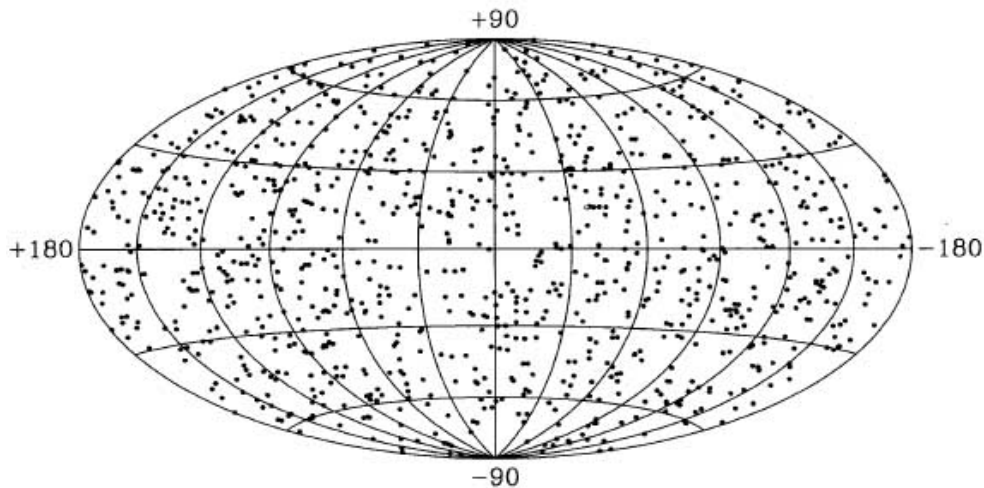


Figure 3.2: Angular distribution of GRBs on the galactic coordinate obtained by BATSE during the nine year mission (Briggs et al. 1996[22]). The distribution of GRBs are not clustered along the galactic plane but distributed isotropically.

Figure 3.2 shows the distribution in galactic coordinates of 1005 GRBs from the 3rd BATSE catalog (Briggs et al. 1996[22]). While the isotropic distribution had been reported by Atteia et al. 1987[23] previously. BATSE provide two new crucial features: the high sensitivity of the instrument and the large size of the sample. The isotropy of the weakest GRBs that are too faint to localize by the previous instrument could be check using the BATSE data.

The dipole and quadruple moments of BATSE GRBs were also calculated by Briggs et al. 1996[22] with considering all observation biases. As the result of this test, weakest GRBs are perfectly distributed isotropically, just like the celestial distribution of bright GRBs. These results also confirmed that the distribution of short GRBs is isotropic as long GRBs.

V/V_{max} Distribution

V/V_{max} test is proposed by Schmidt et al. 1988[24]. This method provides a quantitative evaluation for the uniformity of the radial distribution of objects in a well-defined sample. Detection schemes of V/V_{max} method are based on counts rather than peak energy flux or time integrated energy flux.

At first, we define the limiting count of C_{lim} which is determined as the detection limit of instruments. If the minimum signal to noise ration is set at n_{σ} , then the limiting count

C_{lim} is defined as

$$C_{lim} = n_{\sigma} \sqrt{N_b} \quad (3.2)$$

C_{lim} is defined by the Poisson statistics for the background count N_b . Assuming the Euclidean space, the observed peak count of a source C (subtracted background) will depend on its distance as r^{-2} ,

$$r_{max} = r \left(\frac{C}{C_{lim}} \right)^{1/2} \quad (3.3)$$

We characterize the radial location of the source by the ratio of the volume V contained within the radius r and the volume V_{max} contained within the radius r_{max} . The ratio is (r/r_{max}) , thus

$$V/V_{max} = \left(\frac{C}{C_{lim}} \right)^{-3/2} \quad (3.4)$$

If the sources uniformly distribute in space, the distribution of V/V_{max} should be uniform over the range 0.0 to 1.0. In this case, the mean value $\langle V/V_{max} \rangle$ should be 0.5. The error of $\langle V/V_{max} \rangle$ calculated by the r.m.s. will be $(12n)^{1/2}$, where n is the number of sources. Pendleton et al. 1996b[16] found $\langle V/V_{max} \rangle = 0.329 \pm 0.011$ with the BATSE 3B Catalog (more than 1122 GRBs), which is 15σ away from the value of 0.5. In addition, Kouveliotou et al. 1993[25] found $\langle V/V_{max} \rangle = 0.367 \pm 0.030$ and $\langle V/V_{max} \rangle = 0.302 \pm 0.038$ for long and short bursts respectively. These results indicate that the GRBs are distributed in cosmological distance that represents the red-shift effects. The evidence of such distribution is confirmed by the discovery of afterglows and determined the distance of GRBs.

LogN-LogS Distribution

The integrated number of transients N increases with the distance from the earth r , and observed flux S decreases inversely with square of the distance ($S \propto r^{-2}$). Therefore, the observed flux S is correlated with integrated number of the transients N . This distribution is called ‘‘LogN-LogS distribution’’. If the transients uniformly distributed in the Euclidean space ($N \propto r^3$), these correlation become parallel to the index with $-3/2$ on the double logarithmic plot ($N \propto S^{-3/2}$).

Figure 3.3 shows the LogN-LogS distribution of GRBs detected by BATSE. GRB can be seen the brightest emission from the cosmological distance. The Euclidean space is expanded in the cosmological distance by the red-shift effects. Therefore, the shape of LogN-LogS distribution of GRBs is not be index of $-3/2$ at the lower flux, and dim

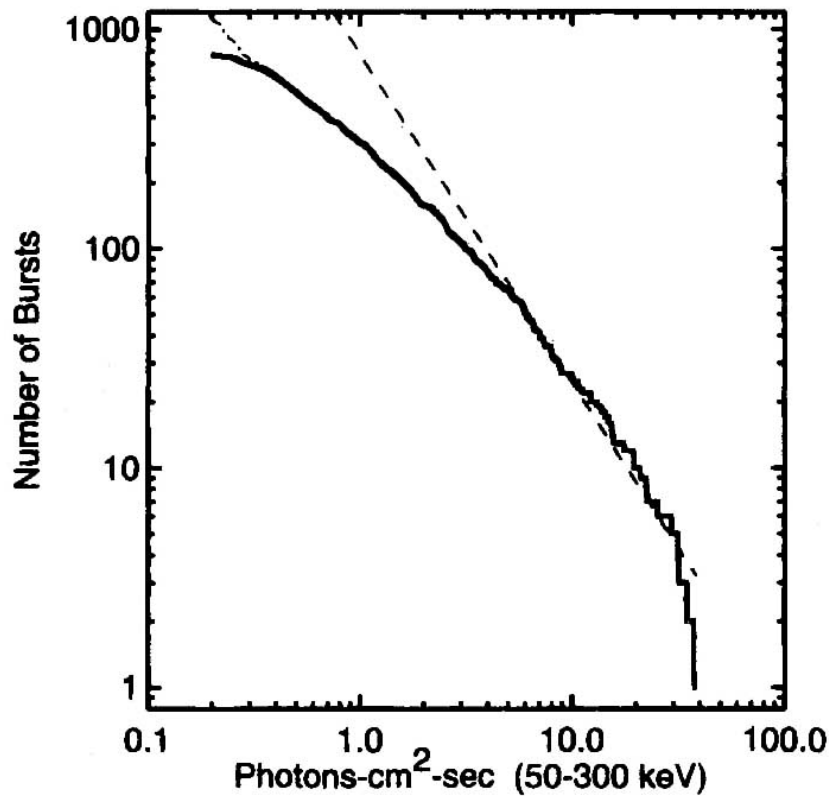


Figure 3.3: LogN–LogS distribution of GRBs detected by BATSE. The horizontal axis shows the peak flux of prompt emission. GRBs occur at the cosmological distance, dim events are decrease by the effects of the redshift.

events (remote events) are decrease. This means that if we observe GRBs by a detector with the small range of sensitivity, the index of the distribution could be seen between $-3/2$ and -1 . Thus we need the wide range of sensitive detector as BATSE. The only GRBs shows such distribution as figure 3.3. Since the other object, for example, AGNs are dimmer than GRBs, we can see only the bright near source which is not affected red-shift. Thus the LogN-LogS distribution of these objects with a index of $-3/2$.

Arefive et al. 2003[11] shows the LogN-LogS distribution in the soft X-ray band assembled by past satellite emissions, and they said that the dominant sources of the distribution is GRBs and flare stars by their distribution results with index of -1.0 . However, the large amount of statistic LogN-LogS distribution in the soft X-ray band as BATSE in the hard X-ray band has not been yet, and be waited.

3.1.3 X-ray Flash

X-ray flashes are one of the soft X-ray transients, and its properties are similar to GRBs.

BeppoSAX found the some X-ray transients detected by WFC but do not detected by GRBM (Heise et al. 2001[7]). They call these events ‘X-ray flashes (XRFs)’. Kippen et al. 2001[15] searched for these transients in BATSE data, and found the counterpart in the γ -ray range. However these flux in γ -ray band was not brighter than X-ray band.

The properties of XRFs are investigated in detail by Sakamoto et al. 2005[8] using the low energy data observed by WXM on board the HETE-II. They analyzed 45 transients obtained in the HETE-II operation. These transients are characterized based on the fluence ratio $F = S_x(2 - 30 \text{ keV}) / S_\gamma(30 - 400 \text{ keV})$. GRBs, XRRs, and XRFs are classified as the ($F < -0.5$), ($-0.5 < F < 1.0$), and ($F > 1.0$) respectively. They finally showed that XRFs and GRBs differ only by their E_{peak} , while they have similar durations and spectral indices. Their investigation confirmed that XRFs are soft GRBs.

The redshift of several XRFs have been measured, and the range of redshift is similar to GRBs. Thus, this fact demonstrates that XRFs are not highly redshifted GRBs. In addition, all these events are appear compatible with the $E_{peak} - E_{iso}$ relation for GRBs. The spectral and temporal properties of XRFs, and their range of redshift suggest a common physical origin with GRBs.

The detection frequency of XRFs depends on the sensitivity of the detector in the X-ray band and its E_{peak} . Therefore, the frequency of XRFs are considered as similar to or a few larger than that of GRBs. The $\text{Log}N\text{-Log}S$ distribution of XRFs may probably shifts to the upper region than that of GRBs.

3.1.4 GRB Afterglows

After an GRB occurrence, dim and long emission is emanated in the soft X-ray band to optical band at the point of GRB. This counterpart is called “afterglow”

The first X-ray afterglow were discovered by Beppo-SAX for GRB970228 (Costa et al. 1997[26]). This discovery was one of the most important break through of the study of GRBs. Figure 3.4 shows the X-ray images of discovered afterglow of GRB970228. The time variation of the X-ray flux of the afterglow was also measured. The X-ray flux decayed by the power-law with index -1.32 . The discovery of X-ray afterglow provided that the position of GRB were so accurate that an optical telescope can observe the position of GRB. Soon after this discovery, optical telescope also discovered the counterpart of GRB090228 (Paradijs et al. 1997[27]). Optical observations confirmed the presence of host galaxy and established its cosmological redshift. The measured value of redshift z

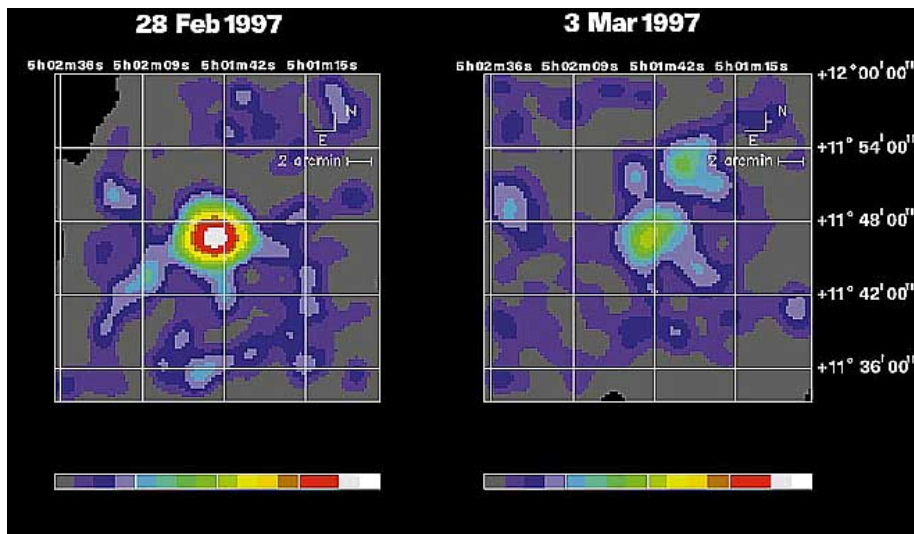


Figure 3.4: The X-ray image (2-10 keV) of the first discovered afterglow of GRB970228 observed by Beppo-SAX (Costa et al. 1997[26]). Left panel shows the image of afterglow at 8 hours after the burst, and right panel shows the image at 3.5 days after the trigger.

confirmed that GRBs occurred in the cosmological distance.

The X-ray afterglow was observed by 90 % of GRBs. Figure 3.5 shows the typical light curve of X-ray afterglows. The typical brightness of the afterglow is $10^{-8} \sim 10^{-12}$ erg cm $^{-2}$ s $^{-1}$ with Swift XRT energy range (0.3–10.0 keV) which is corresponding to 10 mCrab \sim few *mu*Crab. The typical duration of X-ray afterglows is $\sim 10^5$ s for the XRT sensitivity. The bright phase (which can be detected by MAXI GSC) of afterglow is typically few 100 s (which depends on the decay index of light curve) after prompt bursts. Therefore, the scan frequency of the afterglow candidates should be larger than that of prompt GRBs and flux distribution of detected afterglows should be distributed dimmer region in the Log*N*-Log*S* distribution.

3.1.5 Off-axis Model

Yamazaki et al. 2002[28] proposed the model for XRF in which the observed angle is much larger than the collimation angle of the relativistic jet. In this model, the high X-ray to γ -ray fluence ratio is due to the relativistic beaming factor $\delta \equiv \gamma[1 - \beta \cos(\theta_v - \Delta\theta)]$ changing as a function of off-axis angle. Both the peak flux ratio and the fluence ratio increase as the observed angle increase.

According to this model, E_{peak} energy of GRBs (~ 250 keV) is shifted to low energies because of the smaller relativistic beaming effect. Thus E_{peak} can be estimated as $\sim \nu'_0 /$

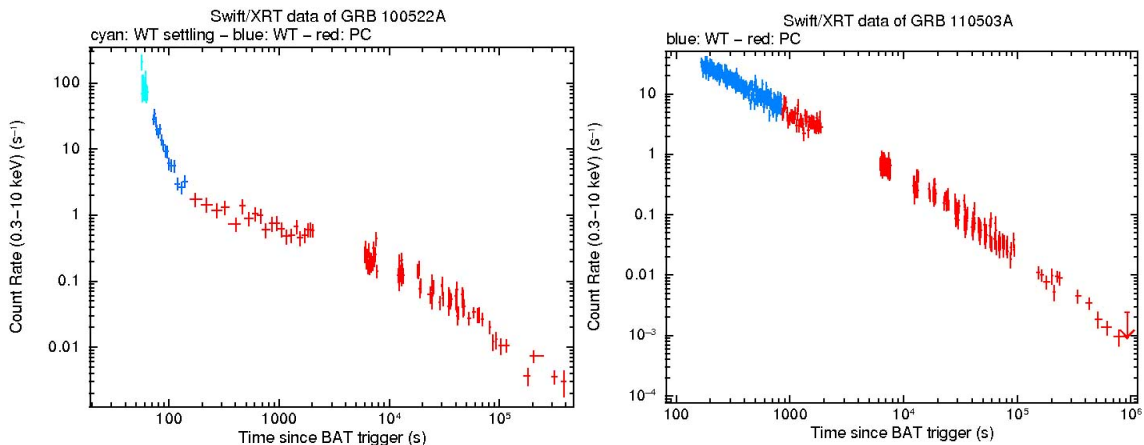


Figure 3.5: The typical light curve of X-ray afterglow. Left panel shows the afterglow with three phase of decay. Right panel shows the single power low decay afterglows. The most of X-ray flash has afterglows with the single power low decay as the right panel.

δ , where $\delta \equiv \gamma[1 - \beta \cos(\theta_v - \Delta\theta)] \simeq [1 + \Gamma^2(\theta_v - \Delta\theta)] / 2\Gamma$ and $\theta_v > \Delta\theta$.

In this model, since the fluence at the E_{peak} is proportional to δ^{-3} , XRFs should not be at high redshift. And the value of $\langle V/V_{max} \rangle$ for XRF is obtained by Heise et al. 2001[7] with 0.56. However, Heise et al. 2004[29] revisited the XRF data and updated the value of $\langle V/V_{max} \rangle$ to 0.27. This number is very close to $\langle V/V_{max} \rangle$ of classical GRBs. This suggests that XRFs could be at large cosmological distances. Yamazaki et al. 2004[30] changed some model parameters of their off-axis model and found that a hard GRB at viewing angle of 0.05 with a half opening angle of 0.03 could be an XRF with a red-shift of 1.5.

3.1.6 Orphan Afterglows

Since the majority of GRB jets are not directed toward us, most GRBs are seen as off-axis. Off-axis GRBs are possibly detected as afterglows which does not have prompt emission. These GRB afterglows with invisible prompt emission are called 'orphan afterglows'. The GRB collimation can be constrained by afterglow searches in X-ray, visible and radio wavelengths.

A search for orphan afterglow in X-ray band was performed by Greiner et al. 2000 [6] in the ROSAT all-sky survey data. They found no convincing candidate in this search, and the authors concluded that the beaming angle of afterglows and prompt emission is comparable in the X-ray band. With the sensitivity of ROSAT, it could only detect bright afterglows in the first few hours after the GRB detection when the jet has not spread out

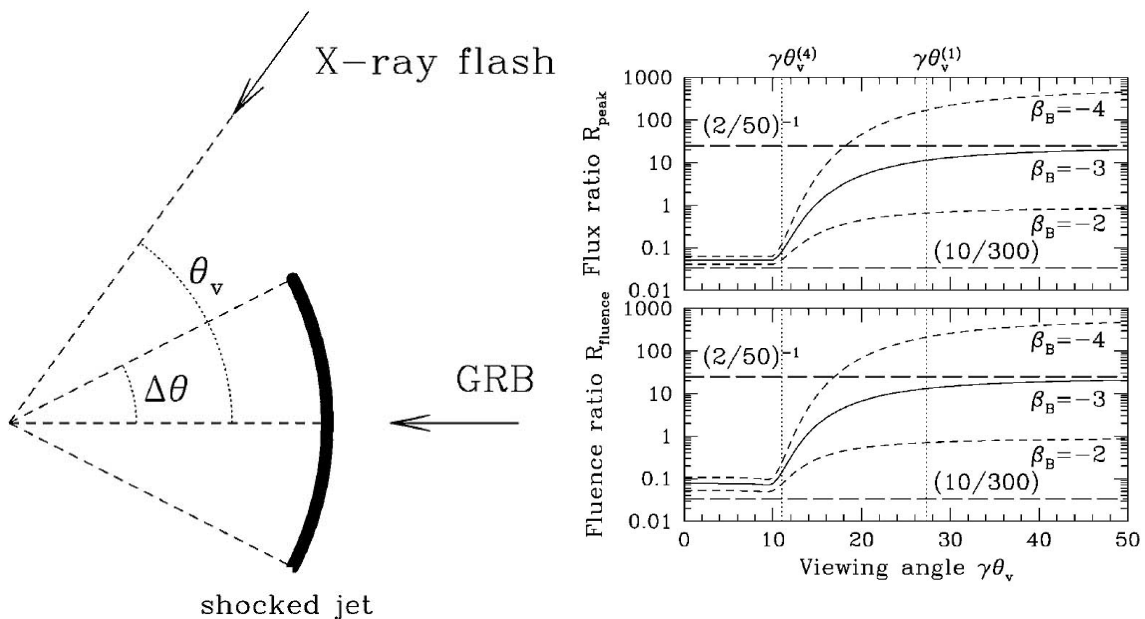


Figure 3.6: Left: The schematic view of the off-axis model. Right: The peak flux ratio (upper panel) and fluence ratio (lower panel) of 2–10 keV and 50–300 keV as a function of viewing angle (Yamazaki et al.(2002)[28]).

significantly. Therefore, event rates of orphan afterglows are quite a few events comparing with rests of prompt GRB in X-ray band.

The typical X-ray light curve of afterglows which has three decay phases (steep, shallow and normal), and if we could see the orphan afterglow as off-axis of the GRB in X-ray band, it is observed after the normal decay. The typical brightness of the afterglow in the normal decay phase is 10^{-12} erg cm $^{-2}$ s $^{-1}$ (0.3–10.0 keV) as bright as possible. Thus, the pointing observation with the X-ray telescope is needed for detection of the orphan afterglow in a X-ray band. On the other hand, Sakamoto et al. 2005[8] reported that the most of the shape of typical light curve of XRFs is single power-law decay whose power-law index corresponding to normal decay. In this case, we can probably see an afterglow emission that a jet break of the emission has already occurred. Thus the some level of bright orphan afterglows should be seen in this case. However the orphan afterglows has not observed yet in any energy band (radio, optical, X-ray).

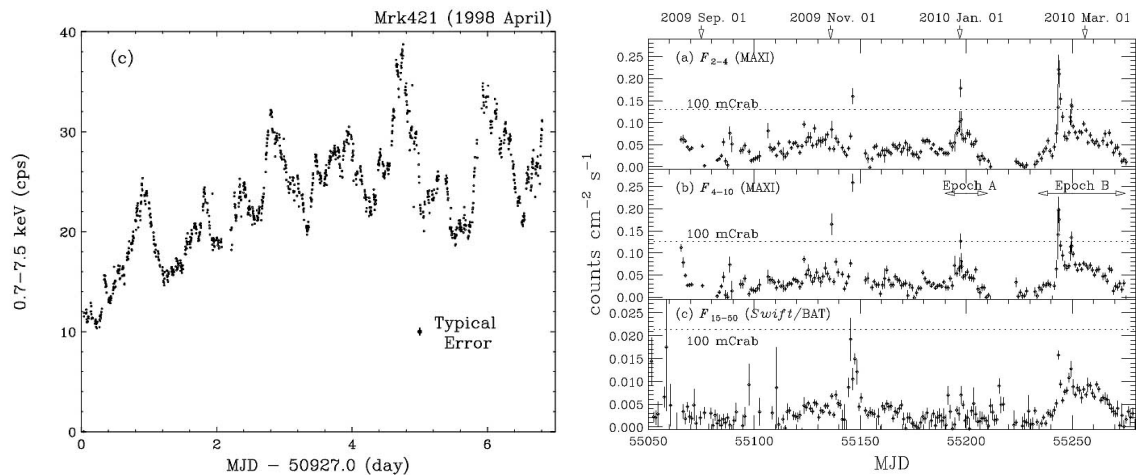


Figure 3.7: The light curve of Markarian 421. Left panel shows the light curve observed ASCA (Kataoka et al. 2001[33]) and right panel shows the light curve observed by MAXI GSC (Isobe et al. 2010[35]).

3.2 Other X-ray Transients

GRBs are not the only transients that are detected in the soft X-ray band. In this section, we will describe the other transients that have short time scale and could be detected in a single scan by MAXI/GSC.

3.2.1 Jet from BL Lac

The blazar is one of the candidate classes of X-ray transients. The blazar is a class of Active Galactic Nuclei that emanate relativistic jet in to line of sight. BL Lac object is a class of blazar, and characterized by rapid and large-amplitude flux variability and significant polarization at radio and optical frequencies. Markarian 421 is one of the most investigated BL Lac objects and its spectral energy distribution (SED) peaks in the X-ray band. This object is also one of the brightest extra-galactic sources at the very high energy (VHE) gamma-ray band above 100 GeV.

ASCA observed Markarian 421 five times with a net exposure of 546 ks (~ 6 days) both 1993 and 1998 (Takahashi et al. 1996, Takahashi et al. 2000, Kataoka et al. 2001, Tanihata et al. 2001 [31, 32, 33, 34]). In these observation, the Maximum intensity variation of Markarian 421 was about 3 times of the lower state (Figure 3.7).

The GSC also has observed Markarian 421 and detected the brightest outburst (164 ± 17 mCrab) in 2010 February (Isobe et al. 2010[35]). In the case of the brightest outburst

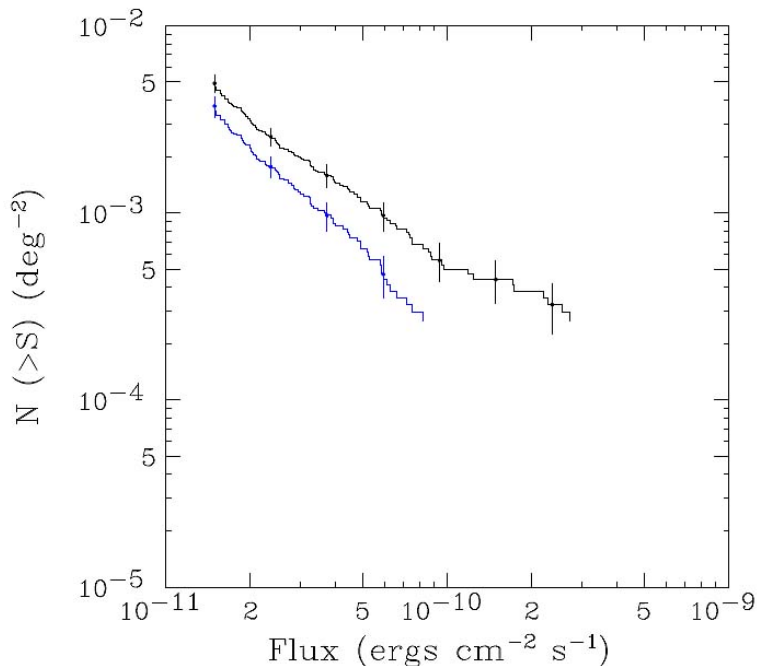


Figure 3.8: Log N -Log S distribution for all X-ray sources (black line) and AGNs (blue line) detected by MAXI/GSC (Hiroi et al. 2011[36]). AGNs are distributed by power-law with index $-3/2$.

of the Markarian 421, the time scale of the outburst is $\sim 10^5$ s for decay time, and the maximum brightness is about 10 times of steady phase.

The Log N -Log S distribution of Active Galactic Nuclei observed by MAXI/GSC is reported by the Hiroi et al. 2011[36]. Figure 3.8 shows the Log N -Log S distribution of AGN. Here, we assume that a bright outburst with 10 times of steady phase occurs per year for all of these AGNs. The Log N -Log S distribution of the outburst shifts to 10 times of flux on figure 3.8 (The maximum value of flux is about 1.0×10^{-9} erg s $^{-1}$ cm $^{-2}$). On the other hand, the limited sensitivity of a single scan of MAXI/GSC is about 5×10^{-10} erg s $^{-1}$ cm $^{-2}$ for 4.0-10.0 keV energy band. Thus, the contribution of the flare from BL Lacs (AGNs) for Log N -Log S distribution of transients are few events per year at the maximum sensitivity of MAXI/GSC.

3.2.2 Active Star Flare

Flares from active stars are also candidates for short X-ray transients. The X-ray emission is emanated by the flare of a star that is distributed in the close area (≤ 100 pc) from the solar system.

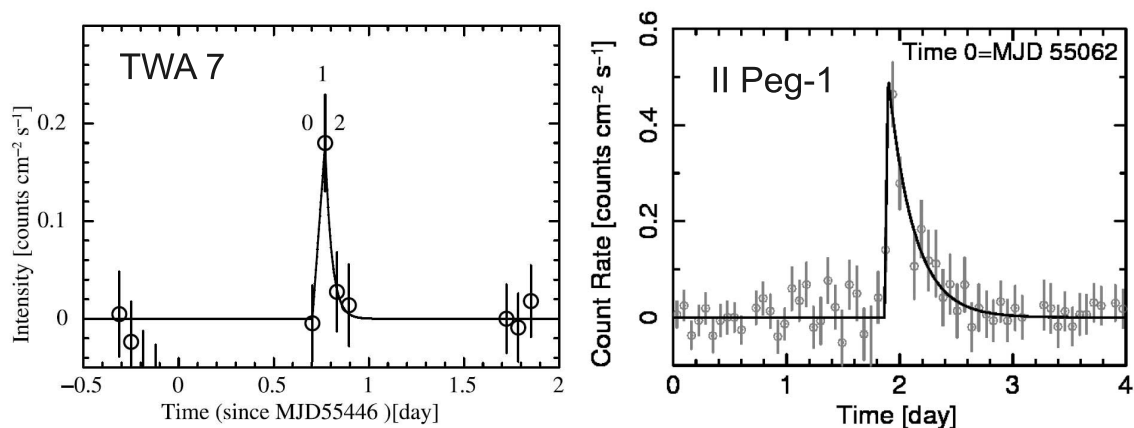


Figure 3.9: An example of the light curve of the flare stars. Left panel shows the light curve of TWA 7[37], and right panel shows the light curve of II Peg[38]. The typical time scale of active star flare observed by MAXI/GSCs is from few hours to one day.

The one of the main objects of active star flares are T Tauri stars that are part of the Young Stellar Objects (YSOs). The X-ray flare from the star rapidly rises within 10–100 s, and slowly decays with the time scale of 10^4 – 10^5 s. The intensity of the X-ray flare is 100 – 10^6 times higher than the maximum class of solar flare. It is considered that such flares on a star occur by an activity of the magnetic field on the star as same as the solar flare. RS CVn systems are also main candidate of the flare stars. RS CVns are the close binaries and its orbital period is very short. The rapid rotation of stars of such systems intensifies the magnetic activity of each star. Due to the extreme magnetic environment, RS CVn systems typically emanate the large flare with the orders of magnitude in a broad energy band. Since the flare is caused by the magnetic fields of the surface of a star, the time scale and intensity of the flare from RS CVns are also as same as the solar flare. The dMe stars are also candidate of the X-ray transients that are emanated the X-ray emission by its large magnetic fields generated by the deep convection zone in the star.

MAXI/GSC has detected flare stars from T Tauri star (Uzawa et al. 2011[37]) and RS CVn (Yamazaki et al. in press[38]). MAXI observed 22 flares from 13 flare stars in 2 years operation. These are found by not single scan exposure but 1 day exposure [38] with energy range of 2.0–10.0 keV. Thus its brightness and the time scale of these events are relatively dimer and longer than that of GRBs. The example of light curve of the flare stars observed by MAXI GSC is shown in Figure 3.9.

We estimate the $\text{Log}N$ - $\text{Log}S$ distribution of active star flares using the observed data of MAXI/GSC. Yamazaki et al.[38] reports the maximum flux of the flare from active star

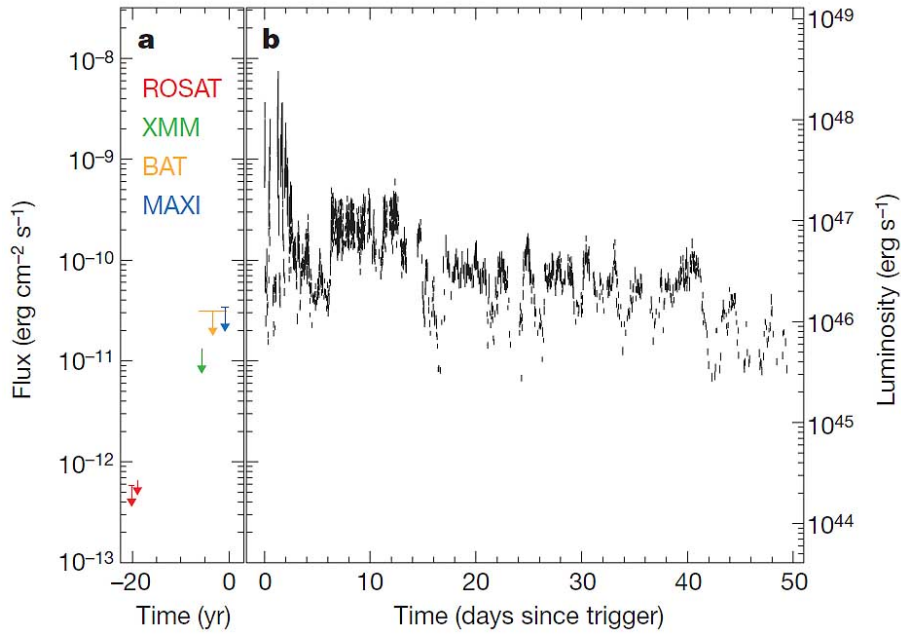


Figure 3.10: The light curve of Swift J164449.3+573451 detected by Swift/XRT (Burrows et al. 2011[9]). The left region **a** plotted the upper limit before the burst. The horizontal bars on each upper limit indicate the time interval over which they were calculated, and are placed at the value of the 3σ upper limit. All flux limits are calculated for the 1–10 keV energy band. The right region **b** is the light curve detected by Swift/XRT with the energy range of 1–10 keV.

is $L_{max} = 4.2 \times 10^{33} \text{ erg s}^{-1}$. Then we estimate the maximum distance that can observe the maximum flare using the detection limit of single scan of MAXI/GSC ($F_{min} = 1.0 \times 10^{-9} \text{ erg s}^{-1} \text{ cm}^{-2}$ for 2.0-10.0 keV) and the equation $L = 4\pi r^2 F$. The maximum distance of the observable flare is calculated with 190 pc, which is comparable to the thickness of the galactic plane. This means the stars that are spatially distributed in outside of the galactic plane with low density are invisible for the sensitivity of MAXI/GSC. Thus, the active star flare which can be observed by MAXI/GSC are distributed by simple power-law with index of $-3/2$ on a $\text{Log}N\text{-Log}S$ plot.

3.2.3 Tidal Disruption of a Star by the Supermassive Black Hole

Supermassive black holes have powerful gravitational fields with strong gradients that can destroy stars that get too close. It produces a bright flare in ultraviolet to X-ray energy band from stellar debris that forms an accretion disk around the black hole. These events are called “tidal disruptions”.

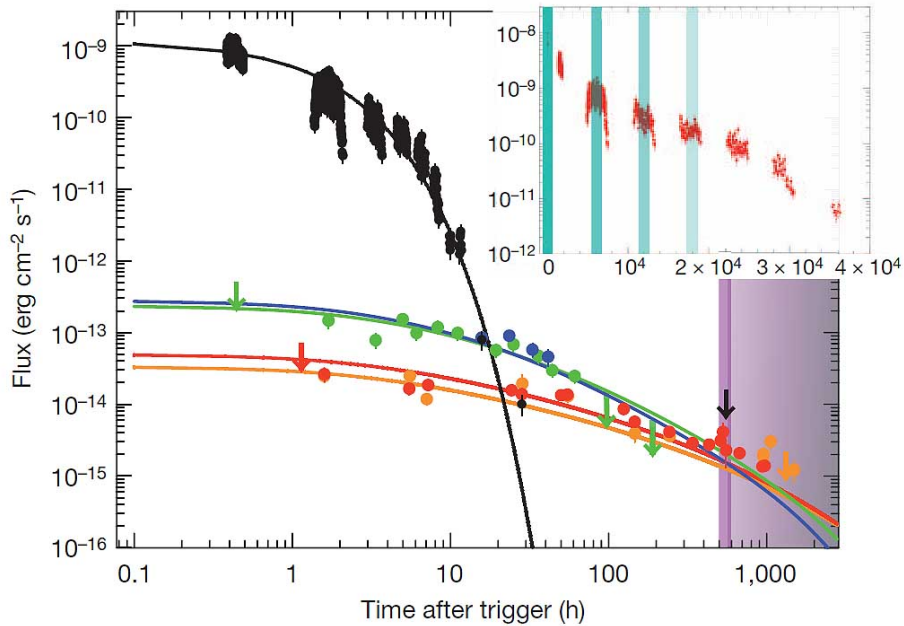


Figure 3.11: The light curve of GRB101225A detected by Swift/XRT (Campana et al. 2011[39]).

Swift/BAT discovered the short burst in hard X-ray band on March 28, 2011 as GRB110328A by its integrated isotropic energy of 2×10^{53} erg (1–10 keV), but its duration time and periodic light curve is not similar to the typical gamma-ray burst (Burrows et al. 2011[9] and Bloom et al. 2011[40]). This event was identified as the tidal disruption event by its properties of light curve and luminosities, and named Swift J164449.3+573451. Figure 3.10 shows the light curve of Swift J164449.3+573451. The left region **a** of the figure 3.10 shows the 3σ upper limit of the emission at the source point before the burst. The flux limits of each data are calculated for the 1–10 keV energy band. The right region **b** of the figure 3.10 shows the light curve of the source detected by Swift/XRT with 1–10 keV energy band.

GRB101225A were also reported as the tidal disruption events that the an asteroid was destroyed by the gravitation of a supermassive black hole (Campana et al. 2011[39]). The light curve and spectrum of the afterglow of GRB101225A are unusual comparing with that of typical gamma-ray busts (figure 3.11). Thone et al. 2011[41] proposed progenitor of GRB101225A is a merger of a helium star with a neutron star.

The frequency of these events is not able to estimate because of its low detection rate. Tidal disruption events are observed two events only. Additional detections are needed for investigation of the frequency and origin of these events. The X-ray transient search

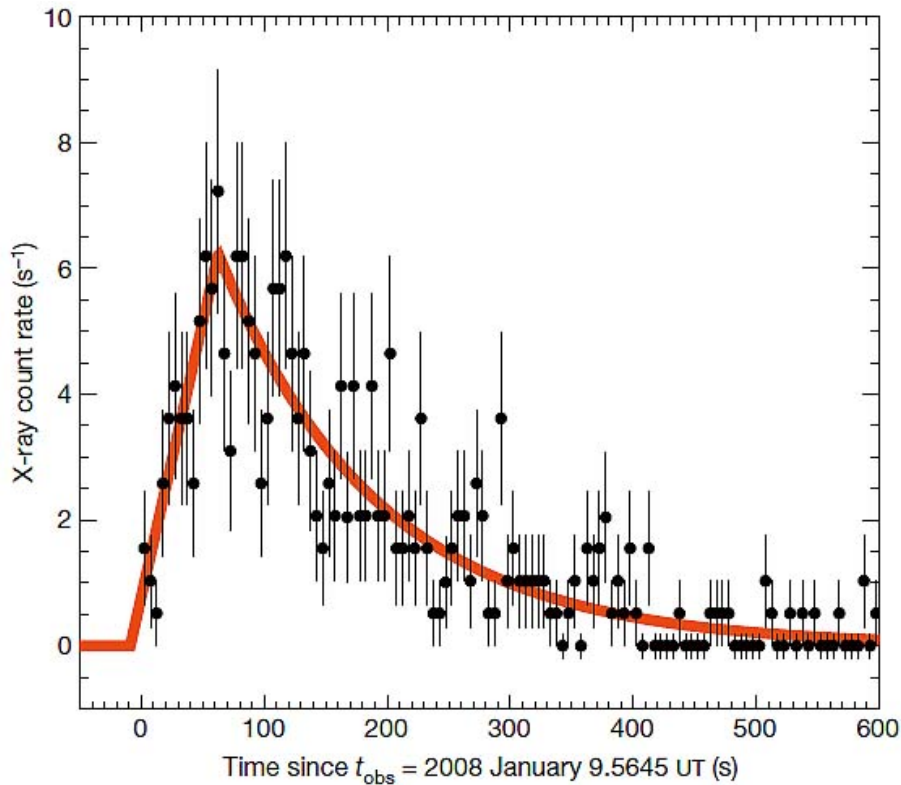


Figure 3.12: The light curve of XRO080109 detected by Swift XRT (Soderberg et al. 2008[10]). This light curve was well fitted by a fast rise exponential decay model (red curve). The best-fit parameters are a peak time of 63 ± 7 s after the beginning of the burst, an e-folding time of 129 ± 6 s, and peak count rate of 6.2 ± 0.4 count s^{-1} .

has a potential for detection of these events.

3.2.4 Super Nova Shock Breakout

In general, super novae were discovered mainly through their 'delayed' optical light (some days after the burst of neutrinos that marks the actual event). Prompt bursts of X-ray emission from a break out of the super nova shock wave through the stellar surface in the first moments after the explosion have been theoretically predicted (Colgate 1974[42], Klein and Chevalier 1978[43]), but their short durations (few 100 second) and the lack of sensitive wide-field X-ray searches have prevented their discovery until now.

The supernova shock breakout event had been observed only once by Swift X-ray telescope (XRT) on January 9, 2008 at 13:32:49 UT, Swift XRT serendipitously discovered an extremely bright X-ray transient (X-ray outburst 080109; XRO080109) during a scheduled observation of the galaxy NGC2770 (Soderberg et al. 2008[10]). Figure 3.12

shows the temporal evolution of XRO080109. The light curve was characterized by a fast rise and exponential decay and its time scale was about only 300 s. The X-ray spectrum was best fitted by a power-law ($N(E) = E^{-\Gamma}$) with a photon index of $\Gamma = 2.3 \pm 0.3$, and a hydrogen column density of $N_H = 6.9_{-1.5}^{+1.8} \times 10^{21} \text{ cm}^{-2}$, in excess of the absorption within the Milky Way. The estimated unabsorbed peak flux is $F_X \approx 6.9 \times 10^{-10} \text{ erg cm}^{-2} \text{ s}^{-1}$ (0.3–10.0 keV). On the γ -ray band (15–150 keV), they detected no counterpart for this burst and obtained the limit on the γ -ray fluence of $F_\gamma \leq 8 \times 10^{-8} \text{ erg cm}^{-2}$ (3σ), a factor of three times higher than an extrapolation of the X-ray spectrum to the γ -ray band.

Soderberg et al. 2008[10] calculated the rate of these events. They concluded that an all-sky X-ray satellite with sensitivity similar to that of the Swift/XRT would detect and localize several hundred of the explosion. We assume the detectable limit of MAXI/GSC and Swift of $1.0 \times 10^{-9} \text{ erg cm}^{-2} \text{ s}^{-1}$ and $5.0 \times 10^{-12} \text{ erg cm}^{-2} \text{ s}^{-1}$ for 40 s respectively (Burrows et al. 2000[44]), and these events are distributed with index of $-3/2$ on the $\text{Log}N$ - $\text{Log}S$. The rate of these events decreases from several hundred of events to few events per year ($1/1000 \sim 1/100$ of XRT detectable events). These events occur in the galaxy with a distance of less than 200 Mpc ($z \leq 0.05$). Thus, the estimated distribution of X-ray emission from super novae will be isotropic with index of $-3/2$ on the $\text{Log}N$ - $\text{Log}S$ plot.

Chapter 4

Monitor of All-sky X-ray Image

In this Chapter, we describe our instruments for all-sky monitoring.

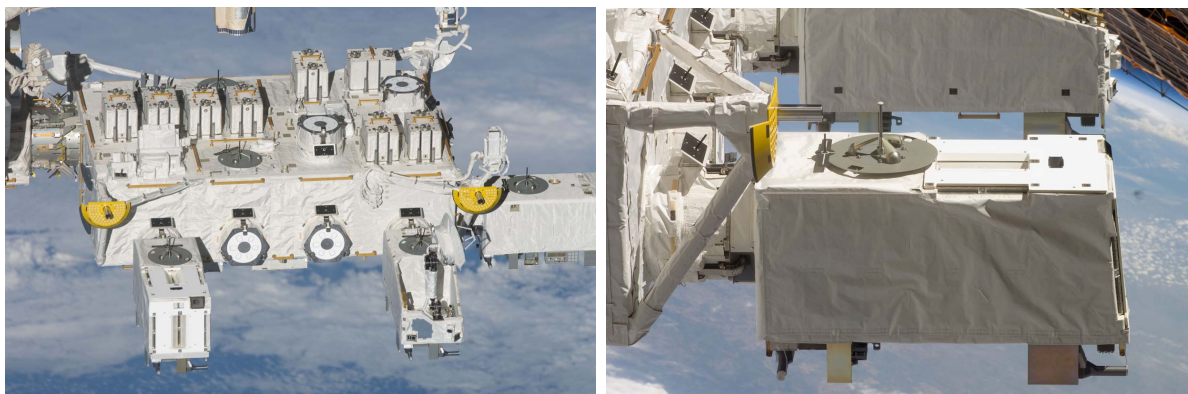


Figure 4.1: Picture of Monitor of All-sky X-ray Image (MAXI) installed on ISS-JEM)

Monitor of All-sky X-ray Image (MAXI) is the first astronomical mission operated on the International Space Station (ISS). The payload was delivered to the ISS by Space Shuttle Endeavor with the mission STS 127 on July 16, 2009, and installed on the Japanese Experiment Module “Kibo Exposed Facility” on July 24. MAXI has two kinds of cameras, Gas Slit Camera (GSC), and Solid-state Slit Camera (SSC). The instrument details of GSCs are described in Mihara et al. 2011[45], and its in-orbit performance is described in Sugizaki et al. 2011[46]. Tomida et al. 2011[47] and Tsunemi et al. 2011[48] describe the performance of the SSC on the ground and in-orbit respectively. The figure 4.2 shows the picture of the proportional counter of the GSC and the CCD camera of the SSC.

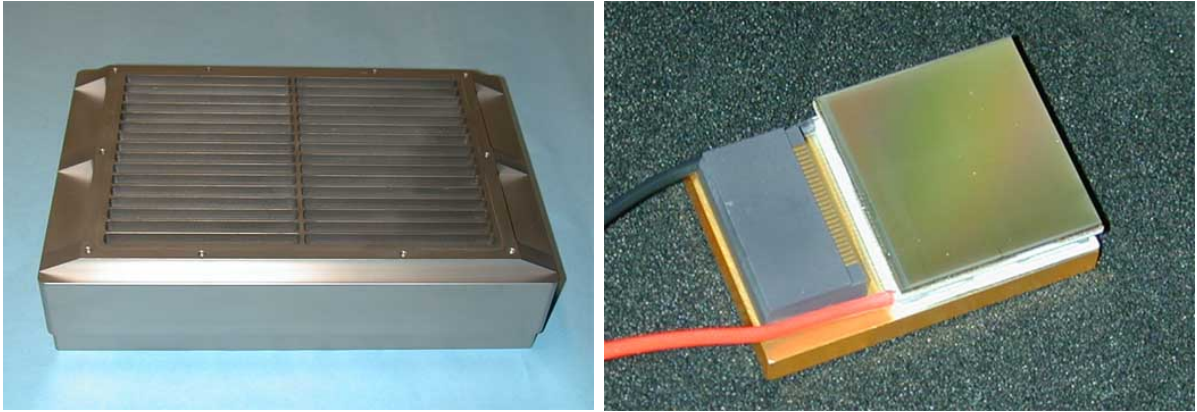


Figure 4.2: Pictures of a proportional counter of Gas Slit Camera (GSC) and a CCD camera of Solid-state Slit Camera (SSC)

4.1 Gas Slit Camera (GSC)

In this section, we describe the performance of Gas Slit Cameras (GSCs). We will show (1) the overview of the GSCs, (2) the total field of view for the all GSCs, (3) the principle of the position determination for X-ray sources, and (4) the detail of proportional counters.

4.1.1 Overview of GSCs

The GSC consists of twelve Xe gas one-dimensional position sensitive proportional counters and slit-slat collimators with the sensitivity in X-ray band.

The GSC constantly monitors the entire sky every 92 minutes using thin-long field of view (FoV) of $3.0^\circ \times 160^\circ$. A set of GSC cameras (six cameras in three pairs) covered the FoV centered at the direction of the motion of the ISS (the horizon view), and the other set covers the FoV centered at the zenith (the zenith view). Using these two independent FoVs, GSC can cover 86 % of the entire sky by a single scan period, even if they are turned off in the regions with high particle fluxes such as the South Atlantic Anomaly (SAA) and at high geographic latitudes ($> 40^\circ$). The detectable energy band of GSC is 2–30 keV and total effective area is designed to be 5320 cm^2 . Table 4.1 shows the summary of characteristics of GSCs.

4.1.2 Field of View

A set of GSCs covers the thin-long field of view of $3.0^\circ \times 160^\circ$. Two sets in horizontal and zenith directions covers two of such fields. We describe the field of view of all GSCs

in this subsection.

MAXI has twelve GSC units. Six of these GSCs are installed in the zenith (anti-earth center) side of MAXI and others are installed in horizontal side facing the ram direction (left panel of figure 4.3). The ID number of these GSC cameras are also shown in figure 4.3. The right panel of figure 4.3 shows the total field of view (160°) of the MAXI/GSC. The long dimension of the field of view of a single GSC unit is 80° , and the FoV for center cameras has overlap with the half of the FoV of the both side cameras. Because of such a thin-long field of view and the scanning observing mode, the sensitivity of GSCs for a single source is lower than that of collimated pointing instruments with narrow FoV in other missions. Among the all-sky monitors in X-ray band, however, the GSC has the highest sensitivity. In addition, GSC has an advantage that it can cover the whole sky in a day except for small regions near the sun and around the orbital poles.

4.1.3 Principle of the position determination

Each GSC camera is composed of a one-dimensional position sensitive proportional counter and slit-slat collimators. The GSC determines the X-ray incident direction in two dimensions: (1) the coordinate perpendicular to the scan direction is encoded in the signal position on the detector anodes, and (2) the other coordinates along the scan is encoded in the transit time which is defined by the narrowly collimated field of view as figure 4.4.

Table 4.1: Summary of GSCs.

Contents	values
Operation start	August 15, 2009
Detector	Gas Proportional counter
Number of Units	12 cameras
Energy Range	2.0–30.0 keV
Energy resolution	18% @ 5.9 keV
Spatial accuracy	0.2° @ 4.0–10.0 keV
Timing resolution	0.1 ms
Field of View	$3.0^\circ \times 160^\circ$
Effective Area	5350 cm ² (Total)
Orbital period	92 minute
Detection limit	50 mCrab (single scan with a GSC, 5σ)

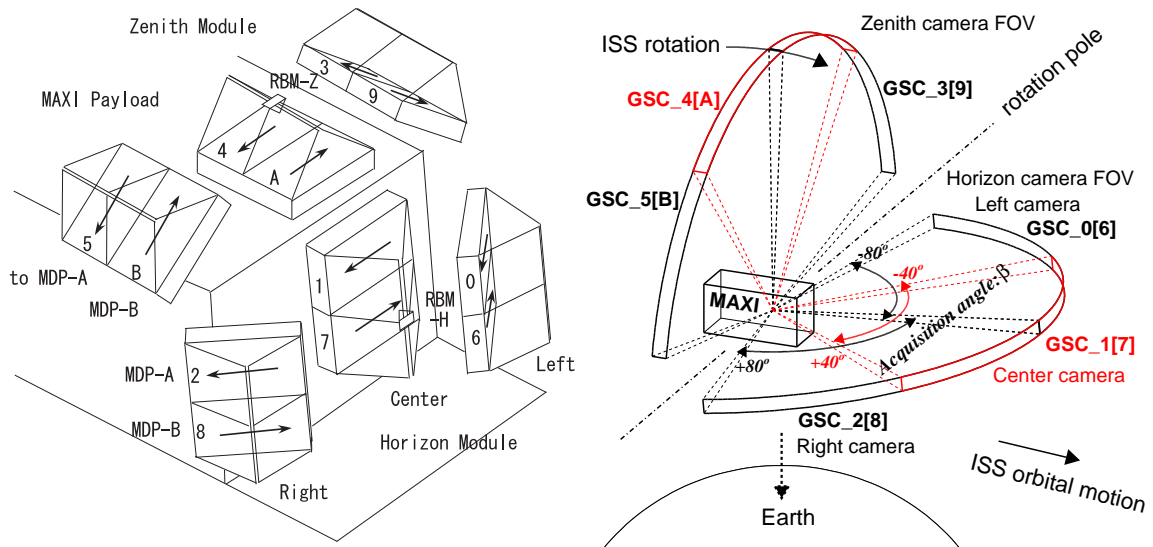


Figure 4.3: Configuration and fields of view (FoV) of GSC. Left panel: GSCs on Zenith and Horizontal directions. GSCs are installed to each direction respectively. Right panel: Thin-long FoV of GSCs. The FoV for central GSC is overlapped to FoV for other GSCs on both sides.

Slit-Slat Collimator

MAXI/GSCs employ the slit-slat collimators to determine the position of X-ray sources.

The top panel of figure 4.4 shows the construction of the collimators of GSCs. The top left panel of figure 4.4 shows the determination of the photon incident angle ϕ using the top slit and anode wire of proportional counters.

The top right panel shows the determination of the photon incident angle θ using the collimators. The field of view for the scan direction is obscured by the collimators and very narrow. Thus the source position for the scan direction is determined by transit time and attitude of the detectors. The typical transit time is about 40 s, and GSC scans the same position every 92 minute which is corresponding to the orbital period of ISS.

Detector Coordinate

The left panel of figure 4.4 shows the determination of the photon incident angle using the anode direction (the detector coordinate). An incident angle of the photon is detected by the line along the slit of the collimator and the position on the anode wires as a pinhole camera. The incident angle for detector coordinate is defined as ϕ .

When the incident angle ϕ is not perpendicular to the anode, X-ray photons through the slit of the collimator and the Be window on the proportional counter, and absorbed

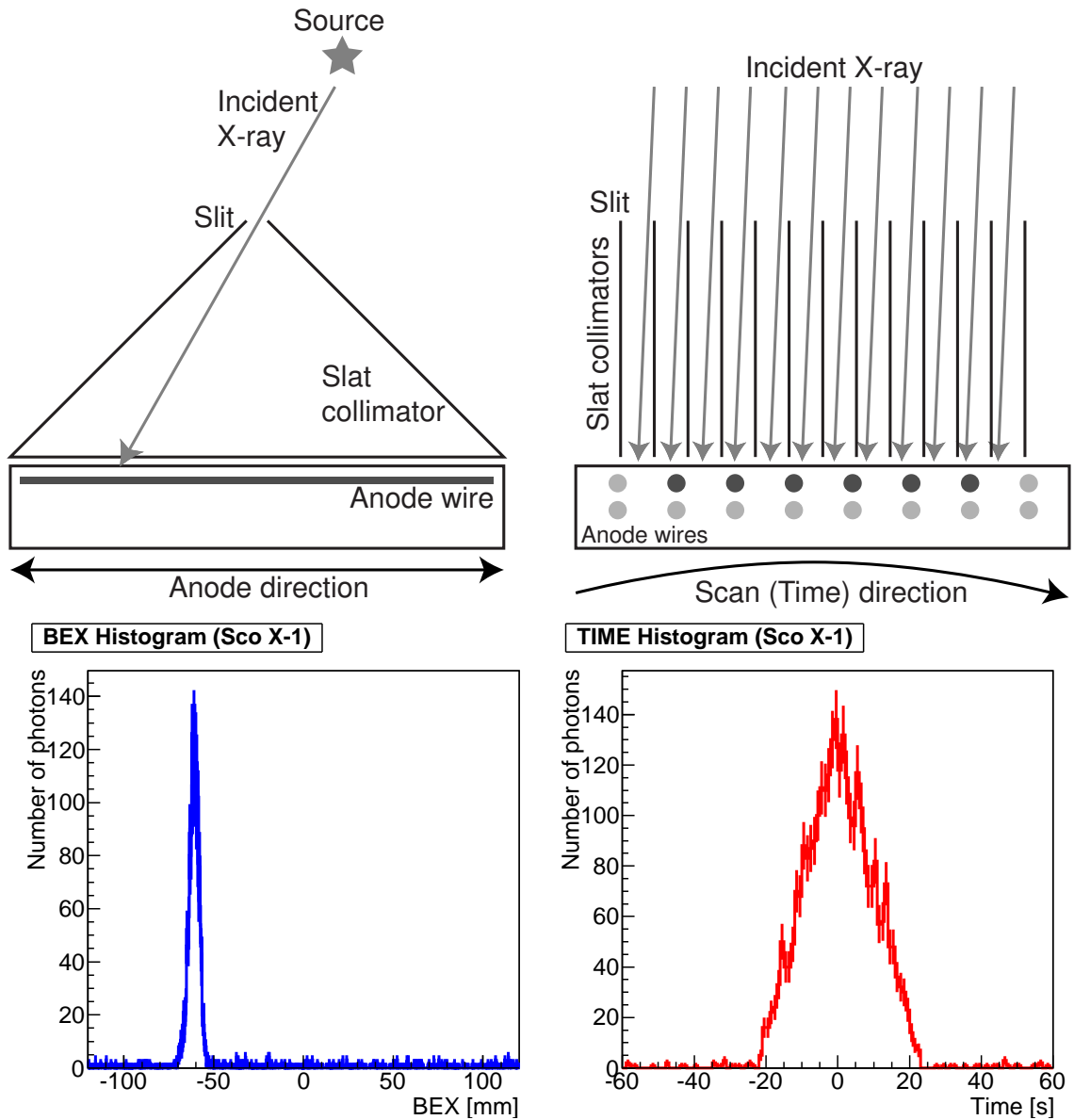


Figure 4.4: Principle of the position determination for the X-ray source on the sky coordinate. The top left panel shows the determination of the photon incident angle using the anode direction (the detector coordinate). The top right panel shows the determination of the photon incident angle using the collimators. Bottom figures show the event histograms on detector coordinate (left) and time series (right).

by the Xe gas in the proportional counter. The mean free path of X-ray photon μ in Xe gas varies by its energy. Thus, the photon detected (absorbed) position projected on the anode also vary by the energy and incident angle ϕ . In the case of a photon with high energy, the photon runs a longer path before getting absorbed by the Xe gas, making the

displacement from the incident position at the Be window to the actual absorbed position larger.

In order to determine the source direction, the detected position must be corrected to the incident point on the surface of the Be window. Since a probability process determines the path length for absorption, we can only correct the displacement statistically with an average value using the mean free path, which is a function of the measured photon energy and the gas pressure. The photon incidence position thus is determined by the position, which is referred to by a FITS keyword “BEX” (X coordinate at the Be window). We calibrated this correction process using the in-orbit data.

4.1.4 Xe Proportional Counter

In this subsection, we describe the detail of Xe proportional counter on MAXI/GSCs. Therefore, most of following descriptions are expositions about principle of X-ray detection and construction of GSCs.

The X-ray photon detector of GSC is a one-dimensional proportional counter. An incident photon deposits its energy to an electron by photoelectric effect. The photoelectron ionizes a nearby Xe and makes primary electrons whose number is proportional to the deposited energy. These primary electrons are accelerated towards the anode wire, and avalanche multiplication of electrons occurs along its path to the anode wire. The anode is made of the resistive carbon fiber and the charge of the multiplied electrons are read out at the both ends of the anode.

The incident position of a photon or particle is determined by the pulse height ratio read out at both anode ends. The sum of the pulse heights determined at the both anode ends is proportional to the energy deposited by the incident radiation. The position resolution improves with the amount of charges collected at the anode. For a given X-ray energy, a higher gas gain achieved with higher anode voltage gives better position resolution, as long as the electron avalanche is controlled in the gas counter. The energy resolution, however, becomes worse due to the space charge effect if the gas gain is too high. The nominal operating anode voltage of MAXI is chosen to be 1650 V, which provides reasonable compromise of the position and energy resolutions based on pre-flight calibrations. The operating voltage was lowered to 1550 V in some counters after we found out in orbit that GSC counters can be damaged by high charged particle fluxes.

The left panel of figure 4.2 shows the picture of a GSC proportional counter. The GSC proportional counters employ resistive carbon fibers with a diameter of 10 μm for anode wires. The higher resistive carbon fiber for anode is preferable for the better position

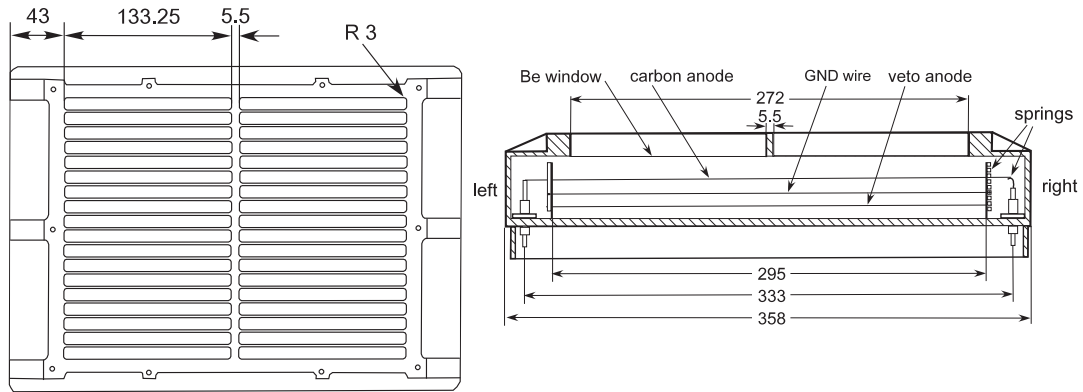


Figure 4.5: Construction of a GSC proportional counter. The left panel shows the top view of the GSC proportional counter. The Be window are protected from the pressure by the grid structures. The right panel shows the side view of the GSC. The background rate near the edge of the anode wire increase easily because the edge of the anode wire is not protected by anti coincidence anode wires as shown in the right figure.

resolution because the thermal noise on the read out signal is inversely proportional to the anode resistance. However the traditional carbon-coated quarts is mechanically weak, and easy to break by launch vibration. The vibration endurance carbon fiber anodes used in the GSC were developed at RIKEN and were successfully used in-orbit in the HETE/WXM (Shirasaki et al. 2003[49])

The front X-ray window is sealed with a 100 μm thick Be foil. This Be window has a total area of $192 \times 272 \text{ mm}^2$, The chamber is filled with Xe gas with a pressure. In order to protect the Be window from the integrated pressure of 740 kgW over the whole window surface, the Be window is covered by a 10.6 mm pitch grid structures along the each anode. The grid perpendicular to the anode wire is placed only at the center of anodes to keep the open area as large as possible (The left panel of figure 4.5). The expected maximum pressure of Xe gas is 1.66 atm at the temperature of 50°C . Each flight counters were designed and tested to endure the maximum pressure of 2.5 atm, which is 1.5 times higher than expected pressure.

The background due to the charged particle is rejected by the anti-coincidence anode wires which are placed at the bottom and both side of the main carbon-anodes. However, at the both edge of the anode wire, the background rate increases easily because the edge of the anode wire is not protected by anti-coincidence anode wires (The right panel of figure 4.5).

4.1.5 In-Orbit Performance

In this section, we will explain the in-orbit performance of MAXI/GSC.

Alignment Calibration

After the launch and obtaining the data from MAXI/GSCs, it was found that the full width at half maximum (FWHM) of point spread function (PSF) for X-ray sources was larger ($\sim 3.0^\circ$) than the expected value ($\sim 1.0^\circ$).

In order to resolve this problem, the calibration of the source localization of each camera with respect to the MAXI attitude system coordinate was carried out using the in-flight data of selected bright X-ray sources (Sco X-1, the Crab Nebula, GRS1915+105 etc.). The calibration involved the mechanical alignments of the cameras as well as the one-dimensional position encoding of every individual anode of the GSC cameras. As the result of this calibration, the FWHM of the PSF improved $\sim 1.0^\circ$ (which is consistent with expected value), and the accuracy of the source position was much improved ($\sim 0.2^\circ$). In addition, this accuracy was sufficiently small that the error circle can be contained in the field of view of Swift XRT. Thus, when the MAXI/GSC discover a new transient, a follow-up observation by Swift XRT can be conducted easily after this calibration. Examples of successful follow-up observations are GRB110213B (GCN11716[50] and GCN11720[51]), and XRF111111A (GCN12554[52] and GCN12555[53]). The detail of this alignment calibration is described in Morii et al. 2011[54]. We note, however, that this alignment calibration have been carried out for only 4.0–10.0 keV energy band, and more calibration work is needed for other energy bands.

PSF Width Calibration

The PSF of GSC counter is somewhat different for GSCs, and is not uniform along the anode position. As written in the previous section 4.1.3, the position of absorption on the detector coordinate is corrected using the energy-dependent mean free path of incident photons. Thus the width of PSF is broadened due to the photons with large incident angles, for which uncertainties in the projected detector position are large.

In order to determine the flux of X-ray sources by fitting the scan light curve, good knowledge of the PSF as a function of the detector position is required for dim sources, while it could be determined by the fitting of the real data for bright sources. Thus, we calibrated the PSF for every anode of every camera, using the real scan data of bright X-ray sources. We note that this calibration have been carried out only for the 4.0–10.0 keV energy band which we use in this work.

High Voltage Operation

GSC operation with twelve counter units GSC_0, GSC_1, ..., GSC_9, GSC_A, GSC_B are started on 2009 August 15 with a nominal high voltage (HV) of 1650 V for all twelve counters. Their power were turned off (which means that high voltage set to 0 V) when the ISS passes through heavy particle background area defined by an on-board radiation zone map obtained by Radiation Belt Monitor (RBM). In the beginning of the mission, we set the radiation zone map only at the SAA.

On September 8, 2009, the power of the analog electronics on the GSC_6 suddenly was shut down by the built-in safety mechanism. It was followed by the power down of another counter, GSC_9 on September 14, 2009. The data around the time of the power-down indicated that a carbon-anode wire in each of these counters was broken. It was also suggested that a large amount of discharges occurred repeatedly at the break location on the carbon wire. After then the GSC operation principle was changed so that any risks to cause potential damages should be avoid as much as possible. The high-voltage reduction at the high latitude above 40° was employed since September 23, 2009. Two noisy counters, GSC_A and GSC_B, which are supposedly weak and likely to be broken sooner, were also suspended from operation on September 26, 2009. On March 26, 2010, there was another power stoppage on the GSC_3 counter, which was also considered to be due to a carbon-wire fracture caused by high voltage breakdown. After then, the operation voltage was reduced to 1550 V for the counters, which had any discharge experience. Table 4.2 shows the summary of the GSC operations.

GSC All-sky Image

Figure 4.6 shows the all-sky image observed by MAXI/GSC integrated for the initial two years. The red, green, and blue color scales represent the intensity in 2.0–4.0, 4.0–8.0, and 8.0–20.0 keV energy range, respectively. The diameter of point source images roughly represents the relative brightness according to the Point Spread Function. We can easily see more than a hundred of X-ray sources over the whole sky as well as unresolved galactic ridge emission along the galactic plane with a scale of $1\text{--}2^\circ$.

4.2 Solid-State Camera

The Solid-State Camera (SSC) consists of two counter units, and monitors the entire sky in a lower energy X-ray band (0.5–12.0 keV). The field of view of the SSC is $1.5^\circ \times 90.0^\circ$. SSC detects X-ray photons through the thin slit, similarly to GSC. The plane of a unit

of SSC is composed by the 2×8 of CCD, and its total area is 200 cm^2 . Since the CCD cameras has the sensitivity in the optical and infrared bands, the surface of the CCD cameras is coated by the $0.2 \mu\text{m}$ aluminum. Besides in order to prevent the reflection of the optical lights, the body of SSC is constructed by black inorganic anodized aluminum alloy. Even with such countermeasures, SSC suffers infrared light leaks from the sides of the CCD chips in daytime. Thus the SSC can obtain useful scientific data only during orbit nights ($\sim 40\%$ of the total time), and covers 71% of entire sky in a single orbit.

The SSC can also search for transients as the GSC, in the lower energy X-ray band though it requires further calibrations.

Table 4.2: Summary of the HV operation of GSC counter

Date	GSC_0	GSC_1	GSC_2	GSC_3	GSC_4	GSC_5	lat $> 40^\circ $
2009-08-15	1650 V	1650 V	1650 V	1650 V	1650 V	1650 V	on
2009-09-08	1650 V	1650 V	1650 V	1650 V	1650 V	1650 V	on
2009-09-14	1650 V	1650 V	1650 V	1650 V	1650 V	1650 V	on
2009-09-23	1650 V	1650 V	1650 V	1650 V	1650 V	1650 V	off
2009-09-26	1650 V	1650 V	1650 V	1650 V	1650 V	1650 V	off
2010-03-26	1650 V	1650 V	1650 V	1550 V ^a	1650 V	1650 V	off
2010-04-10	1550 V	1650 V	1650 V	1550 V ^a	1650 V	1650 V	off
2010-11-13	1550 V	1550 V	1650 V	1550 V ^a	1650 V	1650 V	off

Date	GSC_6	GSC_7	GSC_8	GSC_9	GSC_A	GSC_B	lat $> 40^\circ $
2009-08-15	1650 V	on					
2009-09-08	off	1650 V	on				
2009-09-14	off	1650 V	1650 V	off	1650 V	1650 V	on
2009-09-23	off	1650 V	1650 V	off	1650 V	1650 V	off
2009-09-26	off	1650 V	1650 V	off	off	off	off
2010-03-26	off	1650 V	1650 V	off	off	off	off
2010-04-10	off	1550 V	1550 V	off	off	off	off
2010-11-13	off	1550 V	1550 V	off	off	off	off

^a Three anode wires of GSC_3 are broken by the high voltage breakdown. GSC_3 operates with remaining three anode wires after March 26, 2010.

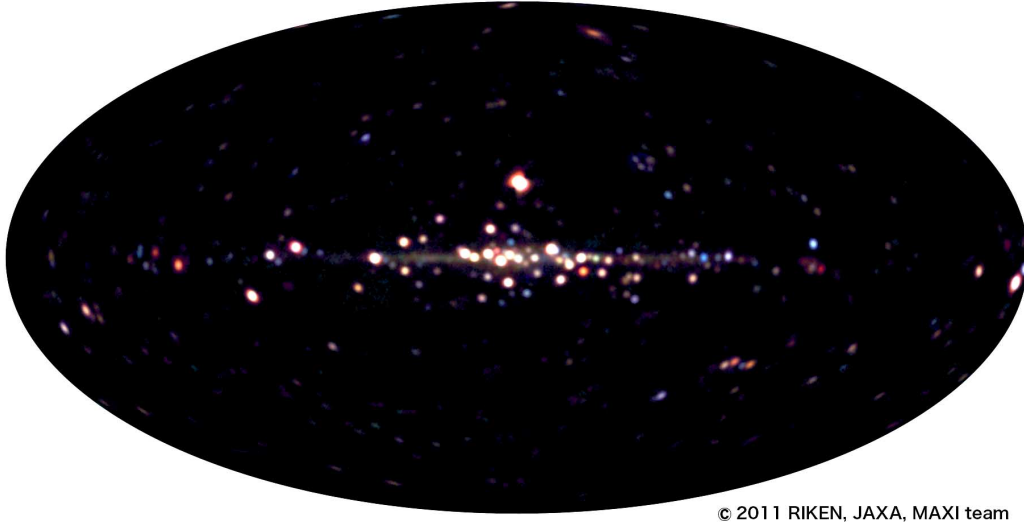


Figure 4.6: All-sky X-ray image observed by MAXI GSC with galactic coordinate.

4.3 Radiation Belt Monitor

Radiation Belt Monitors (RBMs) are attached on the middle of the center units of both horizontal and zenith GSC counter units to measure the charged particle flux which causes background. The RBM count rate is used for the autonomous safety mechanism for GSC that turns off the GSC high voltages when the particle flux is excessively high, thus to protect instruments from high flux charged particles. RBM employs a silicon PIN diode ($5.0 \times 5.0 \text{ mm}^2$, $200 \mu\text{m}$ depth, manufactured by Hamamatsu Photonics Co.). The aluminum with $50 \mu\text{m}$ thickness is deposited on the surface of the PIN diode. The particle transmission of the aluminum with this thickness is roughly equivalent to that of the Be window of GSC. The opening angle of the PIN diode is configured to about 80° which is also adjusted to the field of view of GSC. RBM has four settings of lower level discriminator that can cut the event rate with threshold energies of 30, 50, 200, and 1000 keV respectively. The lower threshold level of 30, 50 keV are used mainly to detect electrons with energies $< 200 \text{ keV}$ and some protons with energies $< 2 \text{ MeV}$. Since the thickness of the sensitive region of the PIN diode is only $50 \mu\text{m}$, electrons cannot deposit energies higher than 200 keV within this path length. Thus only protons with energies higher than 30 MeV and 100 MeV are detected with the threshold level of 200 keV and 1 MeV respectively.

The geographical distribution of the particle flux is shown by the RBM count rates in figure 4.7. The count rate of the particle clearly increases around the SAA and at high

geomagnetic latitudes in orbit near the north and south poles. Furthermore, figure 4.7 also shows that the particle flux in the horizontal RBM is significantly higher at high geomagnetic latitudes. This results suggests that charged particles are trapped by the geomagnetic field so that they have velocities preferentially in the plane perpendicular to the geomagnetic field lines. These properties can explain the difference of the particle maps obtained with the horizontal and zenith RBMs. We used the RBM data to select the good time intervals of the GSC data that do not suffer large non-X-ray background (NXB) rate.

In this thesis we use data after 2009 October 1 that do not contain the data with high NXB rates.

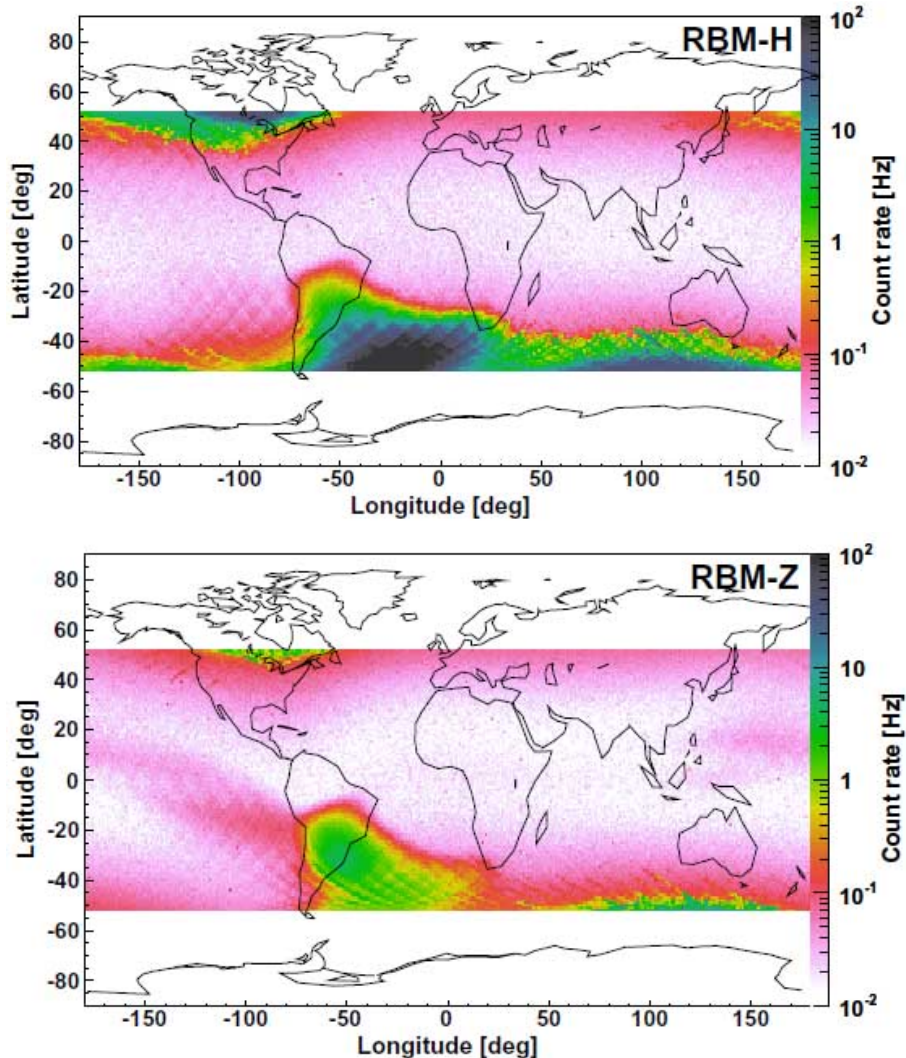


Figure 4.7: Particle map observed by MAXI/RBM. The upper and lower panel shows the count rate of the charged particle.

Chapter 5

Analysis & Results

For this study, we have developed a new procedure to detect fast X-ray transients from the archived MAXI/GSC data. This procedure is independent from the real-time nova search system.

In the real-time nova search system, the MAXI/GSC data are inspected as soon as they are downlinked to the ground. The MAXI team has reported new source activities to the public through its own mailing list, the Astronomers Telegrams (ATel), and GRB Coordinates Network (GCN). However, the detection thresholds of the real time nova search system are configured to high significance levels to prevent false alarms. In reality, the MAXI/GSC data should contain larger number of real transient events that were not picked up by the nova search system.

In this chapter, we describe the analysis method to search for short transients with durations less than 1 orbit of the ISS (92 minutes) in the MAXI/GSC data. These transients should include gamma-ray bursts (GRBs), X-ray flashes (XRFs), GRB afterglows, flare stars, and possibly other rare phenomena.

5.1 Short X-ray Transients Search in All-sky

5.1.1 Data Selection for GSCs

We search for X-ray transients from cleaned data of GSC obtained in the term from 2009 October 1 to 2010 December 31. In the early phase of the MAXI operation before 2009 September 26, some GSCs (GSC_6, GSC_9, GSC_A, GSC_B) were damaged with high voltage breakdown due to excessive irradiation in the high latitude above 40° . These GSCs were turned off after the trouble. Another one (GSC_3) was also damaged on March 26 2010, and was suspended from operation since then. Thus, in this study to search for

transients, we use the seven healthy GSCs (Zenith: GSC_4, GSC_5, Horizontal: GSC_0, GSC_1, GSC_2, GSC_7, and GSC_8) which operate constantly until 2010 December 31.

5.1.2 Data Reduction

At first, we made two-dimensional histogram in the TIME-BEX coordinate space. Here, TIME is the photon arrival time, and BEX (x coordinate at the Beryllium window) is the position of the photon projected back to the entrance window of the proportional counter

Table 5.1: Bright sources whose neighborhoods were excluded in the transient search. These sources are located at least 6.0° away from the galactic plane.

MAXI ID	RA	Dec	l	b	flux [mCrab]	Source
J1619–156	244.98	–15.64	359.09	23.78	12000	Sco X-1
J2144+383	326.17	38.32	87.33	–11.32	500	Cyg X-2
J1823–303	275.92	–30.36	2.79	–7.91	270	NGC 6624
J1731–169	262.93	–16.96	8.51	9.04	260	GX 9+9
J1738–444	264.74	–44.45	346.05	–6.99	170	H 1735–444
J1829–237	277.37	–23.80	9.27	–6.09	30	GS 1826–238
J0319+415	49.95	41.51	150.58	–13.26	30	Perseus Cluster
J1547–625	236.98	–62.57	321.76	–6.34	30	4U 1543–624
J1257–692	194.41	–69.29	303.48	–6.42	30	4U 1254–690
J1959+117	299.85	11.71	51.31	–9.33	30	4U 1957+115
J1712–233	258.11	–23.38	0.56	9.27	20	Ophiuchus Cluster
J0520–719	80.12	–71.96	283.09	–32.69	20	LMC X-2
J0538–640	84.73	–64.08	273.58	–32.08	20	LMC X-3
J1825–371	276.44	–37.11	356.85	–11.29	20	H 1822–371
J0539–697	84.91	–69.74	280.20	–31.51	20	LMC X-1
J0117–734	19.27	–73.44	300.41	–43.56	20	SMC X-1
J0355+310	58.85	31.05	163.08	–17.14	20	X Per
J1230+123	187.71	12.39	283.78	74.49	20	M 87
J1104+382	166.11	38.21	179.83	65.03	10	Mrk 421
J1657+353	254.46	35.34	58.15	37.52	10	Her X-1
J1918–052	289.70	–5.24	31.36	–8.46	10	4U 1916–053

assuming the energy dependent mean free path in the gas chamber. We determined a bin size of the histogram as the TIME bin width of 50 s and the BEX bin width of 5.0 mm. These bin sizes are chosen according to the point spread function (PSF) in a TIME-BEX space. The PSF are described in detail at section 5.2.2 in this chapter.

In order to exclude contamination of leaking photons from strong persistent sources, electronic transient noises, and non X-ray backgrounds, we created mask histograms for the following items.

1. Galactic plane ($|b| \leq 10.0^\circ$)
2. Neighborhood of bright sources (6° around Sco X-1, and 4° around other bright sources)
3. Time intervals close to the times when high voltages (HV) were turned on or off.
4. Regions near the counter ends where NXB dominates ($|BEX| \geq 120$ mm)

1. Exclusion of Galactic Plane

It is difficult to search for transients and identify them in the regions near the Galactic Center region and on the Galactic Plane with the high densities of X-ray sources while the PSF (position spread function) of the GSC counters is limited with only about 1.0° . A large fraction of the transients detected near the galactic plane probably originated from galactic sources. While this is also scientifically interesting, we focus more on the extragalactic short transients in this study. Therefore we exclude the galactic plane region with galactic latitude $|b|$ less than 10° in this transient search.

2. Exclusion of the Region around the Sources

Before starting the transient search, we need to exclude photons around the bright X-ray sources from the X-ray events in the observed data, in order to make the background model and focus our target only on transients. The list of excluded sources is shown in table 5.1. While we search transients in the region with galactic latitude $|b| > 10^\circ$, we need to exclude the bright sources as close as 6.0° away from the galactic plane in order to avoid their surroundings.

Since PSF for BEX direction has the Gaussian shape, the X-ray photons of a bright source may leak out to the neighboring bins, and they could be recognized as a transient event. For example, figure 5.1 shows the result of the transient search using 4.0° as the exclusion radius around Sco X-1. Numerous false events were detected in the immediate

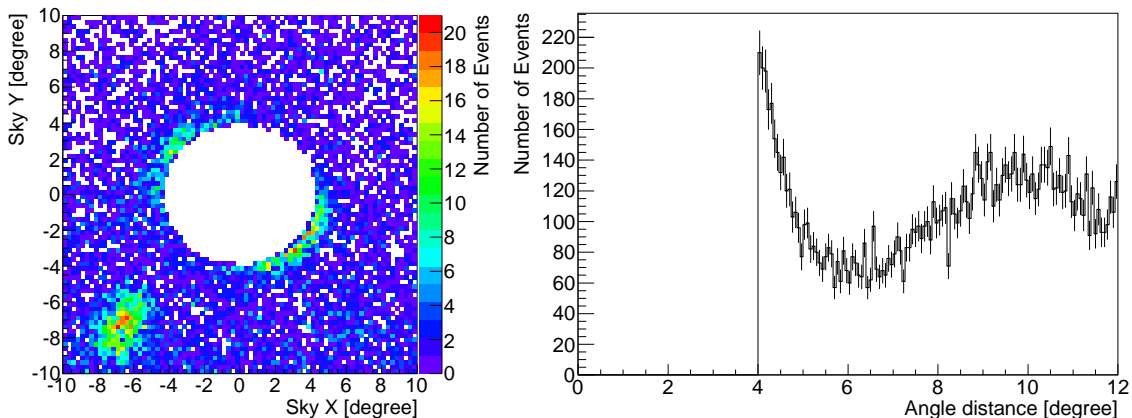


Figure 5.1: Left panel shows the example of the false detection of transients around Sco X-1. The region of Sco X-1 is excluded by the circle with the radius of 4.0° . False detections are found around the excluded region. Events on the bottom-left corner are the other source (MAXI J1659-152). Right panel shows the distribution of the angular distance from Sco X-1 (right panel). We confirmed that an exclusion radius of 6.0° is needed for Sco X-1 using this distribution.

vicinity of the exclusion region around Sco X-1. Based on the distribution of detected false transients as a function of angular distance from Sco X-1, as shown in the right panel of figure 5.1, we confirmed that an exclusion radius of 6.0° is needed for Sco X-1. With similar investigations, we confirmed that it is sufficient to set 4.0° exclusion radius for the other bright sources.

3. Exclusion of the Unqualified Time Series

Next, we describe the exclusion of non-astrophysical excesses in the time series. Throughout our transient search, we look for statistically significant excess counts in the time series data with a fixed time bin width of 50 seconds. However, observation is not continuous. The GSC is turned off in the SAA and high latitude regions. The beginning and the end of a time series may not have the equal effective accumulation time. In addition, the instrument may not be stable at the turn-on/off phases. In order to exclude such unqualified data, we masked the bins whose next bin has no counts (instruments turns off bin) in the light curve in which the TIME-BEX two-dimensional histogram is projected on the TIME coordinate.

4. Exclusion of the BEX Region with NXB Dominant

In order to exclude particle events and γ -rays, GSC has the anti-coincidence system using the veto anodes placed in parallel to the main anode wires. The regions near the both ends of the anodes, however, are not guarded by anti-coincidence anodes, and are exposed to non X-ray background (NXB). In fact we find the NXB increases towards the both ends of anodes, and the NXB is dominant in the regions with $|\text{BEX}| > 130$ mm. The NXB also exhibit time variation according to the particle density in the orbit. The NXB increase in the SAA and high latitude regions (radiation belt near the north and south pole). In order to find the BEX range in which the NXB does not seriously affect the sensitivity in our study, we made the histogram of background events projected on the BEX coordinate, and fitted this histogram by a function composed of the cosmic X-ray background (CXB) plus a constant value representing NXB. As a result, we found that the histogram within the BEX region with $|\text{BEX}| < 120$ mm can be well modeled by a constant NXB. Thus, for the present transient search, we adopted the BEX range of $|\text{BEX}| < 120$ mm in which we can assume the NXB as constant.

5.1.3 Effective Area for Sources

GSC detects a point source when an incident photon passes through the opening of collimators rotating with ISS orbital motion. Thus, the effective area for a point source is defined as the function of the transit time.

At first, we assume that MAXI was constantly rotating with respect to the celestial sphere, while the X-rays come from a source through the slit of the GSC. Using the transmission angle θ , which is defined as the incident angle of the photon projected on the detector plane perpendicular to both the slat collimators and the detector window, the effective area is described as formula 5.1. As the transmission angle θ is sufficiently small ($< 3^\circ$ within the slat collimator transmission), $\sin \theta$ can be approximated by θ , and then,

$$A_{\text{eff}} = \begin{cases} a - h \sin \theta & (a \geq h \sin \theta) \\ 0 & (a < h \sin \theta) \end{cases} \simeq \begin{cases} a - h \theta & (a \geq h \sin \theta) \\ 0 & (a < h \sin \theta) \end{cases} \quad (5.1)$$

If the scan direction is within this plane, the shape of the time variation of the effective area is approximately triangular as shown by this formula. Actually, the rotation of ISS is not constant. The shape of the effective area curve is modified according to the attitude variation of the ISS. Thus the accurate effective area is obtained not only by the event data of GSC but also with the attitude data of ISS. Figure 5.2 shows the example of the effective area for a point source.

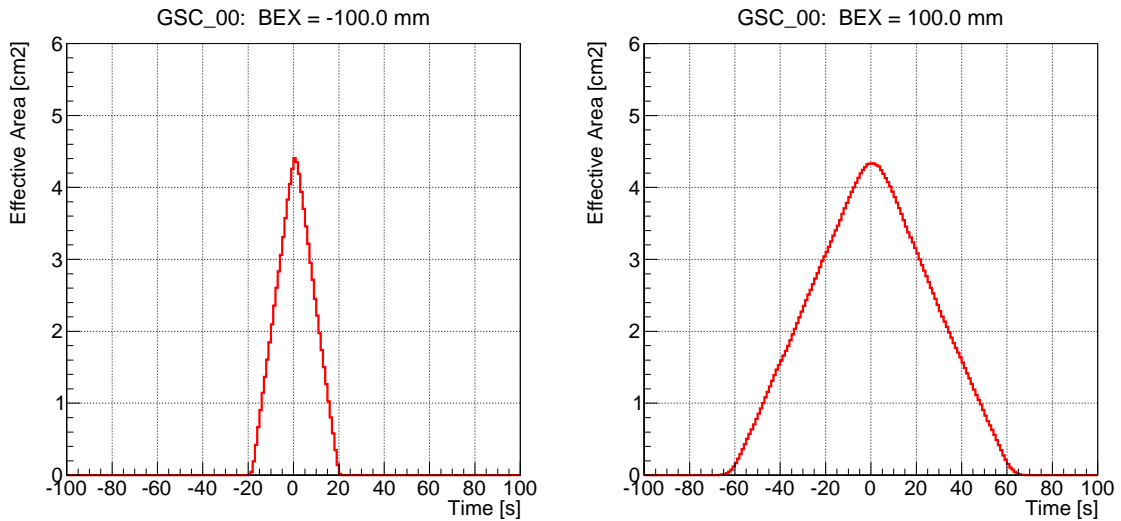


Figure 5.2: Example of the time dependence of effective area for a point source. The left panel shows the typical effective area for GSCs. The right figure shows the source effective area at the detector position monitoring sky near the orbital pole. The scan time of a source near the orbital pole is longer than that in other region.

5.1.4 Effective Area for Background Counts

In this section, we will consider the effective area for background counts in order to use the background model for transient search.

We assumed that the main source of the background counts in the 4–10 keV energy band is not the electrical noise, but the radiation from the outside of the detector composed of the cosmic X-ray background (CXB) and the non X-ray background (NXB). CXB is irradiated almost uniformly from the whole sky, and its main component is the emission from numerous unresolved point sources. NXB mainly consists of charged particles in the orbit and the γ -rays from the sky, the earth, or the ISS environment. Throughout this thesis, we assume that the rate of CXB is constant irrespective of the sky position and it does not vary with time.

The effective area for CXB and NXB need to be calculated with a method that is different from the method used for the point source. Since we assume that the CXB is distributed uniformly on the sky, the GSC field of view for the CXB does not vary with time, and therefore we can consider that the rate of detected CXB is constant with time. On the other hand, NXB rate increases in the SAA and at high latitudes, we have to consider its time variation.

Estimation of Cosmic X-ray Background

Since the count histograms prepared for the transient search do not include contribution of bright sources, these data can be regarded as the data dominated by background counts. We integrated these histograms and estimated the background rate as a function of the BEX coordinate. At first, we describe the estimation of the cosmic X-ray background (CXB).

As described in the previous section, we assumed that the CXB is uniformly distributed over the whole sky. We only need to consider that the effective area of GSC camera depends on the incident angle ϕ due to the following two factors. First, the cross section of the slit for the incident photons is proportional to $\cos\phi$. There is another reduction by a factor of $\cos\phi$ for the solid angle because the distance from the slit to the detector window is longer by the inverse of this factor. Thus, we can fit the CXB by the following function.

$$N_{cxb}(\phi) = C \times \cos^2\phi \quad (5.2)$$

where C is the normalization factor. The incidence angle ϕ is related to the coordinate x in the BEX direction and the distance of the slit from the detector window h as

$$x = -h \times \tan\phi \quad (5.3)$$

The model function is thus obtained by substituting equation 5.3 in formula 5.2.

$$N_{cxb}(x) = \frac{C}{1 + (x/h)^2} \quad (5.4)$$

Using this function 5.4, we made the background histogram using all background data from October 1, 2009 to December 31, 2010 for each GSC units. Figure 5.3 shows the event distribution on the BEX coordinate for GSC_0.

Estimation of Non X-ray Background

Non X-ray background (NXB) is also detected by GSCs, and it is mainly caused by the charged particles and γ -rays distributed in orbit.

Since the charged particles are trapped by the geomagnetic field, the rate of NXB varies with the places in orbit. On the detector coordinate, the rate of NXB increases at the both side of anodes which is not protected by the anti coincidence anodes, and varies with time. Since the rate of transients strongly depend on the background level, we need to exclude the data obtained around the SAA and at high latitude regions.

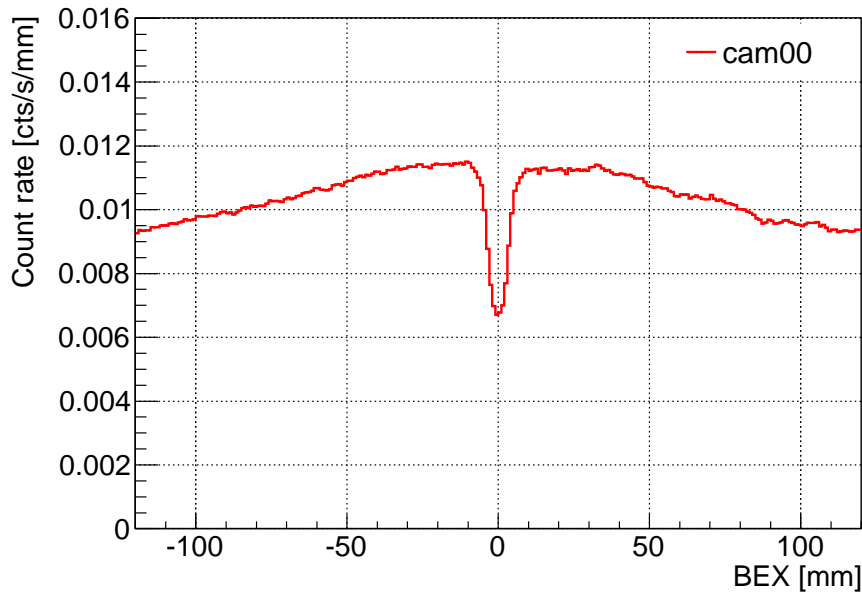


Figure 5.3: Integrated background plot for GSC_0 on the BEX coordinate. The data of this histogram is integrated from 2009 Oct. 1 to 2010 Dec. 31.

The other cause of the NXB is the γ -ray irradiation by the ^{137}Cs source mounted at the bottom of the Soyuz spacecraft. The NXB rate caused by this γ -ray source is higher than that caused by charged particles. Figure 5.4 shows the NXB rate during the period studied in this work (October 1, 2009 to December 31, 2010). The rate of NXB is strongly correlated with the presence of Soyuz on the ISS, and is significantly higher when it is present.

5.1.5 Extraction of Candidates for Transients

Data Extraction

In order to pick up transient sources, we must determine the background model first. Assuming that the CXB was constant, the normalization of CXB was fixed in the model fitting of the background count histogram. The only free parameter is the NXB normalization. We used the binned likelihood method for the fitting algorithm. We use the value of the background which is the sum of the obtained value of NXB normalization (N_{nxb}) and the value of CXB function ($N_{cxb}(x)$) (equation 5.5) for calculating the significance value.

$$N_{bg} = N_{nxb} + N_{cxb}(x) \quad (5.5)$$

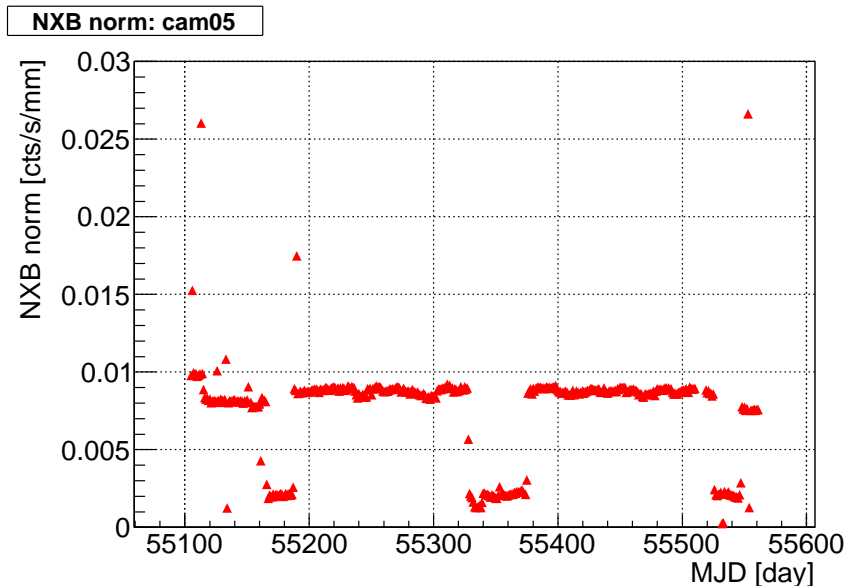


Figure 5.4: Long-term variability of NXB on GSC_5 during the period studied in this work (October 1, 2009 to December 31, 2010). The rate of NXB is correlated with the presence of a Soyuz spacecraft. Four data points with extremely high values corresponding to the times of solar flares.

The source count is given by subtracting the background N_b from the photon counts in a bin (N_{bin}) as equation 5.6.

$$N_s = N_{bin} - N_b \quad (5.6)$$

We define the significance of a transient as

$$\sigma = N_s / \sqrt{N_b}. \quad (5.7)$$

Based on the significance given by equation 5.7, we selected transient candidates with significance of 5σ or larger in the all-sky search. We note that a large fraction of the transient candidates thus extracted may be statistical fluctuations.

Binned Likelihood

Since the GSC data for a single scan contains only small number of photons, we use the binned likelihood method for fitting minimization instead of χ^2 method. The distribution of binned events follow the Poisson distribution. It can be generally approximated to Gauss function and χ^2 method may be used when more than 20 counts are contained in a bin, which is not the case here. The likelihood value $L(\alpha_1, \alpha_2, \dots, \alpha_m)$ is calculated by

the following equation 5.8.

$$L(\alpha_1, \alpha_2, \dots, \alpha_m) = \prod_{i=1}^N P_i \quad (5.8)$$

where $\alpha_1, \alpha_2, \dots, \alpha_m$ are the parameters of the model function to fit, m is the number of parameters, N is the number of bins, i is the bin sequence number, and P_i is a probability density function of the distribution (Poisson distribution in this case).

Most likely model parameters are obtained by maximizing $L(\alpha_1, \alpha_2, \dots, \alpha_m)$, or minimizing $-\text{Log } L$. For the Gaussian distribution, $-\text{Log } L$ agrees with the χ^2 value, and the χ^2 minimization is equivalent to the binned likelihood maximization.

5.1.6 GSC Exposure Map

MAXI/GSC surveys the whole sky, but its exposure of the sky is not uniform. For example, the sky region near the rotation axis of the ISS has higher exposure than the orbital equator in a orbit. The frequency of transients in a high exposure region is clearly larger than in regions with lower exposures. Thus, correction of the exposure is needed for the calculation of the frequency and the angular distribution of transients.

Figure 5.5 shows the exposure map for MAXI/GSCs with galactic coordinate plotted by HEALPix grid[55]. HEALPix is an acronym for Hierarchical Equal Area isoLatitude Pixelization of a sphere. Each HEALPix pixel covers the same surface area as every other pixel. The area size of a pixel in figure 5.5 is 3.36 square degree. The region with higher exposures is located around the north and south poles of the sky. The region with lower exposure is formed as concentric rings due to the vertical grid of the GSC counters (see Figure 4.5, which blocks the exposure to the sky. The maximum exposure is about four times of the minimum value. The exposure for a pixel is 2.5–10 days in this study.

5.1.7 Transient Frequency Map

In order to examine the distribution of the candidate of X-ray transient, we plotted the detected transient data with significance above 3σ on the galactic coordinate.

Figure 5.6 shows the frequency of the candidates obtained by the MAXI/GSC data in 4.0-10.0 keV energy range. We call this map “Frequency map”. This map shows the frequency of the candidates on the galactic coordinate. This frequency map is normalized by the exposure with the correction factor of 1.0 corresponding to the maximum exposure. Thus the value on the frequency map indicates the detection frequency per pixel in the observation term (15 month). We can see the areas of the sky where transients occur

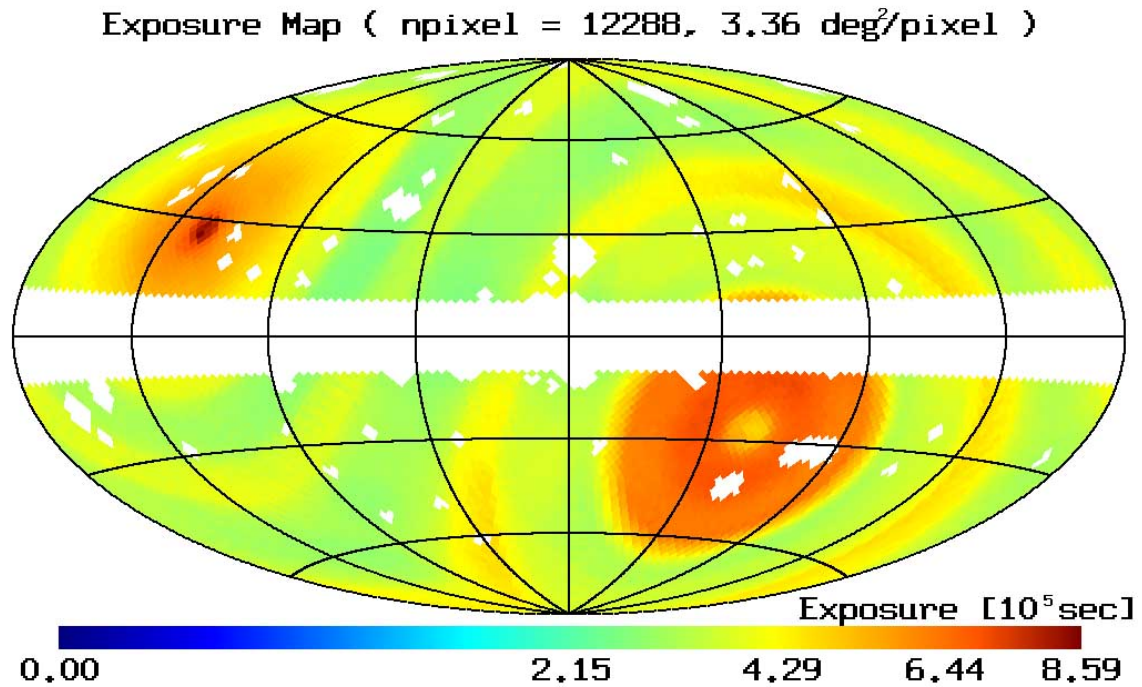


Figure 5.5: Exposure map observed by MAXI/GSC with galactic coordinate plotted by HEALPix grid[55]. The region with higher exposure is located around the North and South Pole of Earth.

frequently. We note that this map includes both the real transients and the statistical fluctuations of the background.

5.2 Local Analysis for Candidates of Transient

In the previous section, we defined a large bin size to search for candidates of X-ray transients from the entire sky. In order to study statistical properties of these transients and identify their sources, more detailed analysis in narrow regions (“local analysis”) is needed. In this section, we describe the local analysis conducted for candidates of X-ray transients detected with $> 5\sigma$ significance by all-sky search. We carried out the local analysis by the following procedure.

1. Position determination by making the PSF-smoothed image
2. Flux calculation using PSF fitting
3. Exclusion of false events
4. Probability calculation

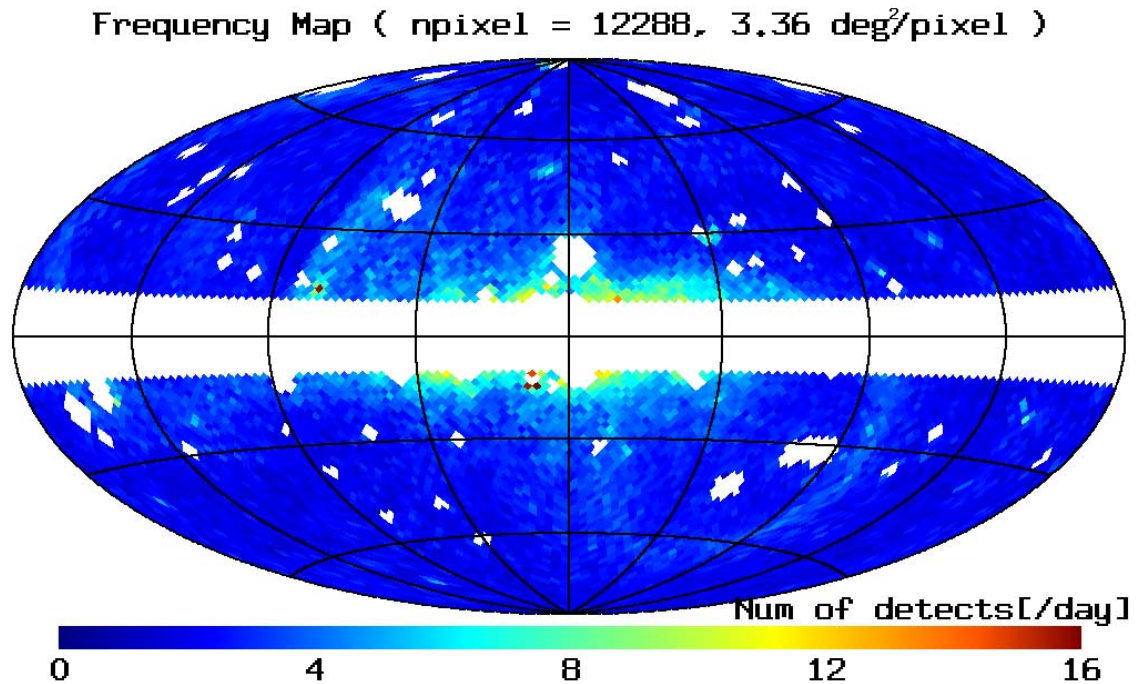


Figure 5.6: Candidates frequency map observed by MAXI/GSC on the galactic coordinate with HEALPix grid. This map includes both real transients and fluctuations of the background.

5.2.1 Data Reduction

We extracted circular regions from single scans with the radius of 5.0° from the center of (RA, Dec) of transient candidates detected in the all-sky search. Note that we excluded the region near the galactic plane ($b \leq 10^\circ$), and regions around known sources in choosing the transient candidates.

5.2.2 Localization of the detected X-ray source

At first, we determined the position the transient by making images smoothed with the point-spread function (“PSF-smoothed images”) as follows before finding the flux by the fitting procedure.

PSF-smoothed Image

The PSF-smoothed images are produced in the TIME-BEX plane. We used Gaussian functions as the PSF in the BEX coordinate $f(x)$, and triangular-shaped PSF $g(t)$ in the TIME coordinate. The smoothed image element n_i is obtained by formula 5.9. Here, we

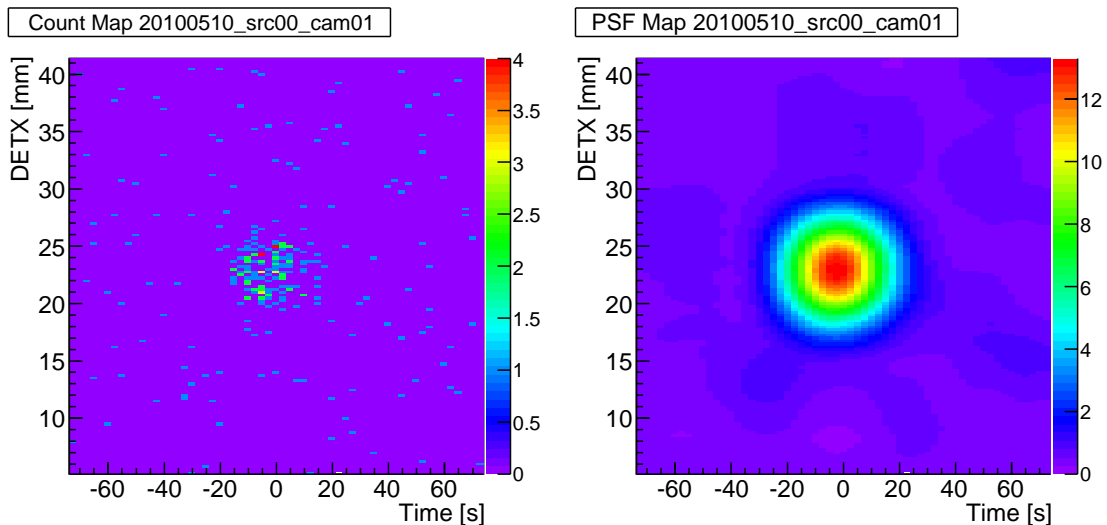


Figure 5.7: Examples for a PSF-smoothed image in the TIME-BEX plane. Left panel shows the count map for GRB100510, and right panel shows the image smoothed with PSF. The most accurate position is determined as the position with the maximum value in the smoothed image.

do not consider backgrounds.

$$n_i = \sum_j N_j \times f(x_j)g(t_j) \quad (|x_j| \leq 2.0\sigma_{x_j}, |t_j| \leq Tw_{x_j}/2) \quad (5.9)$$

Figure 5.7 shows an example of the original count map compared with the PSF-smoothed image. The left panel of figure 5.7 shows the original count map obtained with MAXI/GSC. The right panel of figure 5.7 shows the example of the image smoothed with the PSF. We determined the position of source as the position with maximum value of n_i . The accuracy of this position determination method is about 0.2° for the Crab Nebula.

5.2.3 Flux Calculation

In order to calculate the flux of transients, we fitted the data with the PSF in the TIME-BEX plane.

We find that if we fit the count map with coordinates as free parameters, the parameters does not converge well, probably due to small number of photons from the transient. We therefore performed the fitting with the fixed transient position found in the procedure above.

In addition, we assume the X-ray flux is constant over the scan transit time over a source, which is 40-120 seconds (average 50 seconds).

The unbinned likelihood method is used in the PSF fitting for GSC to obtain the best-fit parameter values for the source flux and the background rate. This method is required because the number of photons can be very small (~ 10 photons for 100 mCrab in a scan), but it makes difficult to define the goodness of fit as the χ^2 method.

5.2.4 Exclusion of False Events

In addition to statistical fluctuations of background counts, MAXI/GSC picks up false events caused by solar flares, charged particle flux variation, and electronics noises. Following is the list of the sources of false events of the GSC. We describe how to exclude them in the following.

1. Solar flare events scattered on the collimators.
2. Solar flare events leaking to the next GSC camera.
3. Solar flare events reflected on the solar paddle.
4. Charged particle events
5. HV on-off events
6. Discharge events

Solar Flare Events Scattered on the Collimators

The first of the three types of false events caused by solar flares are the collimator reflection events.

In order to avoid the solar X-ray emission, the power of GSC is turned off within 5.0° around the sun. When an intense solar flare occurs, however, the solar X-ray flux scattered on the surface of the slat collimators may be strong enough to be detected by the GSC even if the sun is more than 5.0° away from the GSC field of view. We excluded these events according to the position of the sun at the time of the transient occurrence. If the distance between transients and the sun is less than 10.0° , we exclude this candidate.

Sun Leak events

The X-ray photons of very intense solar flares from a GSC slit can reach the very edge of the next camera and sometimes detected by the particular anode of some GSC cameras due to mechanical allowances. We call these events “Sun leak event” These leak events

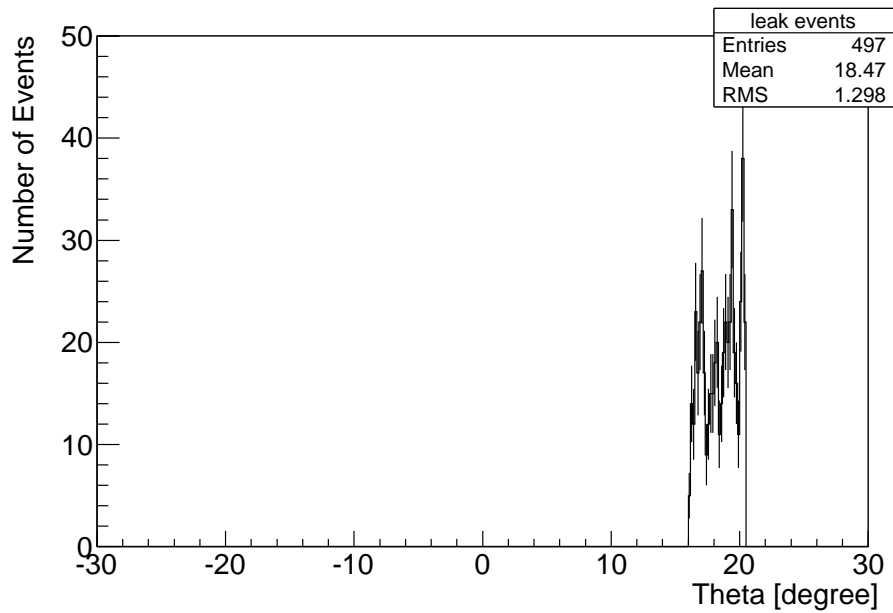


Figure 5.8: The Sun angle θ distribution for the leak events extracted by the the condition 5.10. Leak events are concentrate to the region $[16^\circ < \theta < 22^\circ]$.

are detected only by the anode 5 which is closest to the next camera, and most of these events are found in the GSC_5 camera. The small fraction of them are also found to occur in the GSC_3, GSC_8 cameras.

The shape of the leak event is very similar to short X-ray transient and could not be excluded by PSF fitting. We can exclude these leak events as follows. Since these leak events are detected only in anode 5, we find

$$\sum_{j=0}^4 N_{Cj} < N_{C5} \quad (5.10)$$

Where N_{cj} is a total count detected on anode j .

We also find these leak events occur when the sun is located at a particular direction with respect to the GSC field of view. The distribution of the θ , which is the scanning angle of the Sun form the detector coordinate, is shown in Figure 5.8 for the bright leak events. We find that these leak events are concentrated in the region between 16.0° and 22.0° . When the number of photon too small to evaluate the condition 5.10, we excluded the leak events based on the the θ distribution. We calculated the value of θ for all transient data, and excluded the events between 15.0° and 23.0° after the position determination.

Solar Flare Events Reflected on the Solar Paddle

The solar flare X-rays may be reflected on the solar paddle of the ISS and detected by the MAXI GSCs. This is another cause for false events.

A solar paddle event does not have photon distribution of a point sources. Thus, most of solar paddle events are not detected by all-sky search in this study. In addition, even if such a event is picked up, a large background and small source flux will be found in the PSF fitting, and can be excluded. These results are confirmed in our analysis for 15 months data.

Summarizing above contents, we can exclude the solar false events based on the following conditions of their position with respect to the sun

1. within 10.0° from the sun
2. $15.0^\circ < \theta < 23.0^\circ$

Charged Particle Events

Time variation of charged particles is another cause of false events, In SAA and high latitude regions, the count rate of background in the MAXI GSC data increases due to charged particles. These particle events are spatially extended on the TIME-BEX plot unlike point sources, and therefore can be rejected by the PSF fitting.

HV on-off Events

The other cause of false event originates in electronics of the detectors. During the period soon after the the high voltage of the GSC (HV) is turned on, the gain of the detector is not stable, and the background rate changes transiently, resulting in temporary increase of the count rate. However, these background counts are uniformly distributed on the BEX coordinate unlike point sources, and can be excluded by the PSF fitting.

Discharge Events

Another kind of false events cause by electrical noise are discharge events. Because the HV discharges in the detectors have serious effects on the GSC operation, these events are monitored continuously by MAXI team. Most of these events are detected near the ends of anode wires ($|\text{BEX}| > 130 \text{ mm}$) that are not included in the current search. In addition, these events do not have shape of point sources, and therefore can be excluded using the PSF fitting.

5.2.5 Calculation of False Detection Probability

Since GSCs do not observe the source continuously, the background level of GSC vary from one scan to another. Accordingly, the threshold level used to define the significance of transients varies too.

In order to define the significance of detection consistently, we performed a simulation. For each detected transient, we produced simulated data sets following the Poisson distribution with a mean value of background ($\mu = N_b$), and calculated the source count rate using the PSF fitting using the same algorithm used for the real data. By performing this fitting to a large number of simulated data, we estimated the probability of detecting false transients with source counts N_s due to the statistical fluctuations. With this, we can also evaluate the probabilities for detecting transients in more than one GSC cameras. The results of these estimates are shown in next section.

5.2.6 List of Detected Transients

At the first step of selecting transient candidates in the whole sky, we made the histograms on the detector coordinate with fixed time width of 50 seconds. The number of histogram bins for the 15 month data is 7.72×10^7 . We therefore set the threshold level for transient candidates to be occurrence probability of 10^{-8} , with which the expected number of false event due to statistical fluctuation is only one.

We found 22 transients with probability of less than 10^{-8} (9σ significance). The locations of these transients in the sky are plotted on figure 5.9. We listed these 22 detected transients in table 5.2. Some of these bright transients were identified by the real time nova search system. We summarized the comparison between our transient search and leak time search data in Appendix A.

In addition, we also searched for transients based on coincidence among two cameras. We set the threshold with the combined probability of less than 10^{-8} and also requires probabilities of less than 10^{-3} in both of the two cameras. We found 16 transients satisfy this coincidence criterion, with nine of them already included in the 22 transients picked up by the previous criterion, and seven additional transients newly found with this coincidence criterion. These seven transients are shown in table 5.3.

Table 5.2: Transients detected with probability of $< 10^{-8}$

Time	RA	Dec	l	b	Ang. Dist.	flux [cts s $^{-1}$ cm $^{-2}$]	prob.	ID
2009-10-12T10:25:56	183.06	63.12	130.35	53.44	112.69	136.1 \pm 16.9	< 1.00e-15	FXT091012 (GRB)
2009-10-29T10:31:49	216.43	65.82	108.59	48.60	102.17	97.5 \pm 22.8	1.65e-10	unID or SNe
2009-12-22T22:18:16	263.27	-13.84	11.38	10.41	15.37	308.6 \pm 44.3	< 1.00e-15	unID or NRAO530
2010-01-23T05:18:10	54.32	0.61	184.99	-41.46	138.30	108.7 \pm 86.3	4.82e-11	HR1099 (flare star)
2010-02-06T18:56:31	186.82	61.21	128.09	55.68	110.35	448.3 \pm 91.0	< 1.00e-15	unID
2010-02-07T00:04:16	117.40	-76.63	288.85	-23.08	72.71	79.6 \pm 19.2	1.80e-11	unID
2010-03-18T02:20:49	119.14	-76.80	289.18	-22.77	72.37	72.9 \pm 18.9	5.14e-10	unID
2010-03-27T17:08:19	346.29	43.01	103.07	-15.73	102.57	99.5 \pm 24.6	5.46e-12	FXT100327 (GRB)
2010-04-13T21:18:51	24.53	-18.05	175.20	-75.93	104.02	164.7 \pm 46.4	1.32e-09	unID or AGNs
2010-04-15T03:44:51	7.75	-16.30	98.26	-78.18	91.69	336.1 \pm 59.9	< 1.00e-15	GRB100415A
2010-04-22T03:11:20	288.85	-17.85	19.42	-13.19	23.33	130.0 \pm 31.6	1.47e-10	Swift J1922.7-1716
2010-04-25T05:17:51	256.71	24.02	45.23	32.95	53.77	74.6 \pm 46.2	9.85e-13	4U1700+24
2010-05-10T19:27:22	355.81	-35.73	358.07	-73.14	73.15	717.4 \pm 51.0	< 1.00e-15	GRB100510A
2010-06-16T01:42:17	52.33	-41.54	247.41	-54.75	102.81	113.5 \pm 28.4	6.05e-12	XRF100616A
2010-06-27T09:57:49	271.81	19.72	46.21	18.33	48.94	104.5 \pm 20.8	6.50e-10	unID
2010-07-01T06:54:29	188.81	-34.22	299.12	28.53	64.69	281.1 \pm 47.0	< 1.00e-15	XRF100701A
2010-08-23T17:25:46	20.45	6.11	136.50	-55.96	113.96	646.5 \pm 55.7	< 1.00e-15	GRB100823A
2010-09-07T18:25:30	160.88	-33.31	274.34	22.36	85.99	91.6 \pm 60.6	1.95e-10	TWA-7 (flare star)
2010-09-15T20:22:48	182.28	85.00	124.01	32.04	118.31	106.4 \pm 30.7	1.35e-11	unID
2010-10-10T04:49:19	64.29	32.99	165.14	-12.54	160.65	127.2 \pm 23.6	< 1.00e-15	unID
2010-12-11T11:45:54	162.44	41.20	175.62	61.38	118.53	152.0 \pm 49.5	7.17e-09	unID
2010-12-14T15:17:36	323.30	-4.45	49.51	-37.66	59.06	199.2 \pm 49.5	5.09e-11	unID

Table 5.3: Transients table detected by multiple cameras with 9σ significance.

Time	RA	Dec	l	b	Ang. Dist.	flux [cts s ⁻¹ cm ⁻²]	prob.	ID
2009-11-18T17:28:34	332.65	-55.08	337.80	-49.73	53.24	32.42 ± 4.90	3.88e-10	unID
2010-04-05T03:58:39	359.30	28.29	108.67	-33.08	105.56	76.08 ± 9.01	1.38e-08 ^a	II Peg (flare star)
2010-07-04T16:38:32	312.54	-25.66	19.86	-36.49	40.87	57.12 ± 3.08	1.58e-14	unID
2010-07-07T00:51:41	357.81	-7.82	83.71	-66.00	87.45	124.12 ± 8.53	< 1.00e-15	GRB100707A
2010-09-11T14:58:21	103.98	-70.60	281.42	-25.11	79.67	103.71 ± 8.09	1.18e-13	FXT100911 (GRB)
2010-11-10T09:26:44	176.13	-33.83	287.36	27.01	74.58	106.51 ± 11.25	2.03e-10	unID or SNe
2010-12-10T03:38:29	61.62	-5.05	196.49	-38.65	138.49	80.21 ± 6.75	8.24e-09	unID

^a The probability of this transient is slightly higher than 10^{-8} , but because the counterpart (II Peg) of this transient were found, we included this transient in our list.

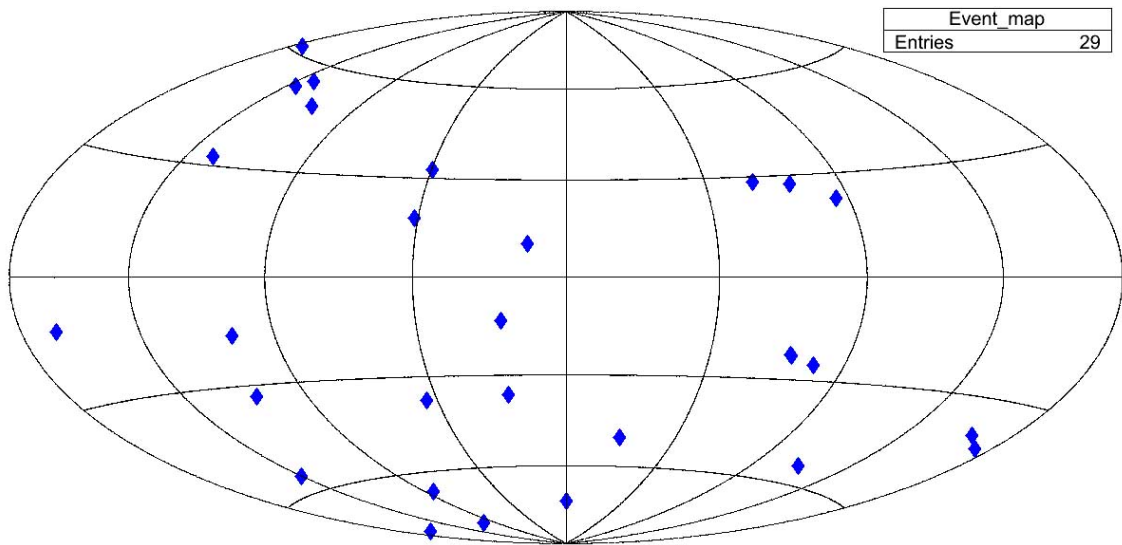


Figure 5.9: Distribution of transients detected by MAXI GSC on the galactic coordinate. The probability of these plotted transients are less than 10^{-8} which is corresponding to about 9σ significance.

5.2.7 Spatial Distribution of Detected Transients

Figure 5.9 shows the spatial distribution of detected transients in our transient search with probability of less than 10^{-8} , which corresponds to about 9σ significance. We searched for these transients in the region excluding the galactic plane ($|b| < 10^\circ$) and vicinity of bright sources (radius of 4° from the source center). We find that these transients are distributed roughly uniformly. In addition, we note that there seem to be more transients in the regions with high exposure than in other regions.

5.2.8 Identification of Transients

In this section, we try to identify MAXI transients by comparing them to various source catalogs.

Prompt Gamma-ray Bursts

The first source class to be checked for short X-ray transients is the gamma-ray burst. We checked the trigger time and the spatial position of our transients data against the gamma-ray burst catalogs of Swift BAT, Fermi GBM, INTEGRAL IBIS, Suzaku WAM, and Konus-Wind.

We found two counterparts of prompt GRBs and one counterpart of GRB afterglow.

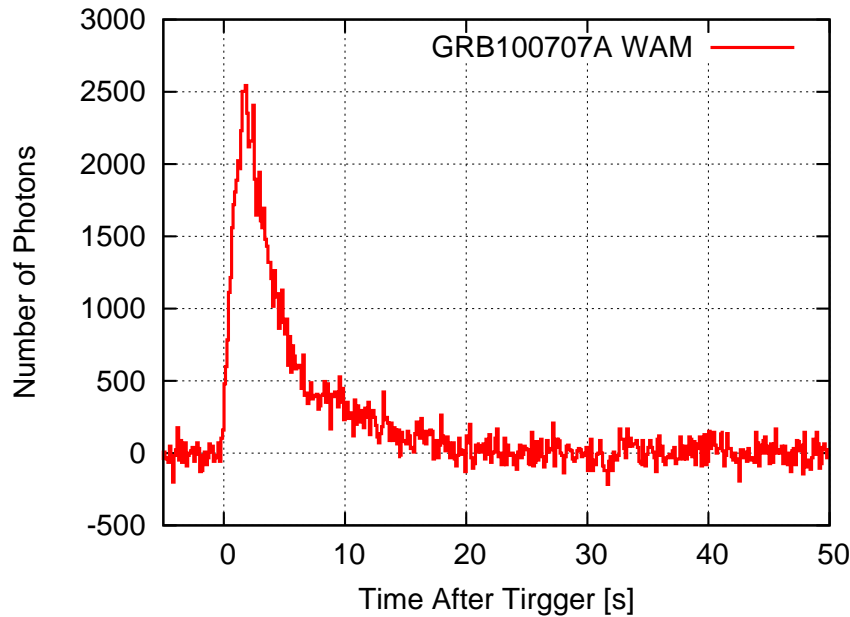


Figure 5.10: The light curve of prompt emission of GRB100707A detected by Suzaku WAM (WAM2, TH0: 50-110 keV). This figure shows the duration time of this burst is less than 30 s.

The two GRBs are GRB100510A detected by Fermi GBM and GRB100823A detected by Swift BAT and Fermi GBM. Timings of detection and locations of these events by MAXI GSC matches the those of other satellites. As for the afterglow candidate, GRB100707A was triggered by Fermi GBM, Konus-Wind, and Suzaku/WAM at July 7, 2010, 00:46:38 (UT). MAXI GSC scan the region near the position determined by Fermi GBM 303 s after GBM trigger (00:51:41 UT), and detected the X-ray emission at the position of (RA, Dec) = (357.8, -7.8). Figure 5.10 shows the prompt light curve of GRB100707A detected by Suzaku/WAM with energy range of 50-110 keV (TH0). The duration time of this GRBs are clearly less than 30 s. Thus, the X-ray counterpart detected by MAXI/GSC 300 s after the burst trigger is not the prompt burst, but should be considered as the X-ray afterglow of GRB100707A.

In addition to these three coincident events, five GRB candidates have been reported by MAXI GSC. These were identified as GRB on the basis of their positions and spectral hardness ratio.

Active Stars

Another class of X-ray transients distributed at high galactic latitude are stellar flare from active stars in the solar neighborhood. The positions of the MAXI transients are compared with active binary catalog[56]. This catalog lists 409 candidates of flare stars.

As a result, we identify three transients to active stars on the basis of positional match: a flare from HR1099 on January 23, 2010, a flare from II Peg on April 5, 2010, and a flare from TWA-7 on September 7, 2010. These transients have been already reported to the community with the alerts from the real time nova search system. We found no new X-ray flare from active stars in this search.

Active Galactic Nucleus

Another possibility for the short X-ray transient is a bright and short flare from active galactic nuclei, in particular BL Lac objects. We compared the transient list with VERONCAT, a database from the catalog of quasars and active galactic nuclei by Veron-Cetty and Veron[57]. VERONCAT catalog includes 1374 BL Lac objects. We found one of the MAXI transient that occurred on April 13, 2010 is positionally consistent with a BL Lac in VERONCAT. The field have been observed by ROSAT and XMM, and there is a known faint X-ray source at the position of BL Lac. If it is the transient, the X-ray flux is enhanced by a factor of $\times 10^4$ at the flare. This flare amplitude, as well as the short time scale of a few hours at maximum, are rather unusual even for a BL Lac. In addition, the error circle of the MAXI transient includes a large number of dim X-ray sources. There are 217 faint X-ray sources within 0.5° of the nominal We do not think there is strong reason to identify the source to the catalogued BL Lac.

Super Novae

Another intriguing possibility for short X-ray transients is supernova shock breakout, for which several UV observations and a X-ray observation have been reported. If a transient is a supernova shock breakout, we can expect the onset of an optical supernova to occur at the same position later.

We compared trigger time and position of all of our transients with the ASIAGOSN supernova catalog[58]. We found no supernova that matches with the time and position of our transients. Only one transient on October 29, 20009, occurred at the position consistent with a past supernova, SN 1991O with a nominal angular distance between them is 0.1° . Other than the positional coincidence, there is no evidence for connecting

these events. In addition, There are 10 ROSAT unidentified source within 0.5° of this transient. With all these, we cannot identify this source.

Cataclysmic Events in Nearby Galaxies

We additionally compared our transients with nearby optically bright galaxies in the Reference Catalogue of Bright Galaxies (RC3)[59]. RC3 catalog includes 23,022 galaxies with B-band magnitudes brighter than 15.5 or redshift not in excess of 15000 km s^{-1} ($z < 0.026$). One transient detected on December 11, 2010 occurred near a starburst galaxy. The distance between the transient and the galaxy was 0.3° . With this marginal positional coincidence, this transient can be a candidate of a supernova shock breakout or a tidal disruption event in this galaxy. However, no optical transients including supernova have been reported from this position, and the association of the transient with the galaxy is not convincing. In order to investigate the evidence of supernova shock breakout, the early detection report of a MAXI transient and rapid follow-up observations is absolutely needed.

Summary

We summarize identification for our 29 transients. There are 8 prompt GRBs, 1 GRB afterglow, 3 flare stars, 2 X-ray sources, and 15 unidentified transients.

Half of our transients are identified but others are not. The origin of these unidentified transients is probably GRBs, XRFs, or other extragalactic cataclysmic events. We statistically investigated the origin of these events in the next chapter.

Chapter 6

Discussion

In this chapter, we discuss our results of the transient search. At first, we calculated the dipole moment $\langle \cos\theta \rangle$ to test the anisotropy of the transients. We also calculated the value of $\langle V/V_{max} \rangle$ to test the spatial homogeneity and finally we plotted the LogN-LogS distribution and estimated the origin of these transients.

6.1 Statistic Estimation for Transients

6.1.1 Dipole Moment

Large angular scale anisotropies are searched for with dipole and quadruple statistics. Various dipole and quadruple statistics have been introduced to the field of GRB studies by Harmann et al. 1989[60], Paczynski et al. 1990[61], and Briggs et al. 1993[12]. Dipole statistics are sensitive to a concentration of GRBs toward one direction on the sky, while quadruple statistics are sensitive to concentrations in a galactic plane or toward the opposite poles. In our case, since the galactic plane is excluded from the sample, it is difficult to estimate the value of quadruple moment. Thus, we did not test the quadruple moment using our samples. The value of dipole moment are defined as the $\langle \cos\theta \rangle$, where θ is the average angular distance from the Galactic Center (l, b = 0, 0). the maximum value of θ is 180 degree at the anti-Galactic Center (l, b = 180, 0).

We calculated the dipole moment for detected transients using the angular distance from the Galactic Center. In order to exclude the effect of galactic halo, we excluded the region within 20° from the Galactic Center. We also excluded the opposite direction ($\theta > 160^\circ$) of the Galactic Center to compensate the bias of the selected data. In order to correct the exposure bias of angular distribution, we made the angular distribution by exposure map, and the distribution of the dipole moment $\langle \cos\theta \rangle$ was calculated with

the weight proportional to exposure.

We obtained the dipole moment of 0.02 ± 0.17 for the 27 sources with statistical probability of 10^{-8} . With this result, we find that these transients are distributed isotropically. Thus the most of candidates of detected transients are GRBs, GRB afterglows, AGNs, or flare stars. We will investigate the source origin based on the value $\langle V/V_{max} \rangle$ and the $\text{Log}N\text{-Log}S$ distribution in following sections.

6.1.2 V/V_{max} Test

V/V_{max} test is proposed by Schmidt et al. 1988[24]. This method provides a quantitative evaluation for the uniformity of the radial distribution of objects in a well-defined sample. Detection schemes of V/V_{max} method are based on counts rather than peak energy flux or time integrated energy flux.

Here, we used the selected data with probability of 10^{-8} corresponding to 9σ significance. We set the threshold for $\langle V/V_{max} \rangle$ test with minimum value of C_{lim} in our 29 samples. Then we obtained $\langle V/V_{max} \rangle = 0.517 \pm 0.054$ for the 29 sources. This value is consistent with uniformly spatial distribution in Euclidean space. Thus, the result of estimation of $\langle V/V_{max} \rangle$ indicates that most of candidate for detected transients are the samples with small or no effect of redshift. This value of $\langle V/V_{max} \rangle$ suggest two possibilities. 1. The number of GRBs in our samples are small, or 2. almost of detected GRBs are bright source only. In order to test these possibilities, we study the $\text{log}N\text{-Log}S$ distribution in the following subsection.

6.1.3 $\text{Log}N\text{-Log}S$ distribution

The detail explanation of $\text{Log}N\text{-Log}S$ distribution is described in section 3.1.2. For this estimation, we excluded the events on the galactic plane and the region within 20 degrees from the Galactic Center. so we do not consider the X-ray transient from these areas.

Then we compare the frequency of GRBs obtained by the Swift results (Sakamoto et al. 2011[62]). Figure 6.1 shows the $\text{Log}N\text{-Log}S$ plot with the probability threshold of 10^{-8} which is corresponding to $\sim 9.0\sigma$ significance.

In the Swift BAT GRB catalog[62], the spectral index α and 15–25 keV photon flux are obtained by the fitting with cutoff power-law or simple power-law function. we converted Swift BAT hard X-ray flux (15–25 keV) to our soft X-ray flux (4.0–10.0 keV) by extrapolating the power-law function with these spectral parameters.

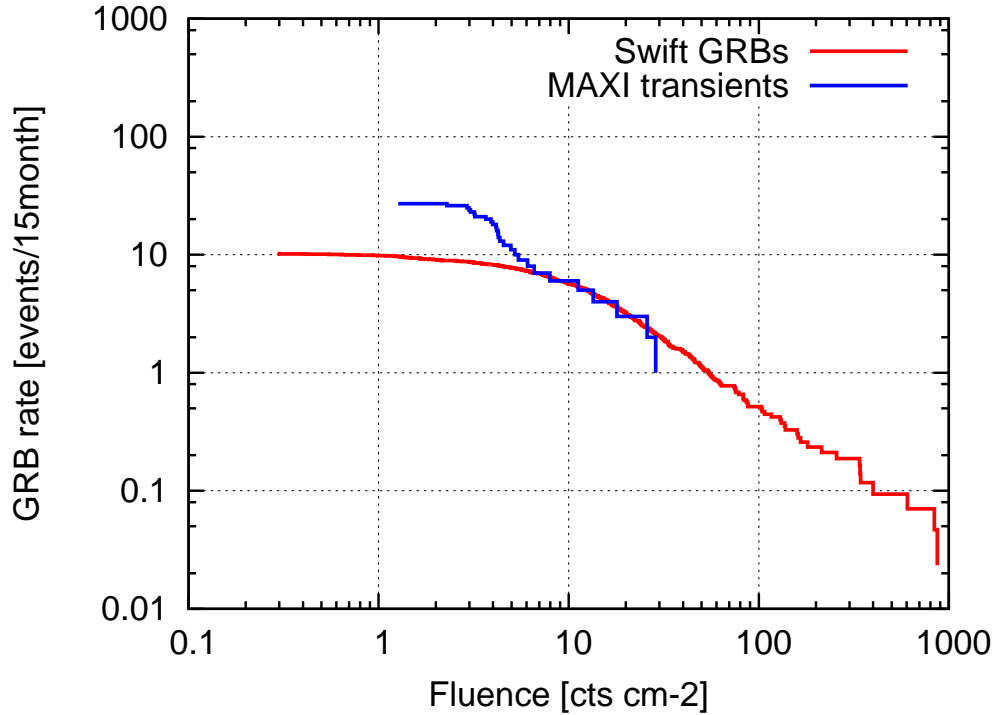


Figure 6.1: LogN-LogS distribution of 29 X-ray transients with the probability threshold of 10^{-8} . Red line shows the by Swift BAT result(15–25 keV) using the flux converted to the GSC energy range and normalized with the observing conditions (see text for details).

Conversion of Swift into MAXI rate

Next, we describe the conversion of the GRB rate of the Swift BAT to the MAXI range in the LogN-LogS plot. We obtained the rate conversion factor R for Swift to MAXI as equation 6.1

$$R = \left(\frac{T_{\text{maxi}}}{T_{\text{swift}}} \right) \left(\frac{\epsilon_{\text{maxi}}}{\epsilon_{\text{swift}}} \right) \left(\frac{F_{\text{maxi}}}{F_{\text{swift}}} \right) = 0.026 \quad (6.1)$$

where T is the mission life time after launch, ϵ is the operation efficiency which is a duty cycle for instruments, and F is the field of view. Table 6.1 shows the value for calculation of conversion factor for Swift BAT to MAXI GSC. The obtained value of rate conversion factor is $R = 2.6 \times 10^{-2}$.

Conversion of Flux into Fluence

The flux measured by Swift BAT must be converted the X-ray fluence that would have been measured by MAXI GSC.

The shape of GRB light curves were approximated by the simple multi triangle. We used the typical duration time of GRB ($T_{90} = 40$ s; this is the average value of T_{90} for long GRBs) for this conversion. The transient flux detected by GSC also needed to be converted the flux to the fluence. In the case of GSC, the flux obtained by the GSC is the averaged flux. Thus, we assumed the shape of GRB was box shape and duration of GRB was 40 s which was corresponding to the source visible time for GSC.

Two Components in Log N -Log S plot

The result of Log N -Log S distribution with probability threshold of 10^{-8} suggests there are two different distribution.

One is the high fluence component, this component is well fitted by GRB distribution observed by Swift. Most of MAXI GRBs are included in this component. As described in the section 3.1.3, the properties of XRFs are similar to those GRBs, and the luminosity of XRFs is distributed with GRBs continuously. Thus, XRFs might be also included in this region.

The other component is distributed the in low fluence region. This component follows a power-law distribution with index of $-3/2$. The identified GRB afterglow, flare stars, X-ray sources, and AGNs belong to this component. Most of unidentified transients are also belong to this components. A few transients are detected at the positions of flare stars (3 transients) and a BL Lac (1 transient) in our transient search. Some of the transients in our sample may be indeed the flares of active stars and AGNs. Since repeated detections of transients from these positions are expected for these objects, future MAXI observations are useful for identifying them.

Other likely possible candidate for the faint transients detected in the distribution with index $-3/2$ might be X-ray afterglow of GRBs. The large number of GRBs should be not detected and reported by Swift or other satellite because of the outside of field of view, lower flux than threshold, detectable only X-ray band (XRFs), or no prompt emission (orphan afterglows). In addition, The candidates for index $-3/2$ also likely include the tidal disruption, or super nova shock breakout.

Table 6.1: Conversion values of Swift BAT and MAXI GSC

Detector	Term [month]	Operation efficiency	Field of view [str]
Swift BAT	60	0.8	1.4
MAXI GSC	15	0.4	0.29

6.1.4 Comparison of the Rate of XRF with GRB

Although the number of detection is few events, the rate of GRBs obtained by MAXI GSC is corresponding to that of Swift GRBs in obtained Log N -Log S distribution.

The Log N -Log S distributions for HETE GRBs and XRFs are shown in Sakamoto 2004[63]. The significant difference (factor ~ 2) is shown between the flux distributions of GRBs and XRFs. The average flux of XRFs is dimmer than GRBs. In addition, distribution of flux of XRFs and GRBs are continuously connected with each other. Thus, the merged data of XRFs and GRBs might distribute as the GRB distribution, and shift to number of increasing on the Log N -Log S plot. However, for the MAXI data, we obtained GRB distribution which corresponds to the Swift GRBs. The reason of this results are considered as following. (1) Statistic amount is small. (2) Swift can detect XRFs with low E_{peak} (< 15 keV) events. These results will be confirmed by future observation and detection of transients.

6.1.5 Transients in the Index $-3/2$ Region

We discuss the origin of the $-3/2$ region. If the origin of the transients in the index $-3/2$ region is the afterglow of GRBs or XRFs, prompt emission of these GRBs might be detected by other satellites. However, as the result of comparison with the timing of transient detected by other GRB monitors, coincident event has been detected only one event. It suggests that afterglow event is not dominant in the $-3/2$ region, though we estimate the number of GRBs that are not detectable by other satellites due to its field of view or operation efficiency.

The reasons for these non-detection of afterglows are considered as following. (1) These events are invisible in the hard X-ray band and most of these prompt events are XRFs. (2) These transients are the candidates of orphan afterglow. (3) The main part of origin of these events are not GRBs. The cause (1) is inconsistent with the previous comparison with Swift GRBs. The causes (2) and (3) indicates the detection of tidal disruptions or super nova shock brakeouts.

Since the most of our transients did not have the follow up observation, identification of these transients are difficult. The preparation of the follow up observation for an transient which will be found by future monitoring are essential for identification. If we continue the monitoring and additional observation, a few identified new type of transient will certainly be found.

6.2 Future Work

Finally, we will describe the future works of short X-ray transient search with MAXI GSC data. The most of unidentified transients are distributed in the region with index of $-3/2$. This result suggests that candidates of these events are not prompt GRBs and XRFs but afterglows or new transients.

In order to discuss further possibility, following transient search is needed.

1. Transient search in the additional term,
2. Transient search with other energy range after the calibration,
3. Transient search for the galactic plane,
4. Systematic search on the lower flux than this work,
5. Follow up observation just after the transient detection.

In particular, since follow up observation has the possibility of detection for new type of transients, it is necessary to develop the system which can give the alert of transient detection for follow up observation.

Chapter 7

Conclusion

Transient Search

We newly developed transient search programs and searched for fast X-ray transients from the single scan data of MAXI GSC. The transient events are extracted in the data between October 1, 2009 and December 31, 2011. We carried out the two step of extraction. At first we roughly extracted the transient events from all-sky data. Next, we extracted the transient events in detail by the fitting with PSF function, and calculated the flux and the fluctuated probability. Finally we found the 29 transients with the probability of 10^{-8} which is corresponding to 9σ significance.

Statistical Property of Transients

We investigated the origin of the transients by angular distribution, V/V_{max} test, and the $\text{Log}N\text{-Log}S$ distribution. We got the value of these parameters as $\langle \cos\theta \rangle = 0.02 \pm 0.17$ and $\langle V/V_{max} \rangle = 0.517 \pm 0.054$. The value of angular distribution indicates the these transients are isotropic in the sky. Thus, candidates for these transients are GRBs, XRFs, AGNs, flare stars, or other X-ray transients. These results were similar to past researches [11, 7, 6, 1, 3]. The value of $\langle V/V_{max} \rangle$ indicates that the distribution of the transients are isotropic and uniformly in the Euclidean space.

Comparison with Swift GRBs

The $\text{Log}N\text{-Log}S$ distribution obtained by MAXI GSC transients indicated two components which are GRBs and other transients. The GRB components are well fitted by the Swift GRB curve, and other component are distributed parallel with index of $-3/2$. The most of unidentified transients are included in this region. The origin of these transients are afterglows or other origin. Therefore, the follow up observation for these X-ray

transients has the potential of detection for rare events such as tidal disruption or super nova shock breakouts. The additional data for transient search and follow up observations should be expected for identification of the origin of these X-ray transients.

Appendix A

Comparision with past MAXI data

A.1 Comparision with MAXI GRB

In order to check the availability of our transient search, We compared the transient search with the past detected GRB data. Table A.1 shows the past detected GRB by GSC, and we can see that the most of GRBs are detected by our transient search. GRB091230 and no identified source 101030 are not detected by our transient search, because these transients are placed at the galactic plane of $|b| < 10$ degree. GRB091120 and 091201 are not also detected. A reason of none detection of these transients are possibly exclusion for solar events or other sources. We must be investigate these events in detai on future work.

A.2 Comparision with MAXI Flare Star

We searched for flare stars detected by past GSC operation as the previous section. We detected two stars by transient search of this thesis. Obtained flux of these stars by the transient search is 0.109 ± 0.011 cnt cm⁻² s⁻¹, and 0.092 ± 0.002 cnt cm⁻² s⁻¹ respectively. Thus, these stars does not contributed to the part of bright sources in our result of LogN-LogS plot. The detection limit of our transient search using only 1 orbit is about 50 mCrab. Since most of flare stars are detected by integrating mult-orbit data, the plobability of detection for flare stars in 1 orbit is relatively low. In addision, since the spectra of flare stars are relatively softer than that of GRBs, it is not possively detected in the 4.0–10.0 energy band. Therefore, we concluded that the most of transients detected in 1 orbit are GRB by comparision of transient search with the past operation data. The ratio of the detection efficiency between GRB and flare star is about 9:2 by this estimation.

Table A.1: Comparison for this work with past detected GRB by MAXI. Galactic plane is defined by $|b| < 10$ degree. The triangle in detection column means the detection in a low significance ($> 1.0 \times 10^{-6}$) data obtained by transient search. The circle means the detection with high significance ($< 1.0 \times 10^{-8}$)

GRB name	Detection Time(UT)	RA(J2000)	Dec(J2000)	l	b	GCN	TS detction
GRB091012	2009-10-12 10:23:12	182.82	+63.37	130.42	53.17	none	○
GRB091120	2009-11-20 04:34:40	226.81	-21.79	340.20	31.08	GCN10188	Sun angle 8.47°
091201	2009-12-01 21:48:36	118.60	+16.60	204.56	21.20	GCN10229	–
GRB091230	2009-12-30 06:27:30	132.91	-53.88	272.06	-6.06	none	galactic plane
XRF100315A	2010-03-15 17:13:40	74.95	-6.63	205.84	-27.80	GCN10492	△
100327	2010-03-27 17:08:15	346.03	+42.90	102.84	-15.75	GCN10552	○
GRB100415A	2010-04-15 03:44:57	7.48	-15.57	98.46	-77.41	GCN10596	○
GRB100510A	2010-05-10 19:27:09	355.80	-35.60	358.48	-73.10	GCN10739	○
XRF100616A	2010-06-16 01:42:13	50.95	-40.62	246.18	-55.95	GCN10860	○
XRF100701A	2010-07-01 06:54:28	188.86	-34.26	299.17	28.49	GCN10914	○
GRB100823A	2010-08-23 17:25:35	20.70	+5.84	137.04	-56.18	GCN11151	○
100911	2010-09-11 14:58:20	103.41	-70.43	281.19	-25.26	ATEL2842	○
101030	2010-10-30 10:09:07	279.98	+1.85	33.27	3.41	ATEL2990	galactic plane

Table A.2: Comparison for this work with past detected flare from active star by MAXI sorted by date. Galactic plane is defined by $|b| < 10$ degree. The triangle in detection column means the detection in a low significance ($> 1.0 \times 10^{-6}$) data obtained by transient search. The circle means the detection with high significance ($< 1.0 \times 10^{-8}$)

Source name	Detection Date(UT)	RA(J2000)	Dec(J2000)	l	b	TS detection
VY Ari	2009-11-09	42.0	+31.1	150.6	-25.4	—
HR1099	2010-01-23	54.2	+0.6	184.9	-41.6	○
AR Lac	2010-01-23	332.2	+45.7	95.6	-8.3	galactic plane
HR1099	2010-02-17	54.2	+0.6	184.9	-41.6	—
II Peg	2010-04-05	358.8	+28.6	108.2	-32.6	○
AR Lac	2010-06-29	332.2	+45.7	95.6	-8.3	galactic plane
II Peg	2010-08-25	358.8	+28.6	108.2	-32.6	△
II Peg	2010-08-26	358.8	+28.6	108.2	-32.6	△
TWA 7	2010-09-07	160.0	-33.7	274.3	+21.9	○
HR1099	2010-11-03	54.2	+0.6	184.9	-41.6	—
Algol	2010-12-31	47.0	+41.0	149.0	-14.9	—

Appendix B

Figures

We show the light curve of detected transients in here. Following figures plotted with The horizontal axis are normarized by the transient detection time. The flux is calculared by PSF fitting for MAXI GSC. The value of flux is the merged value for multi cameras.

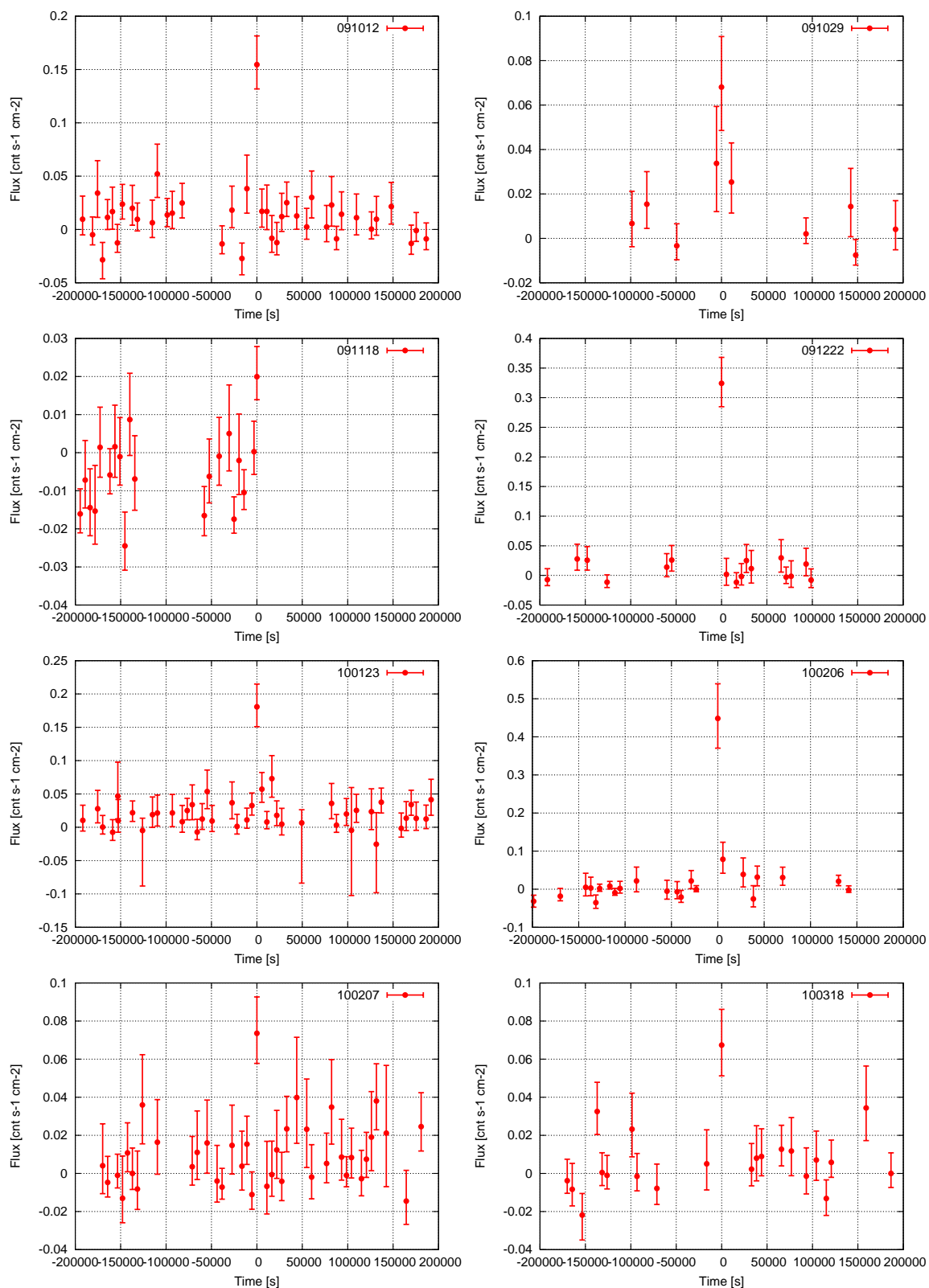


Figure B.1: Light curves of transients

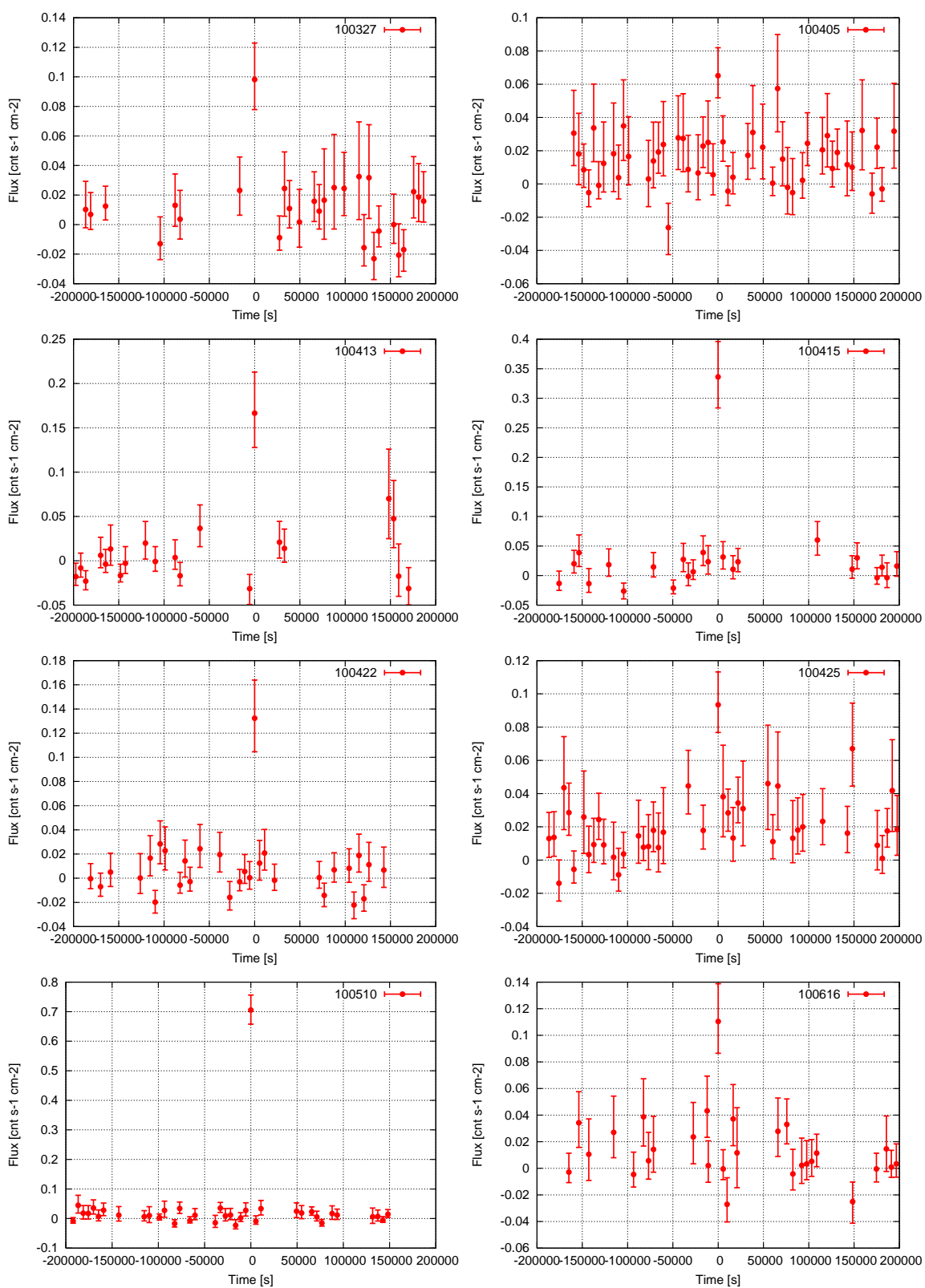


Figure B.2: Light curves of transients

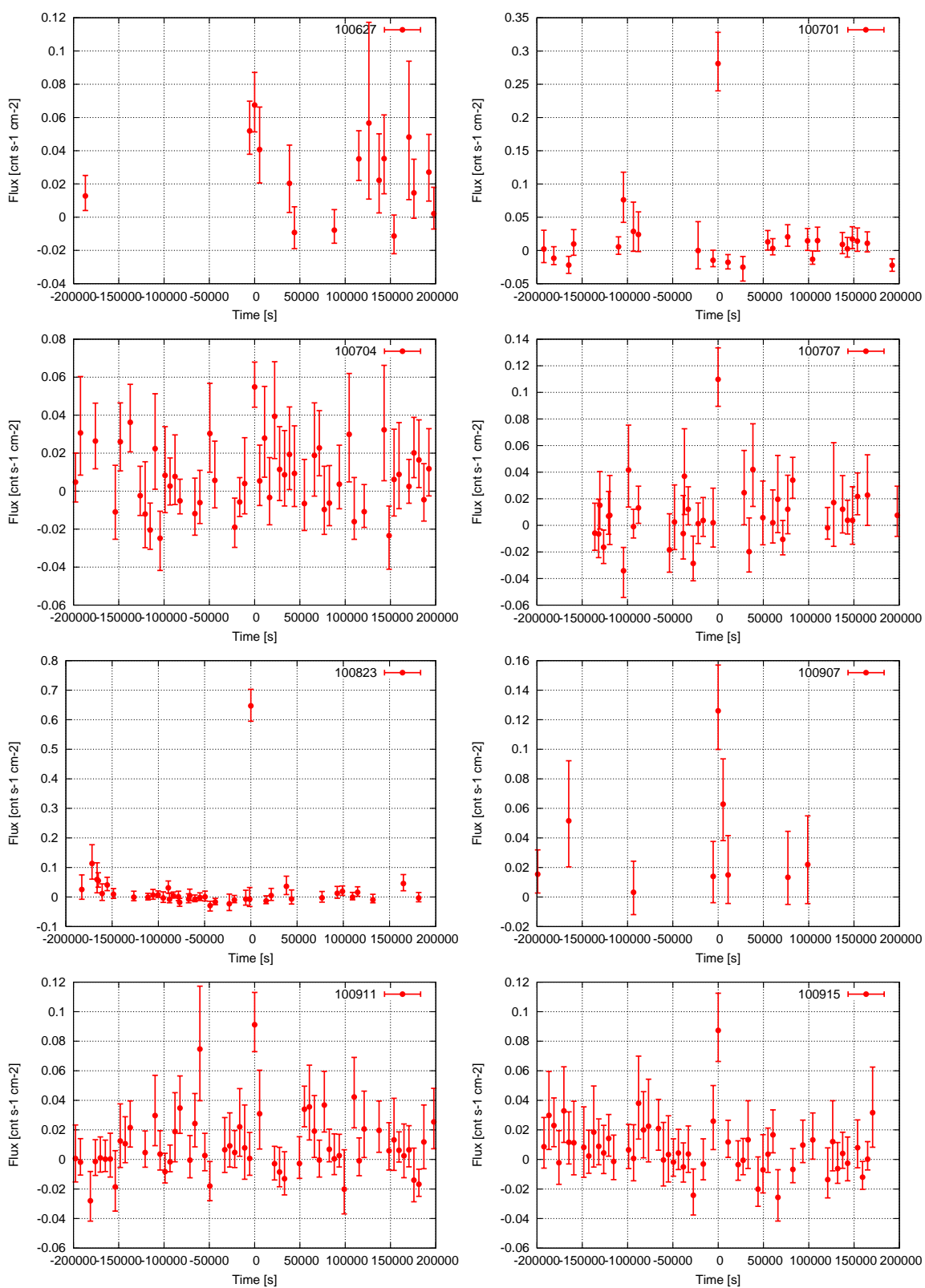


Figure B.3: Light curves of transients

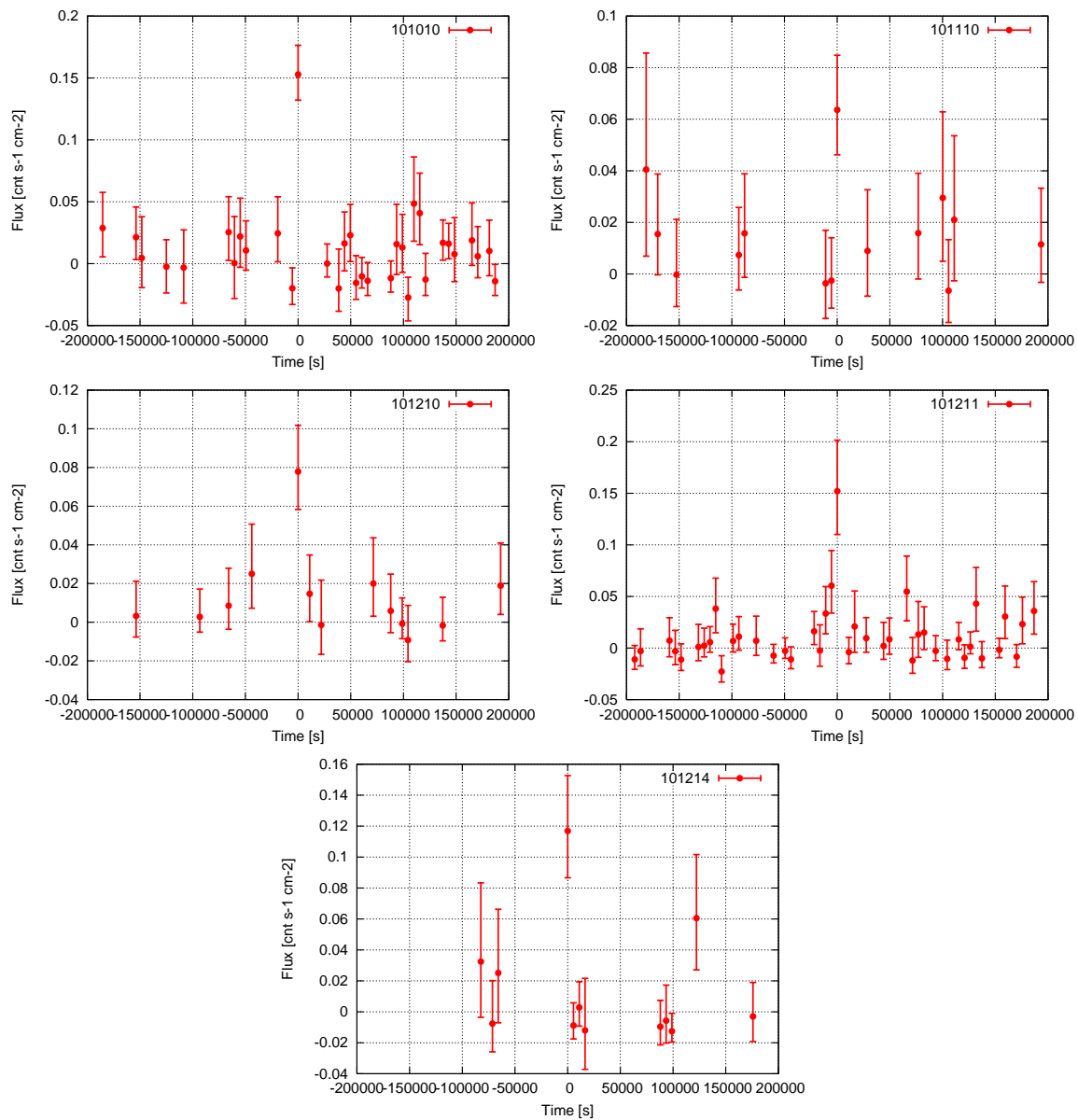


Figure B.4: Light curves of transients

Bibliography

- [1] C. W. Ambruster, K. S. Wood. The HEAO A-1 all-sky survey of fast X-ray transients. *ApJ*, 311, 258–274, December 1986.
- [2] A. Connors, P. J. Serlemitsos, J. H. Swank. Fast transients - A search in X-rays for short flares, bursts, and related phenomena. *ApJ*, 303, 769–779, April 1986.
- [3] J. E. Grindlay. Fast X-Ray Transients and Gamma-Ray Bursts: Constraints on Beaming. *ApJ*, 510, 710–714, January 1999.
- [4] E. V. Gotthelf, T. T. Hamilton, D. J. Helfand. The Einstein Observatory Detection of Faint X-Ray Flashes. *ApJ*, 466, 779, August 1996.
- [5] A. J. Castro-Tirado *et al.* Observations of short-duration X-ray transients by WATCH on GRANAT. *AAP*, 347, 927–931, July 1999.
- [6] J. Greiner *et al.* Search for GRB X-ray afterglows in the ROSAT all-sky survey. *AAP*, 353, 998–1008, January 2000.
- [7] J. Heise *et al.* X-Ray Flashes and X-Ray Rich Gamma Ray Bursts. In E. Costa, F. Frontera, & J. Hjorth, editor, *Gamma-ray Bursts in the Afterglow Era*, page 16, 2001.
- [8] T. Sakamoto *et al.* Global Characteristics of X-Ray Flashes and X-Ray-Rich Gamma-Ray Bursts Observed by HETE-2. *ApJ*, 629, 311–327, August 2005.
- [9] D. N. Burrows *et al.* Relativistic jet activity from the tidal disruption of a star by a massive black hole. *Nature*, 476, 421–424, August 2011.
- [10] A. M. Soderberg *et al.* An extremely luminous X-ray outburst at the birth of a supernova. *Nature*, 453, 469–474, May 2008.
- [11] V. A. Arefiev, W. C. Priedhorsky, K. N. Borozdin. Fast X-Ray Transients and Their Connection to Gamma-Ray Bursts. *ApJ*, 586, 1238–1249, April 2003.

- [12] M. S. Briggs. Dipole and quadrupole tests of the isotropy of gamma-ray burst locations. *ApJ*, 407, 126–134, April 1993.
- [13] J. P. Pye, I. M. McHardy. The Ariel V sky survey of fast-transient X-ray sources. *MNRAS*, 205, 875–888, November 1983.
- [14] H. h. p. . Heasac home page granat.
URL: http://heasarc.gsfc.nasa.gov/docs/granat/granat_about.html.
- [15] R. M. Kippen *et al.* BATSE Observations of Fast X-Ray Transients Detected by BeppoSAX-WFC. In E. Costa, F. Frontera, & J. Hjorth, editor, *Gamma-ray Bursts in the Afterglow Era*, page 22, 2001.
- [16] G. N. Pendleton *et al.* The Intensity Distribution for Gamma-Ray Bursts Observed with BATSE. *ApJ*, 464, 606, June 1996.
- [17] R. W. Klebesadel, I. B. Strong, R. A. Olson. Observations of Gamma-Ray Bursts of Cosmic Origin. *ApJL*, 182, L85, June 1973.
- [18] D. Band *et al.* BATSE observations of gamma-ray burst spectra. I - Spectral diversity. *ApJ*, 413, 281–292, August 1993.
- [19] R. Salvaterra *et al.* GRB090423 at a redshift of $z = 8.1$. *nat*, 461, 1258–1260, October 2009.
- [20] A. Cucchiara *et al.* A Photometric Redshift of $z = 9.4$ for GRB 090429B. *apj*, 736, 7, July 2011.
- [21] R. S. Mallozzi, B. team. Batse gamma-ray burst durations.
URL: <http://gammaray.msfc.nasa.gov/batse/grb/duration/>.
- [22] M. S. Briggs *et al.* BATSE Observations of the Large-Scale Isotropy of Gamma-Ray Bursts. *ApJ*, 459, 40, March 1996.
- [23] J.-L. Atteia *et al.* A second catalog of gamma-ray bursts - 1978-1980 localizations from the interplanetary network. *ApJS*, 64, 305–317, May 1987.
- [24] M. Schmidt, J. C. Higdon, G. Hueter. Application of the V/V(max) test to gamma-ray bursts. *ApJL*, 329, L85–L87, June 1988.
- [25] C. Kouveliotou *et al.* Identification of two classes of gamma-ray bursts. *ApJL*, 413, L101–L104, August 1993.

- [26] E. Costa *et al.* Discovery of an X-ray afterglow associated with the γ -ray burst of 28 February 1997. *Nature*, 387, 783–785, June 1997.
- [27] J. van Paradijs *et al.* Transient optical emission from the error box of the γ -ray burst of 28 February 1997. *Nature*, 386, 686–689, April 1997.
- [28] R. Yamazaki, K. Ioka, T. Nakamura. X-Ray Flashes from Off-Axis Gamma-Ray Bursts. *ApJL*, 571, L31–L35, May 2002.
- [29] J. Heise, J. in't Zand. Galactic and extragalactic Fast X-ray Transient sources. *Nuclear Physics B Proceedings Supplements*, 132, 263–270, June 2004.
- [30] R. Yamazaki, K. Ioka, T. Nakamura. Peak Energy-Isotropic Energy Relation in the Off-Axis Gamma-Ray Burst Model. *ApJL*, 606, L33–L36, May 2004.
- [31] T. Takahashi *et al.* ASCA Observation of an X-Ray/TeV Flare from the BL Lacertae Object Markarian 421. *ApJL*, 470, L89, October 1996.
- [32] T. Takahashi *et al.* Complex Spectral Variability from Intensive Multiwavelength Monitoring of Markarian 421 in 1998. *ApJL*, 542, L105–L109, October 2000.
- [33] J. Kataoka *et al.* Characteristic X-Ray Variability of TeV Blazars: Probing the Link between the Jet and the Central Engine. *ApJ*, 560, 659–674, October 2001.
- [34] C. Tanihata *et al.* Variability Timescales of TeV Blazars Observed in the ASCA Continuous Long-Look X-Ray Monitoring. *ApJ*, 563, 569–581, December 2001.
- [35] N. Isobe *et al.* Bright X-Ray Flares from the BL Lac Object Markarian 421, Detected with MAXI in 2010 January and February. *PASJ*, 62, L55, December 2010.
- [36] K. Hiroi *et al.* The First MAXI/GSC Catalog in the High Galactic-Latitude Sky. *PASJ*, 63, 677, November 2011.
- [37] A. Uzawa *et al.* A large X-ray flare from a single weak-lined T Tauri star TWA-7 detected with MAXI GSC. *PASJ*, 63, 713–716, 2011.
- [38] K. Yamazaki *et al.* Giant X-ray flares on RS-CVn stars detected with MAXI/GSC. *in prep.*
- [39] S. Campana *et al.* The unusual gamma-ray burst GRB 101225A explained as a minor body falling onto a neutron star. *Nature*, 480, 69–71, December 2011.

- [40] J. S. Bloom *et al.* A Possible Relativistic Jetted Outburst from a Massive Black Hole Fed by a Tidally Disrupted Star. *Science*, 333, 203, July 2011.
- [41] C. C. Thöne *et al.* The unusual γ -ray burst GRB 101225A from a helium star/neutron star merger at redshift 0.33. *Nature*, 480, 72–74, December 2011.
- [42] S. A. Colgate. Early Gamma Rays from Supernovae. *ApJ*, 187, 333–336, January 1974.
- [43] R. I. Klein, R. A. Chevalier. X-ray bursts from Type II supernovae. *ApJL*, 223, L109–L112, August 1978.
- [44] D. N. Burrows *et al.* Swift X-Ray Telescope. In K. A. Flanagan & O. H. Siegmund, editor, *Society of Photo-Optical Instrumentation Engineers (SPIE) Conference Series*, volume 4140 of *Society of Photo-Optical Instrumentation Engineers (SPIE) Conference Series*, pages 64–75, December 2000.
- [45] T. Mihara *et al.* Gas Slit Camera (GSC) onboard MAXI on ISS. *ArXiv e-prints*, March 2011.
- [46] M. Sugizaki *et al.* In-Orbit Performance of MAXI Gas Slit Camera (GSC) on ISS. *ArXiv e-prints*, February 2011.
- [47] H. Tomida *et al.* Solid-State Slit Camera (SSC) Aboard MAXI. *PASJ*, 63, 397–405, April 2011.
- [48] H. Tsunemi *et al.* In Orbit Performance of the MAXI/SSC onboard the ISS. *ArXiv e-prints*, January 2011.
- [49] Y. Shirasaki *et al.* Design and Performance of the Wide-Field X-Ray Monitor on Board the High-Energy Transient Explorer 2. *PASJ*, 55, 1033–1049, October 2003.
- [50] H. Negoro *et al.* GRB 110213B: MAXI/GSC detection of a probable GRB. *GRB Coordinates Network*, 11716, 1, 2011.
- [51] M. Morii *et al.* GRB 110213B: MAXI/GSC refined analysis. *GRB Coordinates Network*, 11720, 1, 2011.
- [52] M. Kimura *et al.* XRF 111111A/MAXI J0158-744: MAXI GSC and SSC detection of a soft X-ray transient near SMC. *GRB Coordinates Network*, 12554, 1, 2011.
- [53] M. Morii *et al.* XRF 111111A/MAXI J0158-744: MAXI GSC refined analysis. *GRB Coordinates Network*, 12555, 1, 2011.

- [54] M. Morii *et al.* Alignment calibration of MAXI/GSC. *Physica E Low-Dimensional Systems and Nanostructures*, 43, 692–696, January 2011.
- [55] H. home page. Healpix. URL: <http://healpix.jpl.nasa.gov>.
- [56] Z. Eker *et al.* Chromospherically Active Binaries. Third version (Eker+, 2008). *VizieR Online Data Catalog*, 5128, 0, June 2008.
- [57] M. P. Veron-Cetty, P. Veron. Quasars and Active Galactic Nuclei (13th Ed.) (Veron+ 2010). *VizieR Online Data Catalog*, 7258, 0, 2010.
- [58] R. Barbon *et al.* The Asiago Supernova Catalogue - 10 years after. *AAPS*, 139, 531–536, November 1999.
- [59] H. G. Corwin, Jr., R. J. Buta, G. de Vaucouleurs. Corrections and additions to the third reference catalogue of bright galaxies. *AJ*, 108, 2128–2144, December 1994.
- [60] D. Hartmann, R. I. Epstein. The angular distribution of gamma-ray bursts. *ApJ*, 346, 960–966, November 1989.
- [61] B. Paczynski. A test of the galactic origin of gamma-ray bursts. *ApJ*, 348, 485–494, January 1990.
- [62] T. Sakamoto *et al.* The Second Swift Burst Alert Telescope Gamma-Ray Burst Catalog. *ApJS*, 195, 2, July 2011.
- [63] T. Sakamoto. PHD thesis; Spectral Characteristics of X-ray Flashes and X-ray Rich Gamma-ray Bursts Observed by HETE-2. April 2004.

Acknowledge

I would like to special thank to Professor Nobuyuki Kawai who gave me great opportunities for study and wonderful science theme. Especially after my doctoral course, he gave me a lot of chance and experience for presentaion in international conference, these are very educational for me. In addition, thanks to his earnestly leading for final half year, I managed to finish writting this thesis. I am also grateful to Prof. Jun Kataoka for his earnesly instrunction for experimetns, writting thesis, and presentaion in my master course.

I wish to thank all members of Kawai labolatory. Dr. Yatsu, Dr. Morii, Dr. Saito and Mr. Usui was always helped me for experiments, data analyasis, statistics, discussions, and ordinaly life in our labolatory. Throughout my labolatory life, Mr. Tsubuku, Dr. Arimoto, Dr. Nakamori, Dr. Kanai, and Mr. Koizumi helped me for experiments and ordinaly life. In addition, all of younger members in labolatory are very kind and fun for me. I would like to thank you very much for my pleasant life in labolatory.

I also apreciate MAXI term members for many help for my thesis. Prof. Negro, Dr. Serino, Mr. Hiroi, and Ms. Shidatsu gave me the useful information and data for analysis for my transient search.

Finally, I am greateful my family member, especially, my parents for giving me the oppatunity and time to study science. If they do not said me ‘Never give up.’, I may not be able to finish writing my thesis. Thank you very much.